The origin of magma encountered during drilling of geothermal well KJ-39, Krafla, Iceland and the relationship with the nearby IDDP-1 magma.

A thesis submitted in partial fulfilment of the requirements for the degree

Master of Science in Geology

at

the University of Canterbury

Georgina Rule

2020

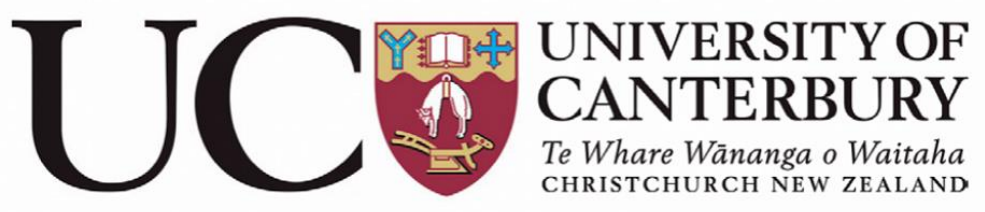

Acknowledgements

First and foremost, I would like to thank my primary supervisor Alex Nichols for providing endless support, answering all of my stupid questions and assuring me that mistakes are just part of the research process. Thanks also to my other supervisor Ben Kennedy for giving me the chance to take this project and for always thinking outside the box, and to Ian Schipper for the crash course using the microprobe and answering my last minute questions.

Huge thanks to the technicians at UC, especially Rob Spiers, for letting me invade your lab for four months and for keeping me company in the prep room.

I would like to thank the Mason Trust for providing the funds to go to Wellington and giving me the opportunity to present my research at the GSNZ conference in Hamilton. It truly was a fantastic opportunity. I must also thank Sarah and Ben Holland for letting me stay multiple times while I was in Wellington to use the microprobe.

Finally, I need to thank my family, boyfriend and particularly my dad for moral and financial support throughout this project.

Abstract

In July 2008, well KJ-39 encountered magma at 2571 metres below the surface while drilling into the geothermal system within the Krafla central volcano, north-eastern Iceland. The magma was returned to the surface as quenched glass along with a resorbed mineral assemblage consisting of bytownite with some anorthite and augite with minor pigeonite and orthopyroxene lamellae. In June 2009, the better-known IDDP-1 well, located 2.5 km north of KJ-39, also intercepted rhyolitic melt and partially molten felsite rich in quartz, plagioclase and alkali feldspar. Because of the proximity of the two drill holes, I investigate whether the magma encountered in KJ-39 is from the same source as IDDP-1. This will have important implications for the dimensions of the magma chamber and thus future geothermal drilling operations. Major elements, S, Cl and F have been measured in KJ-39 glass chips using electron probe micro-analysis (EPMA) and H_2O and CO_2 have been measured using Fourier-transform infrared spectroscopy (FTIR). The KJ-39 chips have a striking range in composition, from andesitic to rhyolitic (SiO_2 58-75 wt%), the H_2O content ranges from 0.64-3.02 wt% with some samples showing evidence of partial or total hydration and CO_2 measurements range from 5-40 ppm, although most measurements were masked by atmospheric CO_2. S contents range from below detection to 1373 ppm and show a strong negative correlation with SiO_2, as does F, while Cl shows a positive correlation with SiO_2. Based on the chemistry and petrology of the KJ-39 samples, there is evidence for formation of a high-SiO_2 rhyolite by partial melting of hydrated basalt, while the andesitic and dacitic glass compositions presented here suggest partial melting of a more mafic source, an andesite, likely melted by the same heat source. When this mechanism for formation is compared with that for IDDP-1 both are to some degree formed by the partial melting of hydrated basalt. The wide range of glass compositions in the KJ-39 sample compared to IDDP-1 suggests that the two melts are not derived from the same source; however, the proximity of the two wells indicates that melting could have been driven from the same heat source. The evidence provided by this study for partial melting processes producing high-SiO_2 rhyolites in basaltic environments, such as Krafla, shows that this process could be more common than previously considered. The wider Krafla region could, therefore, have more of these felsic melt pockets, the peripheries of which would be ideal targets for geothermal exploration and exploitation.

Table of Contents

List of Figures

Chapter 1: Introduction

Chapter 2: Krafla Geothermal Field and Previous Drilling

Chapter 3: Impact of Magmatic Processes and Volatiles on Melt

Chapter 4: Analytical Methods

Chapter 5: Petrographic and Geochemical Results of KJ-39 Cuttings

Chapter 6: Origin of the KJ-39 Magma and the Relationship with IDDP-1

Appendix C: FTIR Images of glass chip showing location of transects

List of Tables

1 Introduction

1.1 Project Background

In May 2008, the geothermal well KJ-39 was drilled in the Krafla geothermal field, northern Iceland, targeting superheated fluids associated with the Hólseldar volcanic fissure, to be used for power production. The well reached a maximum depth of 2865 m (2571 m true depth) before the drill string became stuck, on the 16th October. After a week of unsuccessful attempts to free the string, it was eventually detached using explosives on the 23rd October and as it was returned to the surface, brought with it freshly quenched glass chips. The discovery of the glass chips, as well as downhole temperatures measured as high as 386 °C suggested that the well had intersected magma (Mortensen et al. 2010).

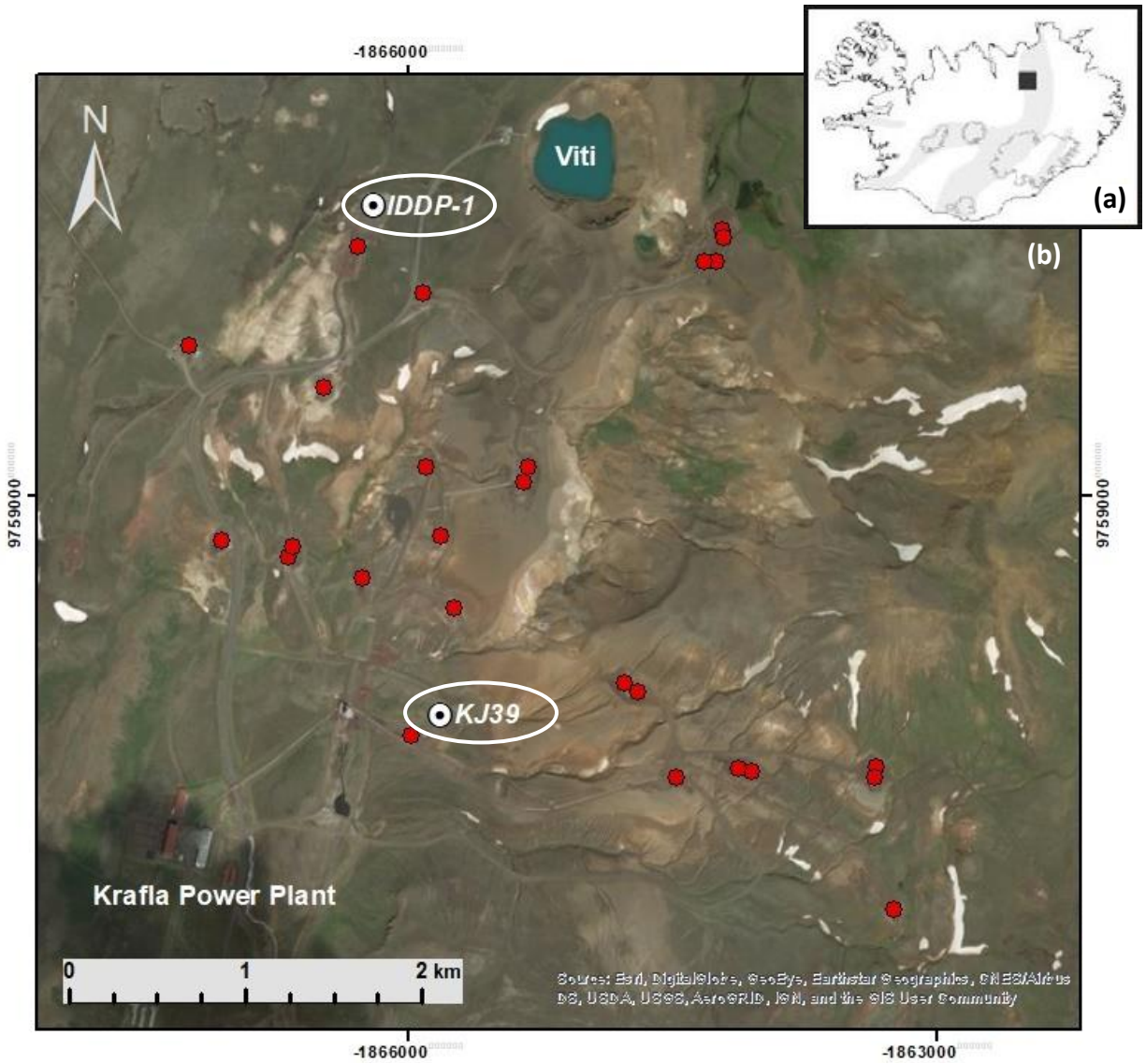

Fig 1.1: *(a) Location of Krafla in Iceland. (b) Location of well holes KJ-39 and IDDP-1 (circled) in relation to the Krafla Power Plant and Viti Crater (labelled). Red dots show the locations of other wells in the geothermal field (from Weisenberger et al. 2015). Basemap imagery is from ESRI through ArcMap.*

Similarly, during the drilling of a second well, IDDP-1, in 2009, high temperatures, drilling complications and glass chips returned in the drilling mud also suggested magma had been encountered. The cumulative evidence from both of these wells indicates that magma has been encountered at least twice in the Krafla geothermal region.

The glass that was recovered during the drilling of KJ-39 forms the basis of this project and is particularly interesting because it provides a unique insight into formation and magmatic processes affecting the magma body at depth, without any overprinting by eruption or slow cooling events. This project analyses the KJ-39 glass chips from the Krafla geothermal field for volatile components, specifically H_2O and CO_2, using Fourier Transform Infrared spectroscopy (FTIR) and major element concentrations, using Electron-Probe Micro-Analysis (EPMA) to determine the origin of the magma that was intersected and also investigate its degassing history. The results of this project were compared with the well-studied glass chips from the IDDP-1 well, located approximately 2.5 km to the north of KJ-39 (*Fig 1.1*), which also intersected magma in June of 2009, in order to determine the relationship between the two magmatic sources. If the magmatic source is similar for both wells this could constrain the size and extent of the Krafla magma chamber. Information about the geometry of the magmatic system below Krafla will have important economic implications for the geothermal field and will open up further geothermal drilling opportunities such as the Krafla magma testbed (Eichelberger 2019).

1.2 Thesis Objectives

The main goal of this thesis is to determine the petrographic origin of the magma that was intersected in the KJ-39 well and determine any relationship with the magma that was intersected in the IDDP-1 well. In order to achieve this, it has the following objectives:

- *Objective 1*: Review the literature on the magmatic context of the Krafla geothermal region and processes that effect melt composition.
- *Objective 2*: Measure major and volatile (S, Cl, F) element variations in the glass chips to examine evidence for magmatic processes such as melt injection, mixing, degassing and fractional crystallisation.

- *Objective 3*: Examine textural evidence for magmatic processes using thin sections and SEM backscatter images of crystals glass and vesicles in the glass chips.
- *Objective 4*: Use FTIR measurements to identify the H_2O and CO_2 concentrations and H_2O speciation in the glass chips.
- *Objective 5*: Compare glass major and volatile element (H_2O, CO_2, S, Cl, and F) chemistry and mineral assemblages with those from the published data on IDDP-1 magma chips.
- *Objective 6*: Discuss the magmatic processes and the relationship between the two magma bodies that have been intersected and whether they could be from the same or a similar source.

1.3 Chapter Overview

Chapter 2: **Krafla Geothermal Field and Previous Drilling**. This chapter will overview the geological setting of the Krafla geothermal field and the history of the geothermal industry in Krafla. It will also detail the drilling of both KJ-39 and IDDP-1 wells and provide a brief overview of the previous work done on the IDDP-1 glass cuttings (*Objective 1*).

Chapter 3: **Impact of Magmatic Processes and Volatiles on Melt**. This chapter will discuss the impact of magmatic processes such as fractional crystallisation, remelting and mixing as well as the degassing and regassing of volatiles in melts, focusing on H_2O and CO_2 as well as S, Cl and F (*Objective 1*).

Chapter 4: **Analytical Methods**. This chapter will outline the primary analytical methods used in this study and overview the preparation, analysis and data manipulation for each method.

Chapter 5: **Petrographic and Geochemical Results of KJ-39 Cuttings**. This chapter will present the results from the geochemical analysis using electron probe micro analysis (EPMA) and Fourier Transform infrared spectroscopy (FTIR) along with the textural analysis (*Objectives 2-4*).

Chapter 6: **Origin of KJ-39 Magma and the Relationship with IDDP-1**. This chapter aims to determine the origin of the KJ-39 sample set by interpreting the results in the previous

chapter. It will also compare the results with those from the IDDP-1 magma studies to determine any relationship between the magma sources. (*Objective 5 and 6*).

Chapter 7: **Conclusion**. This chapter will outline the key findings and future directions of the thesis.

2 Krafla Geothermal Field and Previous Drilling

2.1 Introduction

This chapter will outline the geological setting of the Krafla volcano and its associated geothermal field as well as detailing the history and extent of the geothermal drilling in the area. It will also introduce the drilling of the KJ-39 well.

2.2 Krafla Central Volcano Geological Setting

The Krafla central volcano is a very well-studied volcano in NE Iceland because of its expansive history of primarily tholeiitic eruptions, with both rhyolitic and basaltic phases. The magmatic context is summarized in (Kennedy et al. 2018). The most recent eruptive phase, the Krafla Fires, occurred from 1975-1984 (Einarsson 1991). The volcano is situated in Iceland's Northern Volcanic Rift Zone (*Fig 2.1*) and comprises a central volcano, with a diameter of approximately 15 km, intersected by a fissure swarm spanning approximately 100 km (Jónasson 1994). The volcano consists of predominantly hyaloclastites, basalts, formed before and after the last glacial period, and a few infrequent rhyolite lava domes (Tuffen & Castro 2009), which infill the collapsed caldera (Zierenberg et al. 2013; Mortensen et al. 2014). The rhyolitic volcanism at Krafla is frequently separated into two main phases along with a third, small-scale stage (Jónasson 1994). The initial phase, occurring at 100 ka, produced a minor rhyolite dome along with a silicic welded tuff, associated with the caldera formation (Björnsson et al. 1977, 1979; Calderone et al, 1990; Sæmundsson 1991). The next stage of rhyolite volcanism occurred between 25 and 13 ka, throughout the last glacial period (Sæmundsson 1991) producing three rhyolite ridges formed outside of the rim of the caldera (Jónasson 1994). The smaller, final stage of rhyolite volcanism combines several, minor eruptive events that occurred after the last glacial period, including the eruption of two rhyolitic layers of pumice at 9 ka as well as the emplacement of the Hrafntinnuhryggur obsidian ridge (Jónasson 1994). The latest eruption at Krafla was the Krafla Fires and the associated rifting episode, that occurred from 1975-1984 (Opheim & Guðmundsson 1989, Zierenberg et al. 2013). The fires, which consisted of nine volcanic eruptions along with subsidence and swelling of the caldera (Opheim & Guðmundsson 1989), were very similar to a previous event, the Myvatn Fires, a series of basaltic fissure eruptions occurring between 1724 and 1729 (Grönvold 1984) that formed the nearby Viti Crater (*Fig 2.2*) (Zierenberg et al. 2013).

2.3 Krafla Geothermal Field and Power Generation

The geothermal industry in Iceland is one of the largest contributors to power production, contributing approximately 30% of electricity production in Iceland, of which 90% is utilised for heating businesses and private homes (Nielsen et al. 2000). Because of the ever-increasing demand for cheap and efficient power, focus in recent years has turned to deeper, higher temperature exploratory wells to investigate for supercritical hydrothermal fluids. These supercritical fluids are expected to yield ten times the power of standard geothermal fluids in Iceland (Friðleifsson and Elders 2005), thus are of particular interest to energy companies.

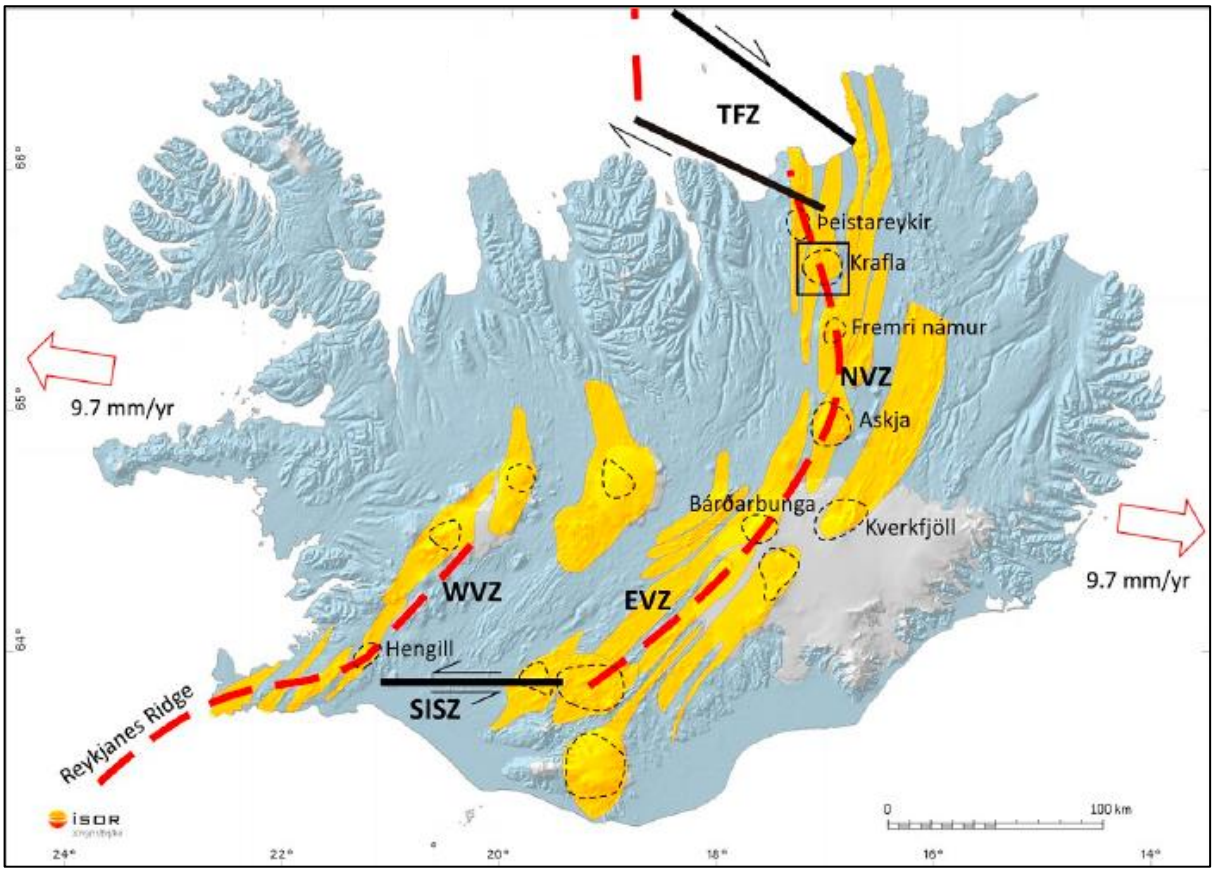

***Fig 2.1**: Location of Iceland's volcanic zones showing the location of the Krafla geothermal field (Black Square) and major spreading centres (red dotted lines). NVZ – Northern Volcanic Zone, WVZ – Western Volcanic Zone, EVZ – Eastern Volcanic Zone, SISZ – South Iceland Seismic Zone, TVZ – Tjörnes Fracture Zone. The WVZ and EVZ are connected by the SISZ (Sturkell et al. 2010). Yellow zones are fissure swarms. Dotted circles show the location of central volcanoes. Figure from Árnason (2020).*

Krafla volcano has been extensively studied because of the presence of several active geothermal systems within the caldera as well as its eruptive history in the era of scientific study. The Krafla geothermal field covers an area of approximately 40 km^2 and is associated with the peripheries of the Krafla magma chamber located 3 to 7 km below the surface

(Einarsson 1978). It is one of the most complex geothermal fields in Europe because of the distribution of two-phase zones (liquid and gas phase water) overlain by single phase, compressed liquid (Bodvarsson et al. 1984).

Geothermal exploration of the Krafla geothermal field began in 1974 with drilling of exploratory wells. In only the second year of operation however, the eruption of the Krafla Fires, 1975-84, complicated the expansion and exploration of the area and threatened to shut down the whole operation (Einarsson 1991). Fortunately, there were no lava flows into the Hlidardalur valley, where the development of the first power plant was underway (Júlíusson et al. 2005). The first power production from the field occurred in 1977 and by 1996 demand was sufficient to warrant the need for a second steam turbine. Since then the demand for geothermal power has increased significantly due to expanding usage in both the domestic and industrial sectors. The Krafla geothermal power plant is currently the largest power plant in Iceland, comprising 33 active wells, while 43 exploration wells have been drilled in total (Weisenberger et al. 2015). The plant is currently capable of producing 500 GWh of electricity per year.

The geothermal field itself is comprised of four well fields, three of which have been exploited; Leibortnar-Vítismór, Suðurhliðar and Hvíthólar (*Fig 2.2*) and Vesturhlíðar, which has not yet been exploited. Each of the well fields are characterized by the differing physical properties of the rocks and characteristics of the geothermal fluids (Mortensen et al. 2010). The Leibortnar-Vítismór field is divided into an upper water saturated reservoir, approximately 1500 m thick with temperatures ranging from 190-220 °C and a lower boiling reservoir that reaches temperatures as high as 350 °C. The Suðurhliðar field is also a boiling reservoir. The Vesturhlíðar field makes up the peripheries of the Leibortnar-Vítismór and Suðurhliðar fields and is a key up-flow zone in the larger Krafla system *(Fig 2.3)*. Finally, the Hvíthólar field is characterized by boiling conditions down to 900 m depth then temperature reversal below that and is located within the southern caldera rim (Mortensen et al. 2010). Temperature conditions in the upper 1200 – 1500 m of these fields vary considerably (Mortensen et al. 2014) but the base of the geothermal field is characterized by boiling conditions, where temperatures can be as high as 350 °C at 2000 m depth. These high temperatures were measured at slightly greater depths (2.1 and 2.5 km respectively) in wells IDDP-1, in which 430 °C was measured, and KJ-39, in which 385.6 °C was measured.

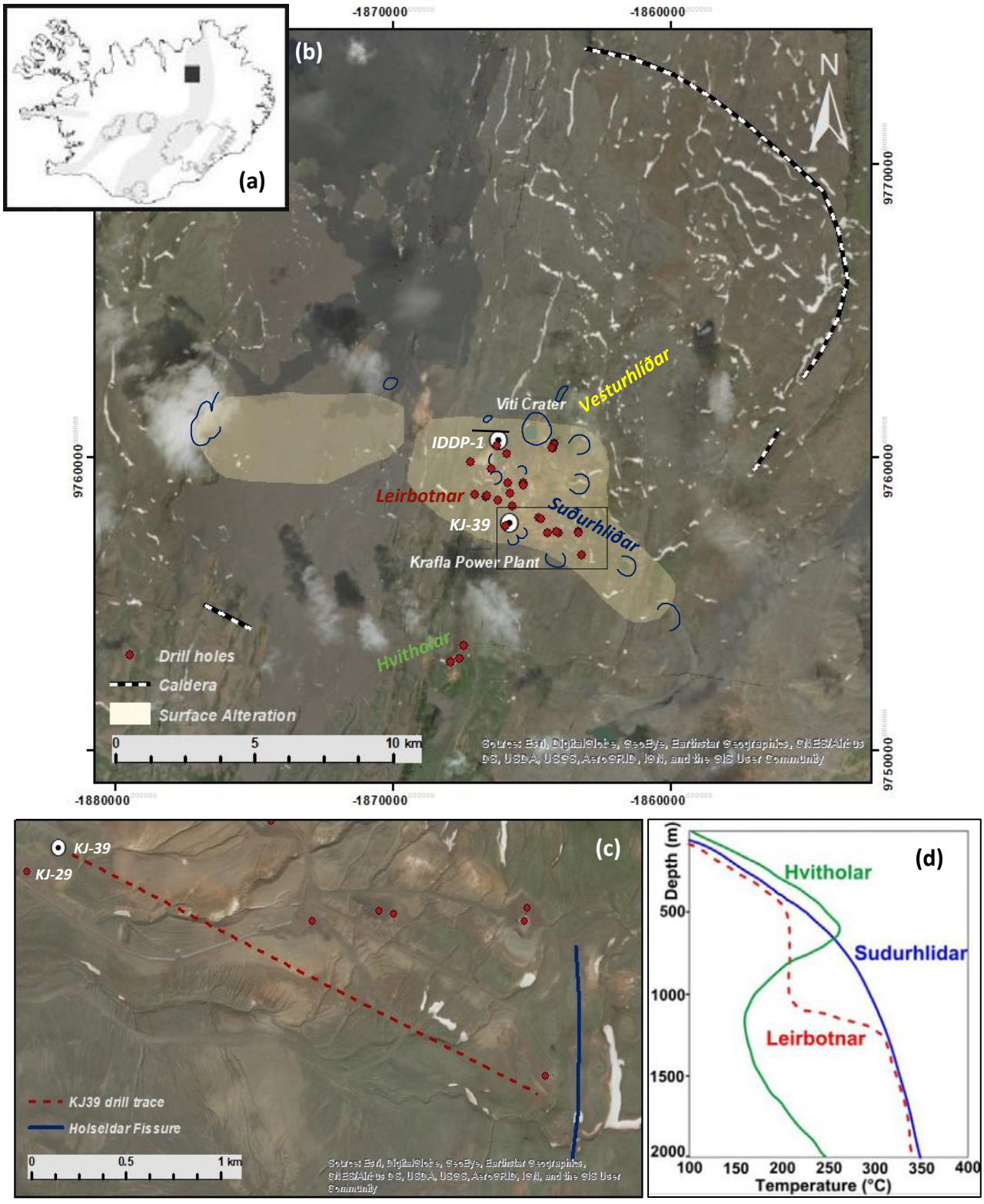

***Fig 2.2**: (a) Location of Krafla in Iceland. (b) Location of the wells in the Krafla geothermal field (Weisenberger et al. 2015). Dotted line shows the outline of the Krafla caldera and the yellow shape shows the areas of surface alteration inferred as the Krafla magma chamber (from Sæmundsson 1991). Labelled are the locations of three exploited geothermal zones in the Krafla area as well as Vesturhlíðar that has not been exploited. Blue lines show craters, black solid line shows the location of the cross section in Fig 2.3. (c) Zoomed in view of boxed area in (b) showing the location of the Hólseldar Fissure and the surface trace of the KJ-39 well (from Langella et al. 2017). (d) Temperature profiles from the three exploited well fields at Krafla (modified from Ármannsson et al. (1987). Basemap imagery from ESRI through ArcMap.*

These two wells displayed such high temperatures because they both intersected magma at their maximum depths (Mortensen et al. 2010, Zierenberg et al. 2013). On both occasions, quenched glass chips were returned to the surface, allowing unique insights into the formation processes and evolution of these magma bodies.

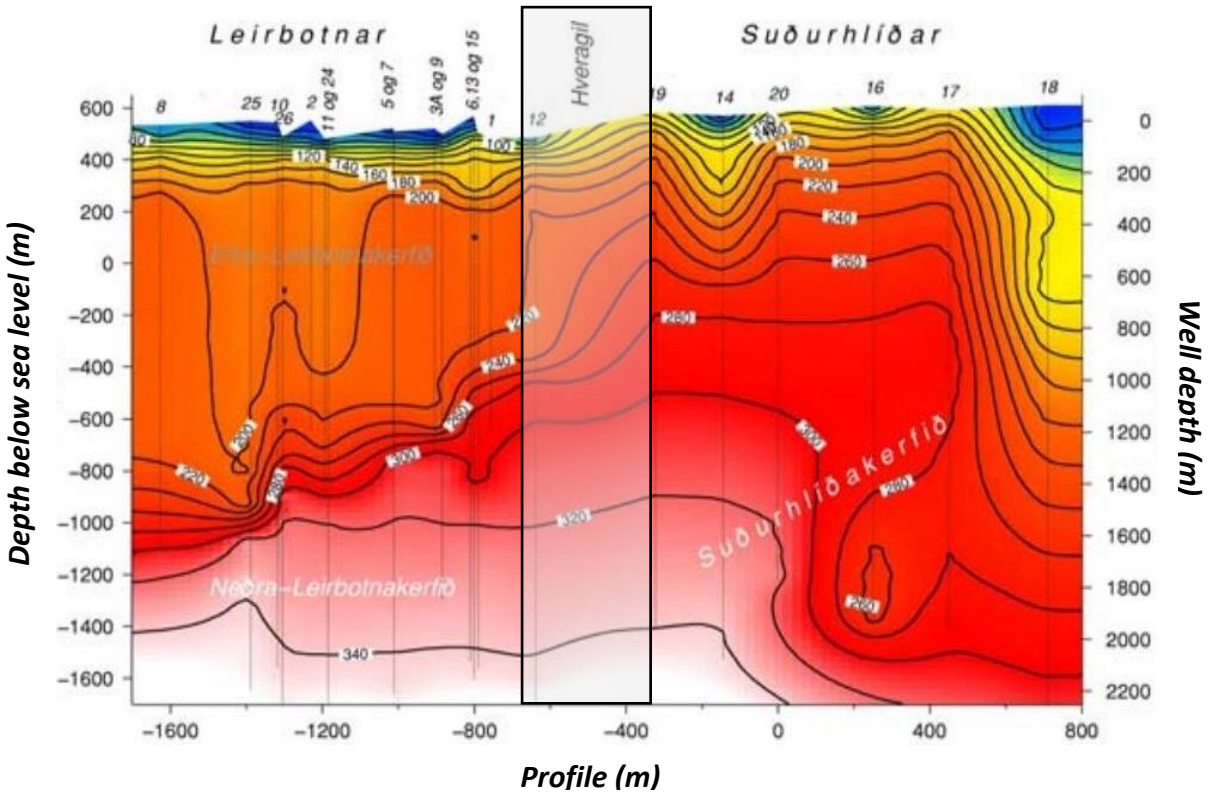

Fig 2.3: *Temperature distribution across the Krafla geothermal fields Leirbotnar and Suðurhliðar in a W-E orientation. The black box shows the main zone of up flow at Hveragil that is a key target for geothermal drilling. The x axis represents the distance across the profile in meters, with 0 showing the location of the IDDP-1 well. The location of this cross section is shown by the solid black line in Fig 2.2. Figure modified from Elders et al. 2003.*

2.4 Magma Drilling

Although drilling into magma is a rare occurrence, it has been recorded to have happened during geothermal drilling for energy generation five times, in various countries (Reinsch et al. 2017). As well as the two occurrences at Krafla, a dacitic magma was intersected during drilling on Hawaii, USA, in 2005, in well KS-13 at a depth of 2500 m (Teplow et al. 2009). In addition, two wells in the Menengai geothermal field, Kenya, MW-04 and MW-06, hit magma at approximately 2.1 and 2.2 km respectively during geothermal drilling in 2011 (Mbia et al. 2015).

2.5 KJ-39

2.5.1 Drilling

Well KJ-39 is located in the south of the Leibortnar-Vítismór field on the same drilling site as another geothermal well, KJ-29, but was drilled directionally to the east at a bearing of 115° and an angle of 30° (*Fig 2.4*) into the Suðurhliðar field (Mortensen et al. 2010). The aim of the KJ-39 well was to target the permeability known to be associated with felsic intrusions in order to access any supercritical fluids circulating the permeable rocks and to investigate any fluids surrounding an explosion crater and the Hólseldar volcanic fissure (*Fig 2.4*). All depths mentioned in the following section represent depth down hole, rather than depth below the surface.

The well was pre-drilled and cased in May 2008, and then drilled and cased to a depth of 973.7 m in July of the same year. The third phase of drilling began in September 2008 and well KJ-39 reached its maximum depth of 2865 m a few weeks later (ISOR 2009). There was 100% recovery of the drill cuttings through the topmost section of the well, which was made up of successions of altered hyaloclastite and basalt, to a depth of 1400 m. This upper succession shows significant alteration with the presence of quartz, epidote, wollastonite and actinolite suggesting alteration in the epidote-actinolite zone. Between 1404-2654 m depth, the well entered an intrusive complex in which recovery significantly decreased because of almost complete loss of circulation and below 2654 there was no recovery of cuttings at all. Mortensen et al. (2010) grouped this intrusive complex into three sequences; a basaltic dyke sequence at 1400-1500 m depth, felsic and intermediate intrusives between 1500-2000 m and a doleritic/gabbroic sequence below 2000 m. Below 2000 m, the basaltic intrusive complex is dense and mostly unaltered, unlike the above section which displays an alteration assemblage comprised of quartz, epidote, wollastonite and actinolite (Mortensen et al. 2010). Drilling observations highlighted that rocks in the depth range 2827-2847 m were much softer than the above successions, before the well reached its maximum depth of 2865 m (ISOR 2009). Shortly after the completion of the well and drilling was ceased, the drill string got stuck, on the 15th October 2008, at a depth of 2848 m and remained stuck for approximately a week before it was eventually released, with the aid of explosives, at a depth of 2808 m. The three lowest units that were recovered in the bottom hole assembly (BHA) contained drill cuttings (*Fig 2.5a*). These cuttings contained approximately 30% freshly quenched glass, which together with the incredibly high temperatures measured at the base of the well, 385.6° C, suggested that the well had likely intersected magma (Mortensen et al. 2010).

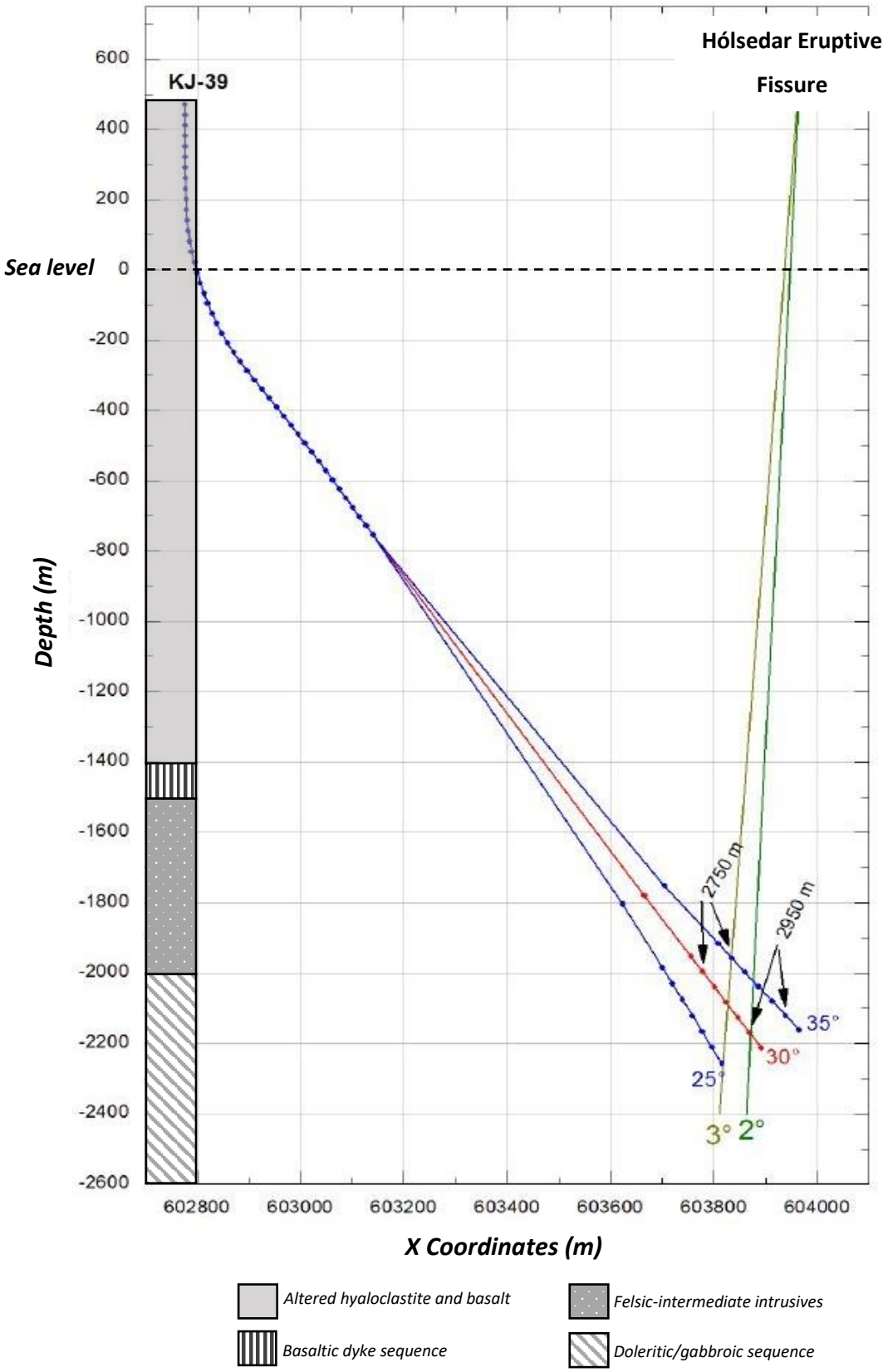

Fig 2.4: *Schematic drill pattern for KJ-39 from the drilling report (ISOR 2009). The red line shows the actual path that the well followed and the two blue lines show the pattern if drilled plus or minus 5°. The green line shows the geometry of the Hólsedar volcanic fissure that the well was designed to investigate. Log on the left shows simplified lithology of the KJ-39 well.*

Along with the glass that was retrieved from the base of the well, there were also resorbed minerals of plagioclase, clinopyroxene and titanomagnetite (Mortensen et al. 2010).

The gases from the Krafla magma chamber may have impacted the thermodynamic and chemical properties of the geothermal fluids circulating the magma and together with the high temperatures, and the close proximity to magma, meant that the well was considered unsuitable for sufficient steam generation. Any fluids circulating in the system would likely be acidic and may cause further damage to the well and the drilling equipment, as shown in *Fig 2.5b* (Bodvarsson et al. 1984, ISOR 2009, Mortensen et al. 2010). Shortly after the cuttings were retrieved from the BHA, the well was plugged with cement up to 2620 m.

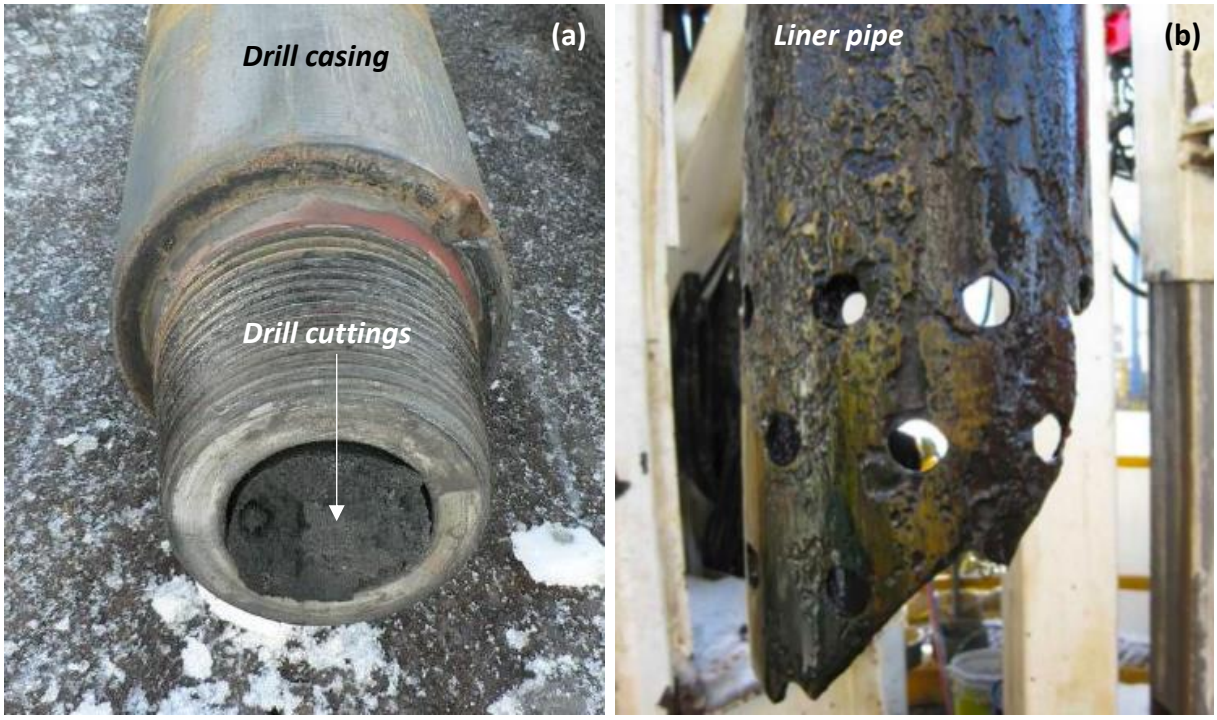

Fig 2.5: *Images of KJ-39 equipment following intersection of magma (a) Drill casing containing cuttings that were retrieved from the BHA when the drill string was freed from well KJ-39. Image from drilling report (ISOR 2009). (b) Heavy corrosion of a liner pipe from the KJ-39 well (Thorbjornsson 2016).*

2.6 Iceland Deep Drilling Project (IDDP)

2.6.1 Project Background

Approximately six months after the KJ-39 well hit magma, a second well in the Krafla region, also intersected magma. The Iceland Deep Drilling Project (IDDP) is a project focusing on supercritical, high energy yielding fluids and is an industry-government collaboration with the

purpose to investigate the use of these supercritical fluids for geothermal energy (Elders et al. 2011).

2.6.2 Drilling

The IDDP-1 well was designed to drill down to a depth of approximately 4-5 km to explore for supercritical hydrothermal fluids (Friðleifsson et al. 2010). The depth and location of this exploratory well was chosen based on S wave shadowing by Einarsson (1978) and magneto telluric surveys that identified two shallow lobes that the IDDP-1 well was to drill between (Elders et al. 2011, Zierenberg et al. 2013) that indicated that the magma chamber sat at a depth of around 3-7 km. Pre-drilling of the well began in June 2008 where the hole was drilled to a depth of 87 m over a period of nine days and cased (Hólmgeirsson et al. 2010). Drilling continued on and off, over a period of six months until the well reached a depth of 2000 m below the surface in May 2009. In April of the same year, the drill bit hit unexpected difficulties around 2100 m causing the well to be sidetracked twice. This initial well, IDDP-1A, reached a depth of 2102 m and became stuck. Drilling operators were unable to retrieve the drill string, so it was abandoned, and a sidetrack drilled. On the 8th June, the sidetracked well IDDP-1B, reached a depth of 2103.4 m and became stuck again. A second sidetrack, IDDP-1C, reached a depth of 2104.4 m on the 24th June (Friðleifsson et al. 2010) and was pushed back up the well by magma. Silicic glass fragments *(Fig 2.6)* were collected from a depth of 2095 m, confirming the presence of magma at around 2100 m (Friðleifsson et al. 2010). After completion of the well in July 2009, the well was injected with cold water until it was allowed to heat up from August 2009. The IDDP-1 well was producing energy between March 2010 and July 2012 and during this time became a very efficient energy producing bore hole. At its peak, temperatures observed were as high as 440 °C (Ingason et al. 2014) and the well was capable of producing between 25 and 36 MW (Gylfadóttir et al. 2012, Ingason et al. 2014). Eventually, after experiencing problems with the corrosive and erosive properties of the steam and extreme temperatures, the well was cased in July 2012. The Iceland Deep Drilling Project itself continues at a different site in Southern Iceland, targeting geothermal waters of the Reykjanes reservoir with drilling of the IDDP-2 well (RN-15). The IDDP-2 well reached a depth of approximately 4600 m in January 2017 and measured temperatures as high as 535 °C at the base of the well (Kruszewski & Wittig 2018). Plans to revisit the Krafla IDDP-1 site are underway as the Krafla Magma testbed project (Eichelberger 2019).

2.6.3 Stratigraphy and alteration of IDDP-1

The IDDP-1 well drilled through geological units consisting mainly of basalt and dolerite down to a depth of approximately 2030 m, which then become increasingly more felsic to a depth of 2070 m. Below this depth, the well encountered a zone where there was complete loss of circulation for approximately 30 m, before the drill encountered the magma. This blind zone, as it is referred to in the drilling industry, means that it is difficult to determine the lithology of the rocks directly above the magma, however, density gamma logs suggest that it is likely felsite (Mortensen et al. 2015).

Because of the extent of the Krafla geothermal field, much of the strata surrounding the Krafla magma chamber is altered to some extent. Mortensen et al. (2014) analysed the alteration mineral assemblages present in the IDDP-1 well and identified alteration zones based on changes in temperature and the assemblage of minerals present. Overall, the degree of alteration increases with depth down the well, with the exception of the uppermost lava flows which are highly altered, although this is likely the result of surface alteration and weathering processes (Mortensen et al. 2014).

Table 2.1*: Overview of the alteration zones identified by Mortensen et al. (2014) outlining the depth, alteration zone and the alteration minerals present in each zone.*

Depth (m)	Alteration Zone	Minerals Present
0-90	Zeolite-Smectite Zone	Low temperature zeolite, smectite, calcite, pyrite.
90-300	Mixed Layer Clay (MLC)	Heulandite, stilbite, calcite, pyrite, quartz, wairakite.
300-510	Chlorite Alteration Zone	Chlorite
510-930	Epidote-Chlorite Alteration Zone	Epidote, prehnite, chlorite, quartz, calcite, pyrite, laumontite.
930-1950	Epidote-Actinolite Zone	Actinolite, garnet, wollastonite, pyrrhotite, iron-oxides (magnetite), chlorite, quartz, Cu-Fe sulphides.
1950-2070	Scarce Zone	Some small amounts of amphibole, garnet, magnetite, actinolite.

Table 2.1 outlines the alteration zones identified in the well and the alteration minerals present. Calcite is the most abundant mineral in the top 950 m but below this depth the abundance diminishes significantly. Some small amounts of calcite are present as veins up until 1600 m depth. Pyrite and quartz are also abundant in the upper 1 km of the well with minerals such as

epidote, actinolite, zeolite and clays also present but not as abundant. Below 1950 m the abundance of alteration minerals decreases significantly with only small amounts of amphibole, garnet, magnetite and possible quartz and actinolite. In the scarce zone, the intrusions encountered during drilling are relatively young and thus may be the reason for the scarcity of alteration minerals, although the base of the well is considered to be a superheated steam zone which may also contribute to the lack of minerals (Mortensen et al. 2014).

2.6.4 Previous Study of IDDP-1 Cuttings

A study by Saubin et al. (2020, In Review), investigated the texture of the glass chips based on the time that the chips were received at the surface of the well after drilling stopped at a depth of 2104 m. The study found that the cuttings retrieved during the first two hours of collection were comprised of 70% felsite and 30% glass, after which 100% of the cuttings were glass. The glass that was returned to the surface initially was composed of 45% clear glass, which reduced to 15% after two hours, with the rest comprising brown glass, until drilling mud circulation stopped. The percentage of vesicles also changed after the first two hours of retrieval, from 60% to <20% and corresponds with the change of colour of the chips (Saubin et al. 2017) *(Fig 2.6)*.

The mineral and glass chemistry of the cuttings has been analysed, as well as volatile components, indicating the existence of multiple melt batches within a very tight range of major elements and volatiles (Zierenberg et al. 2013; Masotta et al. 2018; Watson 2018; Saubin et al. 2020 in review). The major and trace element composition of the glass is in accordance with an origin of partial melting of hydrothermally altered basaltic crust at depth (Elders et al. 2011), however Masotta et al., (2018) concluded an origin of variable amounts of partial melting of felsite. This is in agreement with the identification of three batches of melt separated based on their petrography (Zierenberg et al. 2013). Melt-1 and Melt-2 were identified as high silica rhyolites, although Melt-2 contains lower Ca and higher K than Melt-1. Melt-1 has a similar composition to the host felsite that was also retrieved at the surface. Melt-2 has a higher water content, interpreted as the result of a higher degree of partial melting (Masotta et al. 2018), although a few Melt-2 samples showed evidence of hydration, likely because of the interaction with fluids used during drilling as the melt was quenched. Melt-3 is thought to be the result of mixing between Melt-1 and Melt-2, although it possesses an anomalously high silica content. This high silica is considered to be due to the resorption of quartz during partial melting of the felsite (Zierenberg et al. 2013).

The phenocryst assemblage is comprised of plagioclase, augite and pigeonite with minor quartz and micro-phenocrysts (0.1-1 mm) of titanomagnetite and apatite that are present as inclusions in the plagioclase. The in-situ temperature of the IDDP-1 magma is between 850 and 920 °C, calculated using two-pyroxene geothermometry and crystallisation models (Zierenberg et al. 2013).

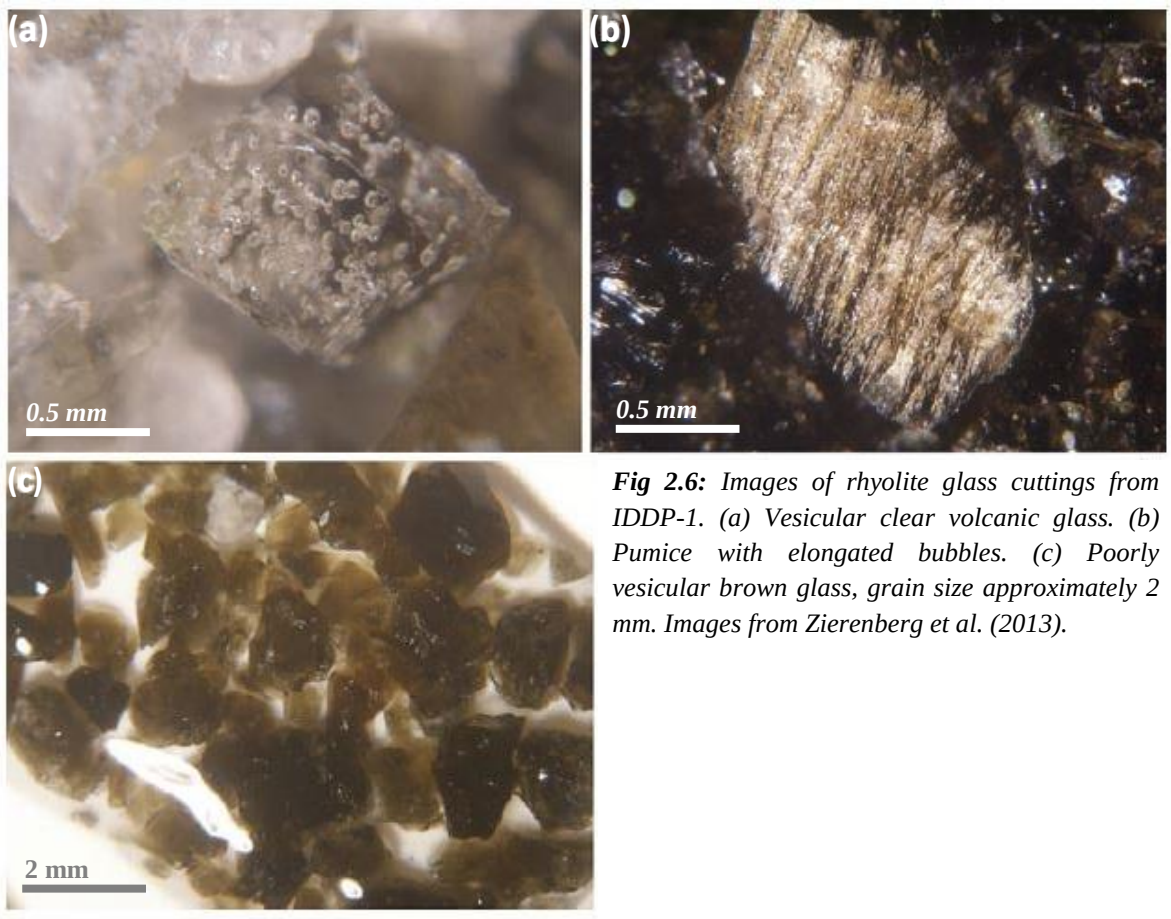

Fig 2.6: *Images of rhyolite glass cuttings from IDDP-1. (a) Vesicular clear volcanic glass. (b) Pumice with elongated bubbles. (c) Poorly vesicular brown glass, grain size approximately 2 mm. Images from Zierenberg et al. (2013).*

The volatile components of the glass chips were analysed by Zierenberg et al. (2013) and showed total H_2O contents ranging from 1.40 to 2.15 wt% with high OH/molecular H_2O (mH_2O) suggesting a predominately magmatic origin. Watson (2018) also analysed the volatile contents of the IDDP-1 cuttings with the aim to understand how the magma responded to the drilling itself, over time. As the glass chips were received at the surface over the drilling period, there is a slight increase in the concentration of total H_2O as well as a significant increase in CO_2 content. There was also a significant increase in the OH/mH_2O, supported by the high percentage of vesicles in the earliest retrieved samples that decreased significantly with time. OH content was higher than mH_2O in most of the cuttings analysed, agreeing with the

conclusion of Zierenberg et al. (2013) that the water was of magmatic origin, rather than hydration caused by the drilling fluids (Watson 2018).

2.7 Summary

Activity in the Krafla geothermal field has been ongoing since the 1970s and focus in recent years has turned to supercritical fluids that yield more energy than standard geothermal fluids. The geothermal wells KJ-39 and IDDP-1 were both planned to target these supercritical fluids, KJ-39 targeting the permeable zone around felsic intrusions and IDDP-1 targeting the peripheries of the Krafla magma chamber. Both wells unexpectedly encountered magma at reasonably shallow depths (between 2100 and 2600 m) and quenched glass was returned to the surface. The IDDP-1 glass cuttings are rhyolitic in composition with SiO_2 content averaging 76.5 wt% and a mineral assemblage consisting of plagioclase, augite, pigeonite and quartz (Zierenberg et al. 2013). The KJ-39 well hit magma at an inclined depth of 2865 m (2571 m below the surface) and temperatures were measured at 386 °C. This project analyses the petrography of the glass chips and minerals that were returned from the KJ-39 well and compares them with the cuttings of the IDDP-1 well to determine the origin of the magma and the relationship within the wider Krafla region.

3 Impact of Magmatic Processes and Volatiles on Melt

3.1 Introduction

Magmatic processes such as fractional crystallisation, remelting and mixing are key factors that determine the end composition of the magma that will eventually erupt or cool, or in this case, be intersected. Volatiles are also important components for melt composition and can contribute up to 10 wt% of the total composition of melts (Sparks 1978). This chapter outlines the impact that these magmatic processes and volatiles have on melts, focussing specifically on the two most abundant volatiles H_2O and CO_2, and the quenching of magma.

3.2 Magmatic processes

3.2.1 Fractional crystallisation

Fractional crystallisation is a very prevalent process occurring in igneous rocks worldwide and is often the reason for patterns seen in major element variation diagrams. Typically, mafic minerals such as olivine and pyroxene crystallise first followed by the intermediate minerals, such as plagioclase, then finally the more felsic minerals like quartz, according to Bowen's reaction series (Bowen 1956). Therefore, as the magma cools, it becomes progressively more felsic or evolved in composition. Variation diagrams are very helpful to identify the extent of fractional crystallisation. Negative correlations or inflections in the trend indicate the entry of a new phase crystallising from the melt and thus being removed from the magma (Rollinson 1993). Fractional crystallisation is well recognised in Iceland, and is the process often attributed to the formation of rhyolites found in the Krafla region, including those formed by the 1875 Askja eruption (MacDonald et al. 1987).

3.2.2 Partial melting and assimilation

The process of assimilation is the chemical evolution of magma that occurs because of interaction with, and entrainment of the host rock material through which the magma is intruding. It is a common process occurring in magma bodies across the world, especially those that ascend through continental crust, and cause partial melting and entrainment of the surrounding country rock. Analysis of the major element composition of phenocrysts and comparing these with the composition of the host glass can determine if the rock has partially melted and/or interacted with surrounding country rock (Tindle & Pearce 1983). If the crystal and glass are in equilibrium, then it is probable that the phenocryst was formed from a melt of

the same composition. If the glass and crystals possess very different compositions however, then the crystal may have been entrained into the melt via assimilation and likely originated from a different source of magma (Simon et al. 2014).

3.2.3 Magma mixing

Magma mixing is the process whereby two or more isolated magma bodies, usually with somewhat differing compositions, mix and create a new magma with a separate composition. In order for these magmas to mix entirely and efficiently, the magmas should be similar in rheology, or have become similar by the time that they mix. Mixing can occur whenever there is a chemical gradient within the magmatic environment, which can be caused by processes such as replenishment of a magma chamber, fractional crystallisation and assimilation (*Fig 3.1*) (Perugini & Poli 2012, and references therein).

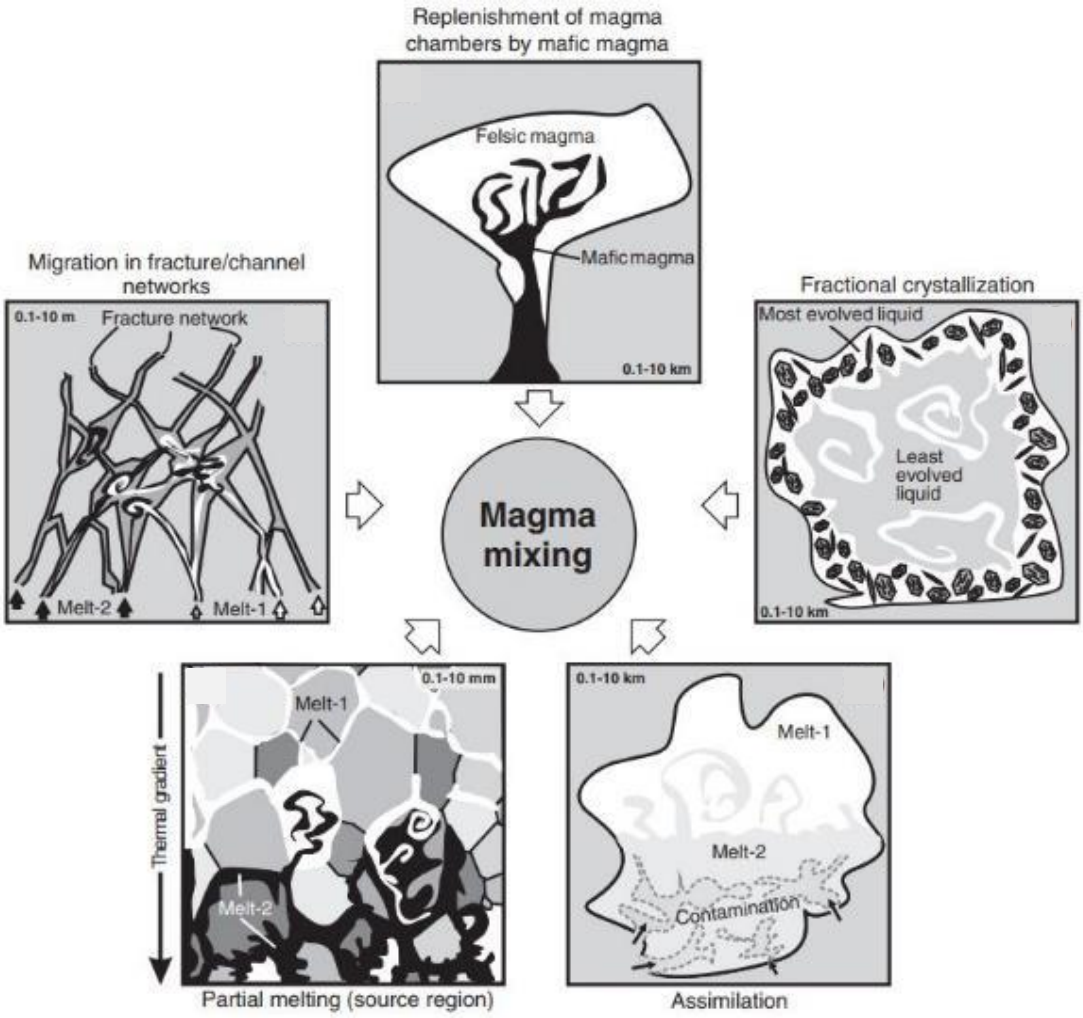

Fig 3.1*: Schematic diagram representing the processes that can generate compositional gradients in igneous environments and allow the mixing of magmas. Figure from Perugini and Poli (2012), modified from De Campos et al. 2011).*

The amount of mixing between the batches depends on the time that the batches are interacting, the size of the batches and differences in compositions (Walker et al. 1979). Evidence for magma mixing is often present as a linear trend on the binary variation diagrams if complete mixing has occurred but can also be represented by scatter if the process of mixing is not complete (Rollinson 1993).

3.3 Volatiles

3.3.1 Water

H_2O is the most important and most abundant volatile in the Earth's crust and can be found in concentrations as high as 10 wt% in rhyolitic melts at high temperatures (1073 K) and pressures (500 MPa) (Johannes & Holtz 1996). Dissolved H_2O has a profound effect on the physical properties of the melt and thus knowing the concentration is important to understand the processes.

3.3.2 Water speciation

Total dissolved H_2O (H_2O_t) is present in silicate melts both as OH groups and molecular H_2O (mH_2O) (Stolper 1982a) and the ratio of the two is strongly influenced by temperature and pressure. The two species can interchange via the equilibrium reaction (*Equation 3.1*):

[3.1]

$$mH_2O\ (melt) + O^{2-}\ (melt) \rightleftharpoons 2OH\text{-}\ (melt)$$

Where O represents an oxygen in the melt framework, mH_2O is molecular water and OH represents hydroxyl groups. Under equilibrium conditions, generally the concentration of mH_2O increases slowly with H_2O_t content at low H_2O contents and more rapidly as the total H_2O content climbs. Conversely, the concentration of OH increases rapidly as the total H_2O content increases at low H_2O contents, and more slowly at high H_2O_t contents *(Fig 3.2)* (Stolper 1982a, Burnham 1975). The exact value that this transition occurs at is dependent on the composition and temperature of the magma.

The equilibrium constant, *K*, of this reaction is a representation of the proportion of the two species expected to be present based on a range of given conditions such as temperature, pressure and melt composition. The equilibrium constant K is defined as the following:

[3.2]

$$K = \frac{X_{OH}{}^2}{X_{mH2O} X_O}$$

X represents the mole fractions on a single oxygen basis. *K* determines the relative proportions of the species mH_2O and OH for a given H_2O_t content while the system is in equilibrium. A higher *K* value means a higher concentration of OH and thus the system requires heat input to break the bonds (Stolper 1982a; Stolper 1989).

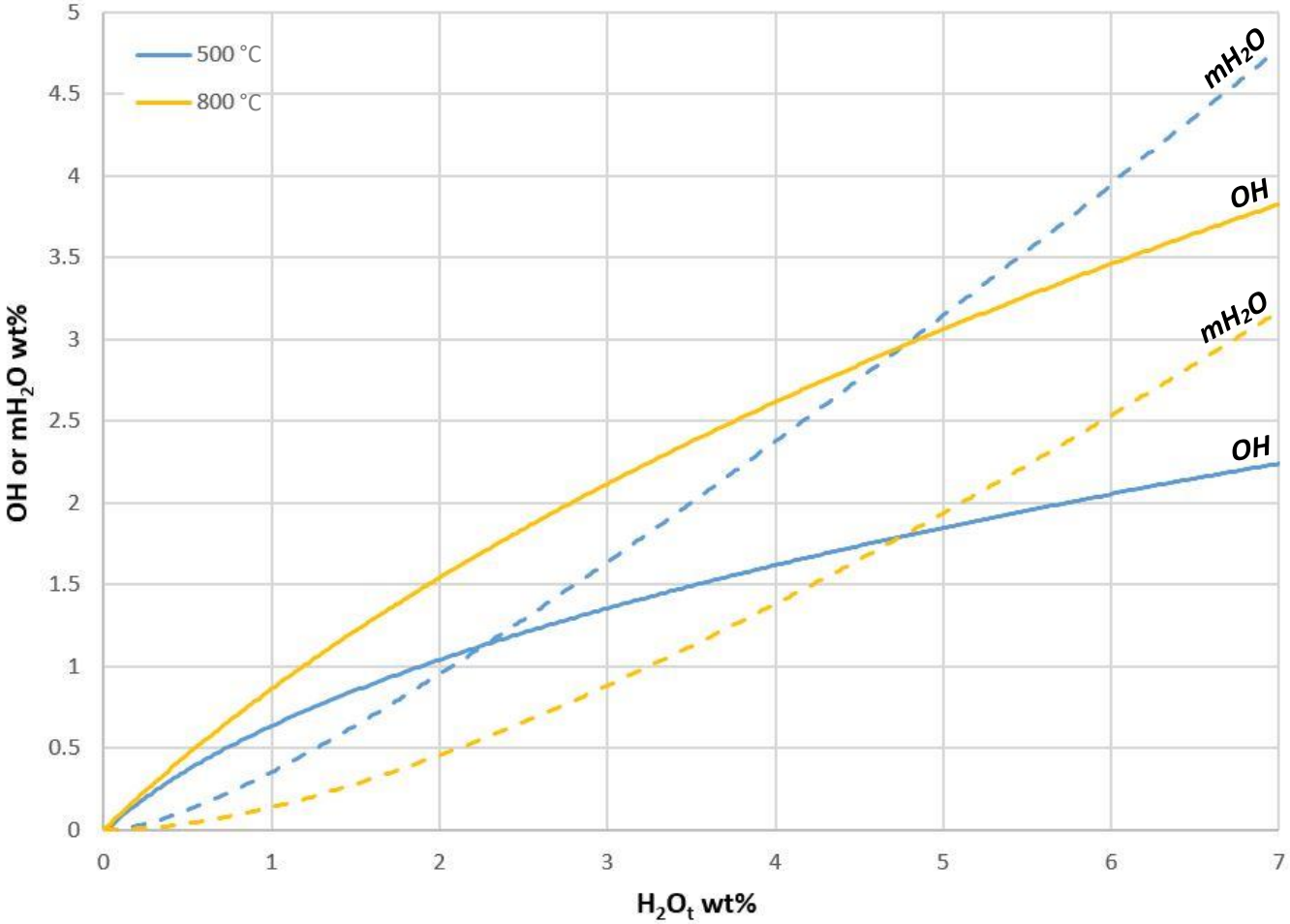

***Fig 3.2**: Variation in equilibrium speciation with temperature and total water content. Speciation model taken from Nowak & Behrens (2001) and K calculated using oxide compositions of the KJ-39 cuttings. Solid line represents OH concentration and dotted line represents the mH_2O concentration, blue shows speciation at 500 °C and yellow at 800 °C.*

At magmatic temperatures (~500 – 1300 °C), H_2O entering the silicate structure will react with bridging oxygen atoms to form OH and mH_2O. As the temperature drops, the reaction moves towards the left of the reaction (*Equation 3.1*) and any H_2O in the glass, or being added to the

system, favours mH_2O (Nowak & Behrens 2001). This is shown by *Fig 3.2*, displaying the effect of temperature on the speciation of H_2O.

3.3.3 Hydration and rehydration of volcanic glass

Most volcanic glass contains trace amounts (0.1-0.6 wt%) of dissolved magmatic H_2O. Hydration below magmatic temperatures, will not allow the system (*Equation 3.1*) to reach equilibrium, so the H_2O remains as mH_2O because there is insufficient energy to break the bonds required to form OH molecules. Therefore, when H_2O is added to the system, mH_2O increases but OH remains the same. Hydrated samples are characterised by higher mH_2O and lower OH than a given model at a specific total H_2O content (Seligman et al. 2016).

After the magma is erupted, quenched to glass and in some cases deposited, H_2O (e.g., meteoric water or seawater, depending on the environment) can enter the glass structure predominantly as mH_2O, a process known as secondary hydration or rehydration (Seligman et al. 2016).

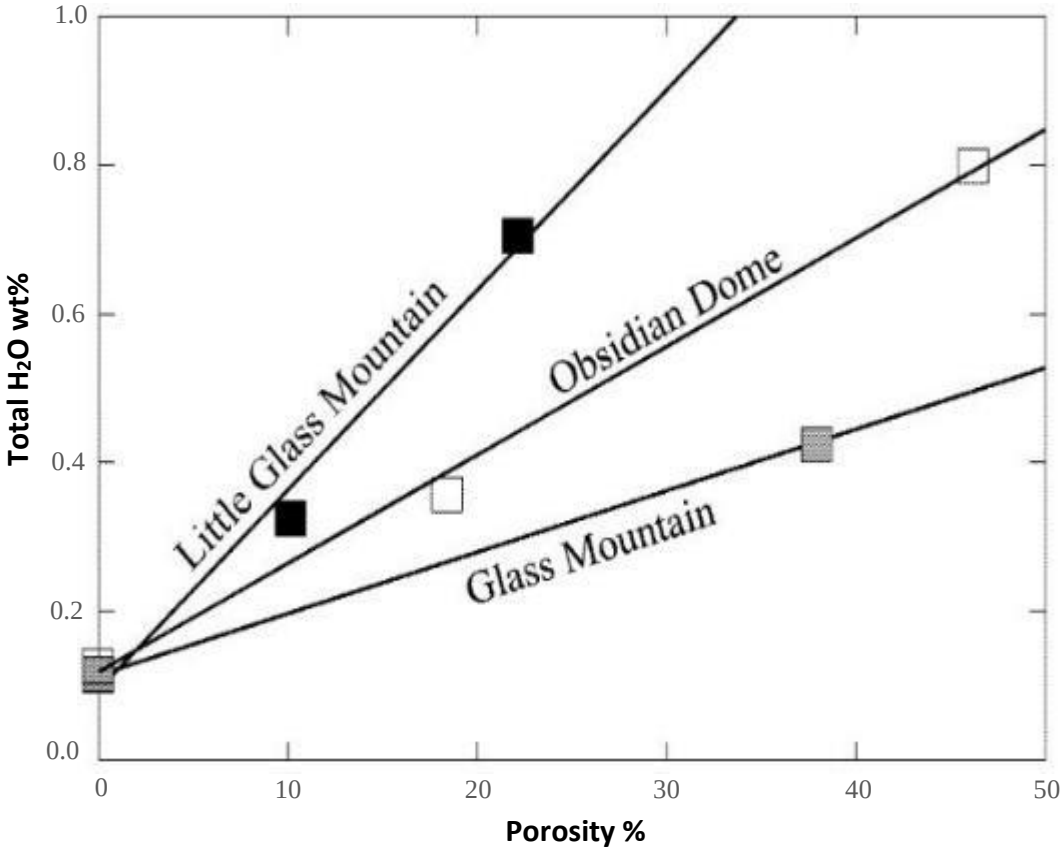

***Fig 3.3**: Total water content plotted against porosity (helium-accessible porosity, a measure of connected vesicle porosity) of three lava flow samples from DeGroat-Nelson et al. (2001).*

The diffusion coefficients of H_2O in volcanic glasses are strongly influenced by H_2O concentration, therefore secondary hydration occurs through the creation of a 'hydration front' that often has a sharp interface and can sometimes be observed under a microscope (Seligman et al. 2016). When H_2O is added to a volcanic glass a hydration layer can form along each of the exposed surfaces. Any mH_2O already in the glass then diffuses into the centre because it is 'drier' than the exterior and a 'hydration rind' forms at the exposed surface (Friedman & Long 1976; DeGroat-Nelson et al. 2001).

The extent of secondary hydration that the sample can experience is dependent on the surface area, so a highly vesicular glass with interconnected bubbles is capable of absorbing more water than a sample with no bubbles (DeGroat-Nelson et al. 2001). Connected porosity can be plotted against H_2O_t content, to show that H_2O is proportional to the porosity (*Fig. 3.3*) although the slope may vary depending on variations in magma chemistry.

3.3.4 CO_2 speciation

CO_2 is the second most abundant volatile in silicate melts, after water, and therefore is important in degassing processes (Eggler 1973). It is present in melts as two species, molecular CO_2 (mCO_2) and carbonate groups (CO_3^{2}) (Stolper & Ahrens 1987). The two species interchange as below:

[3.3]

$$mCO_2\ (melt) + O^{2}\ (melt) \rightleftharpoons CO_3^{2-}\ (melt)$$

The carbonate groups (CO_3^{2-}) impact the melt by interacting with the cations in the silicate network, while molecular CO_2 does not have any effect on the structure because it is a neutral molecule (Lowenstern 2001). The equilibrium constant *K* for CO_2 is (Zhang et al. 2007):

[3.4]

$$K = \frac{X_{CO32-}}{X_{mCO2}X_{O2-}}$$

Unlike the speciation of H_2O, which is strongly dependant on H_2O_t content, the ratio of CO_2 species is roughly the same at all CO_2 values, however, it does vary with melt composition (Zhang et al. 2007). In strongly rhyolitic melts, CO_2 is present as mCO_2 and in basalts it is present as CO_3^{2-}, with more intermediate compositions expected to have both present in varying concentrations (Zhang et al. 2007). The solubility of CO_2 varies with pressure and the alkalinity

of the magma, and increases with pressure. Therefore, magma that originates at depth, and thus high pressure, tends to have high CO_2/H_2O ratios compared to those originating shallower in the crust (Lowenstern 2001).

3.3.5 Sulphur

S is the third most abundant volatile in magmatic systems, so can have important impacts on melt behaviour. The behaviour of S in the melt is complicated because it is impacted by many factors such as temperature, pressure, magma mixing, degassing dynamics and interactions with crustal rocks and fluid (Giggenbach 1987). It is also complex due to the multiple valencies of S and the multiple species. The key species in magma are S^{2-} and SO_4^{2-} in the melt as well as H_2S and SO_2 in the gaseous phase (Baker & Moretti 2011). Dissolved S impacts the partitioning of metals into the sulphide phase and vapour phases and when this is released into the atmosphere is converted to sulphuric acid (H_2S), which has a negative impact on the atmosphere (Wallace & Edmonds 2011).

3.3.6 Chlorine

Cl behaves relatively simply during degassing processes because it has a low mineral/melt partition coefficient and high H_2O vapour-melt partition coefficient. In highly differentiated melts, experimental data shows that Cl is highly soluble and the behaviour is predominately controlled by H_2O degassing (Balcone-Boissard et al. 2010). Cl in volcanic systems is most often present as HCl, but at high pressures can also be present in chloride salts such as NaCl and KCl (Balcone-Boissard et al. 2010 and references therein). The solubility of Cl demonstrates a weakly inverse relationship with pressure, meaning that magma ascent is not the only controlling factor of Cl degassing (Metrich and Rutherford 1992). It partitions very strongly into aqueous phases thus is often exsolved into the degassing H_2O. In areas with strong hydrothermal circulation, as is expected within the Krafla geothermal field, the Cl can partition into the hydrothermal fluids and be removed from the system in that way (Schipper et al. 2019). Cl partitions into the fluid phase earlier than F, which becomes increasingly important as the melt becomes more evolved (Westrich et al. 1988).

3.3.7 Fluorine

F is the most poorly understood volatile. At low pressures F can be found in concentrations up to weight percent levels in high silica melts, and has a very low vapour-melt partition coefficient (Webster 1990). This suggests that F should not be affected by decompression and

should not degas into the atmosphere in any significant quantity (Balcone-Boissard et al. 2010). However, there is direct evidence of measured HF in many volcanic plumes (Aiuppa et al. 2009) and the hazardous manner of F in ash deposits is well known (Stewart et al. 2016). F is fractionated from the other halogens during degassing processes more readily because it has a greater solubility in silica rich magmas, thus tends to remain in the magma (Carroll 1994).The problem with studying F degassing comes from its tendency to adsorb onto surfaces forming salts that are readily dissolved into the aqueous phase present in the melt (Wardell et al. 2008).

3.4 Bubble growth

If the melt is oversaturated in volatiles, nucleation and growth of bubbles is promoted which in turn leads to the expansion of the magma body itself and eventual eruption of a highly vesicular magma. Oversaturation of volatiles in these melts can occur either because of a change in pressure or temperature such as during ascent, or because of addition of volatiles to the melt (Zhang et al. 2007). Bubbles nucleate in two ways; homogenously and heterogeneously. Homogeneous nucleation is the formation of a bubble in a melt that is both crystal and bubble free, so the bubble is the first thing to form in that specific magma. The pressure required for oversaturation to be significant enough for homogenous nucleation to occur is often higher than 100 MPa in rhyolitic magma (Mangan & Sisson 2000). Heterogeneous nucleation occurs in a magma that contains other phases, such as crystals or inclusions. This process is the more efficient of the two mechanisms and requires pressures as low as 5 MPa (Shea 2017).

The type of nucleation occurring in magma is impacted by the chemistry of the magma, with nucleation in crystal-poor rhyolite favouring homogeneous nucleation, while less evolved, less viscous magma favours heterogeneous nucleation (Shea 2017). The size of the bubbles in magma is also impacted by magma chemistry, with rhyolitic magmas typically producing smaller bubbles than those in magmas of basaltic composition. The smaller bubbles in rhyolites is attributed to the lower diffusivity of H_2O in silica-rich melts (Sparks 1978).

3.5 Quenching

Because of the manner in which the KJ-39 sample was retrieved, it is important to address the effect of quenching on the magma.

3.5.1 Impact on magma chemistry

Major element chemistry of magmas is impacted by quenching because quenching rapidly halts crystallisation processes that would usually occur when the magma cools slowly. This means that the glass chemistry represents that of the time of quenching, rather than what the magma would have evolved to if it was to erupt or cool.

3.5.2 Impact on volatiles

Studies by Silver & Stolper (1989) and Stolper (1989) show that the H_2O speciation of melt is impacted by quenching in magmas over 1000 K (726 °C). In the initial stages of the quenching process the conversion of mH_2O to OH and vice versa, keeps up with the cooling of the magma. As the magma continues to cool, the conversion rate slows and eventually stops, because there is no longer enough thermal energy to convert the mH_2O to OH (Silver & Stolper 1989, Stolper 1989, Silver et al. 1990). Therefore, the final speciation of the glass actually represents the temperature at which the conversion between species stops, rather than the temperature at which the magma was quenched. If the quenching rate is high, then the difference between these temperatures will be negligible. Because of this, volcanic glasses that have been quenched will have higher mH_2O/OH ratios at higher temperatures (Zhang & Ni 2010).

3.6 Degassing

Degassing processes are important to consider because they can contribute to the eruption of magma, however, in the case of both KJ-39 and IDDP-1 magmas, they were intercepted by drilling and thus, degassing processes were halted. However, non-eruptive degassing is a common process, particularly in silicic and intermediate magmas worldwide (Boichu et al. 2008), such as Vulcano Island in Italy (Nuccio & Paonita 2001) and White Island in New Zealand (Giggenbach & Sheppard 1989). This degassing is often observed in two phases; short-duration gas exsolution periods, followed by long-term secular degassing. Boichu et al. (2008) suggested that this non-eruptive degassing could be attributed to degassing of a shallow intrusion that has halted in the crust and begun to cool. As the magma cools it crystallises and causes the volatiles in the remaining melt to become oversaturated, increasing the pressure of the intrusive body. At shallow depths the overpressure causes cracks to propagate to the surface and allows gas to escape. Following gas escape the intrusion returns to its original pressure and the cycle begins again (Boichu et al. 2008).

3.7 Summary

Magmatic processes and the presence of volatiles are key factors in the end composition of the magma. Processes such as fractional crystallisation and melting impact the major element content and provide important insight into the evolution of the magma. Volatiles, particularly H_2O can also greatly impact the behaviour of the melt and have a huge impact on other magmatic processes. These processes are important to note when investigating the origin of the KJ-39 magma and how this magma body fits within the wider Krafla region.

4 Analytical Methods

4.1 Introduction

This chapter describes the main analytical methods that were utilized as part of this study and will overview sample preparation, analysis and data processing for each method. The primary analytical methods that were used are electron probe microanalysis (EPMA) to analyse the concentration of major elements, S, Cl and F of the glass and minerals and Fourier-transform infrared spectroscopy (FTIR) to analyse the H_2O and CO_2 content of the glass.

4.2 Sample preparation

The KJ-39 sample set was received as a collection of glass and crystals that, other than being washed to remove drilling mud, remained unchanged from the state in which they were retrieved at the surface of the well. Initially, samples were sieved using the 500 μm mesh, followed by the 355 μm mesh in order to separate the largest samples. These sizes were chosen because they allowed a large portion of the sample to be used, while keeping the glass shards large enough for sample preparation to be manageable. The glass was separated from the pyroxene and plagioclase phenocrysts that were also present in the KJ-39 sample. The glass samples were then separated into three groups; for EPMA, FTIR and a spare group. Because of time constraints of the project, samples were analysed in two groups; the first were analysed for major elements and then volatiles (Group 1) and the second were analysed for volatiles then major elements (Group 2) (*Fig 4.1*).

4.2.1 Group 1; EPMA then FTIR

Firstly, the samples were organised into groups to mount. Mounts 1 to 4 each contained two of each crystal (plagioclase and pyroxene) and two glass chips, and the remaining two mounts (Mounts 5 and 6) contain nine and eight glass chips respectively. The chips were secured on a clean glass plate using double sided tape, over which a 2.5 cm mould was placed. Epoxy resin (EPO-TEK® 301) was poured over the chips to a thickness of 0.75 cm and left to set overnight. Once set, the mounts were removed from the moulds and the tape removed. The mounts were ground to expose the largest possible area on each of the glass chips and crystals using silica carbide paper, starting with a grade of P180 and working up to P2000, then polished using 3 μm and finally 1 μm diamond paste on a polishing disc to remove any scratches on the surface.

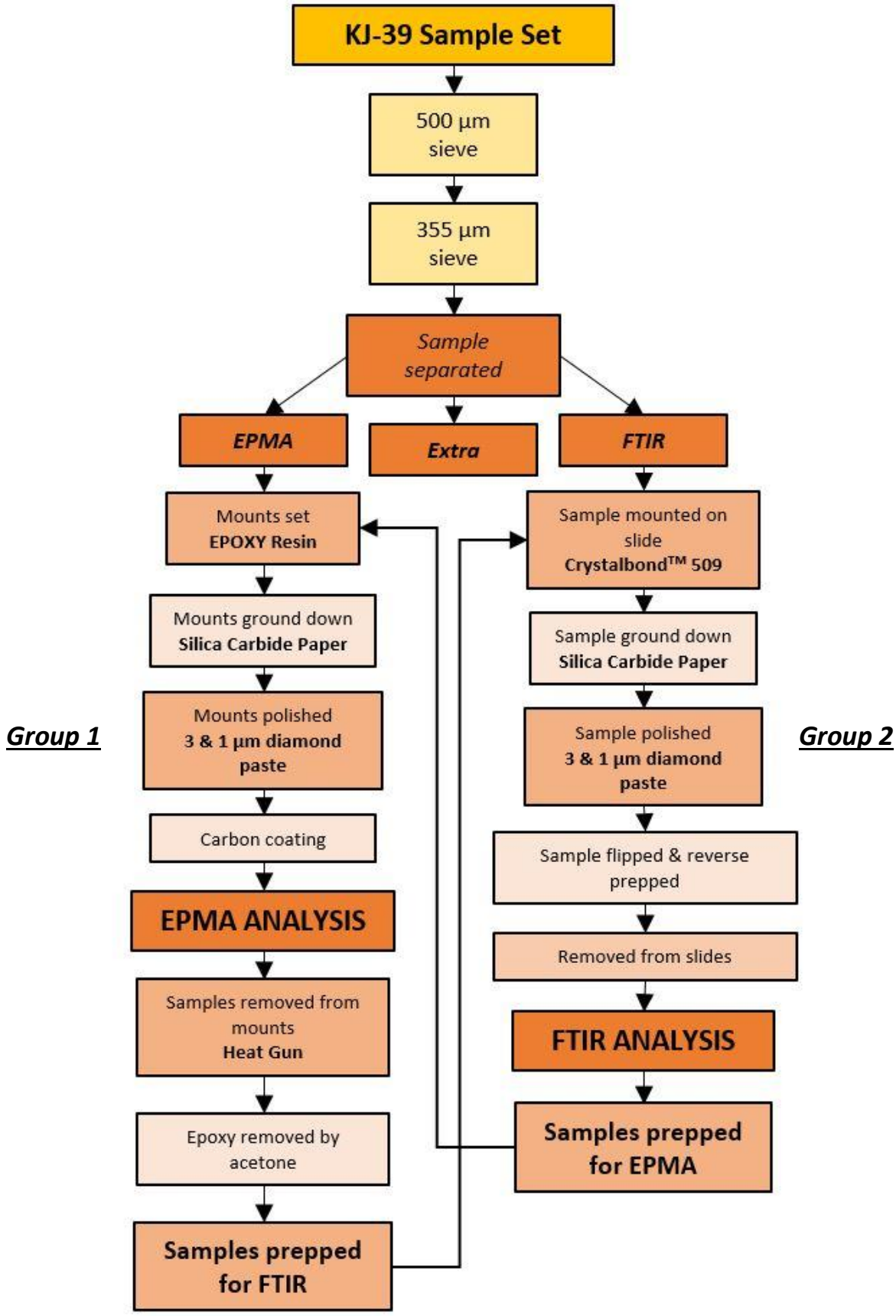

***Fig 4.1**: Flow chart outlining the preparation process for samples in Group 1 and Group 2. Arrows from the bottom show the second round of preparation based on the order of analysis.*

Before being placed in the electron microprobe, the samples needed to be carbon coated to prevent them charging. The samples are non-conductive so the carbon coat allows them to conduct x-rays without impacting the x-ray spectrum (Reed 2005). The carbon is coated on the sample mounts in a vacuum chamber, with a carbon evaporation source that consists of pointed carbon rods. A current of 100 A is passed through the rods, causing the carbon to evaporate from the rods and onto the sample.

After the samples had been analysed for major elements by EPMA, the samples had to be removed from the epoxy mounts so that they could be prepared for FTIR analysis. The mounts were targeted with a heat gun at a temperature of 350 °C. The heat caused the surface of the mounts to crack and therefore the samples could be picked out with tweezers. The samples were placed in acetone for 24 hours in order to dissolve any remaining epoxy still on the samples, then removed and left to dry on clean tissue. Because only the glass samples were analysed for volatiles, the crystals were left in the epoxy mounts.

For FTIR analysis samples must be free-standing doubly polished wafers (free of any adhesive or epoxy, which would contaminate the spectra) of a known thickness. A glass slide, with the thermo-adhesive Crystalbond™ 509 on it, was placed on a hot plate set at a temperature of 90 °C to melt the adhesive, then the sample was placed, polished side down on the slide. Crystalbond™ was chosen because of its low melting temperature (120 °C) and its solubility in acetone, thus making it relatively easy to remove the sample. The samples were ground and polished following the same process used for the EPMA mounts and during this polishing process, the thickness of the samples was frequently checked using a digital indicator micrometer, to ensure that the sample was prepared to the appropriate thickness for analysis (described below in section *4.4.3*). The samples were then flipped by remelting the Crystalbond™ on the heat plate and polished using 1 μm diamond paste to remove any remaining carbon from the carbon coating used during electron probe analysis. When samples were sufficiently thinned and polished, the Crystalbond™ was remelted so that the sample could be removed and placed in acetone. When all of the Crystalbond™ was dissolved the sample was removed and left to dry on clean tissue.

4.2.2 Group 2; FTIR then EPMA

Samples that were separated for initial FTIR analysis were mounted on a glass slide using Crystalbond™ and ground down to a thickness of approximately 60-100 μm, by the same

process as described in section *4.2.1* (thickness monitored throughout the process using a digital indicator micrometer). The samples were then polished using 3 and 1 μm diamond paste on a polishing disc until the sample was scratch free. The polish was checked using a reflected light microscope. The glass slide with the sample on was then placed on the hot plate to melt the adhesive so the sample could be flipped using tweezers. The second side of the sample was ground and polished as above, monitoring the thickness throughout, until the sample was at a sufficient thickness for analysis.

When the samples had been analysed for volatile contents, the samples were prepared for EPMA analysis. All of the Group 2 samples were secured on a clean glass plate using double sided tape, and a 2.5 cm mould was placed over the top. Epoxy resin was poured over the samples and left to set overnight. When the mount was set and the mould removed, they were polished as above so that the chips were exposed and scratch free. The samples were already flat from the FTIR analysis so only required polishing. Finally, before the samples could be analysed by the electron microprobe, they were carbon coated as above.

As well as the glass chips that were analysed in the second round of EPMA analysis, a group of glass with crystals attached were also analysed. These samples were prepared in an epoxy mount as above, and ground and polished so that the samples were scratch free.

4.3 Electron probe microanalysis (EPMA)

Electron probe microanalysis (EPMA) is a commonly used technique to identify the major element composition of a solid sample. The sample is bombarded by a focused beam of electrons causing the release of X-rays as the beam interacts with the different elements. This creates an X-ray spectrum that is then used to interpret the elements present. The intensities of the resulting lines are compared with those of standard samples that represent pure elements or samples with known concentrations (Reed 1995) and provide concentrations as wt%. Glass chips, minerals and opaques were analysed by EPMA using the JEOL JXA-8230 Superprobe at the School of Geography, Environment and Earth Sciences at Victoria University of Wellington. Major element concentrations were measured using a voltage of 15 kV and a current of 8.0 nA. Peak and background count times were 30 s and 15 s, respectively and the beam diameter was defocused to 10 μm. In order to calibrate the glass results, both synthetic and natural standards were used as follows (*Section 5.3.1*); basaltic glass standards VGA-99

and IO and two rhyolite standards VG-568 and VG-2. To calibrate the crystals and opaques that were measured, synthetic pure oxides of Ti, Mn and Cr were used as well as K-pyroxene, plagioclase feldspar, and Elba pyrite standards (*Appendix A*). Individual glass chips were analysed at least three times, with further analyses carried out on any phenocrysts (in the second round of EPMA analysis) and opaques that were present. The standards for glass or crystals were measured twice after every 20 measurements on the samples, dependant on what was being analysed.

The first round of analyses measured 25 glass chips as well as 16 crystals for major elements and the volatiles, S, Cl and F. The crystals were analysed at least three times per crystal, and where zoning was identified a measurement on each zone was carried out. Of the 25 glass chips, 6 were highly vesicular while the rest had less than 5% bubbles. These chips were chosen in order to identify whether there are any differences in composition in samples that have different textures. A second set of glass chips, consisting of 18 samples, previously measured by FTIR were later probed to get a full set of major and volatile components, as well as data from a set of opaque minerals that were identified. During this second round of EPMA analysis a separate group of glass samples with phenocrysts of plagioclase or pyroxene were analysed in order to determine the relationship between the glass and crystals.

4.3.1 Electron dispersive x-ray spectroscopy (EDS)

As well as providing quantitative measurements, the electron probe can be used to determine the qualitative composition of samples using electron dispersive x-ray spectroscopy (EDS). This analytical technique can be used to identify all elements of the periodic table, with the exception of H, He and Li (Newbury & Ritchie 2013) and is useful because it provides quick identification of elements based on x-ray peaks from excitation of electrons, as with the EPMA. This technique was used to determine the composition of opaques in the glass samples.

4.4 Fourier-transform infrared spectroscopy (FTIR)

4.4.1 Principles of FTIR

FTIR was carried out on the glass chips in order to determine the original magmatic H_2O and CO_2 content of the magma that was intersected by the KJ-39 drilling. In FTIR, infrared radiation is passed through a doubly polished sample of known thickness. The radiation

interacts with the molecular species of the volatiles by causing a change in the vibrations of the covalent bonds (Stolper 1982b). The change in vibration allows the molecules to absorb specific frequencies of radiation that correspond to the specific molecular frequency of the bond. Each of the bonds will absorb a different wavelength and produce an absorption peak that will appear at different wavenumbers on the IR spectrum (*Fig 4.2*).

FTIR is useful for determining volatile concentrations because it can detect a large range of concentrations of hydrogen and carbon phases, from a few parts per million to tens of weight percent. It can also determine the concentration of individual species, molecular H_2O (mH_2O) and OH, as well as total dissolved H_2O content (Newman et al. 1986). The technique is non-destructive and the small size of the IR beam (minimum 10 x 10 μm) means that it can be placed on the sample to avoid any crystals or vesicles that might affect the data. H_2O is especially receptive to analysis using FTIR because the bonds are highly polarised and thus are efficient absorbers of the IR radiation (Della Ventura et al. 2010).

4.4.2 Absorption bands

Absorption bands for H_2O are often split into two groups; the near-IR region, ranging from 14000-4000 cm^{-1} and the mid-IR region from 4000-400 cm^{-1} (*Fig 4.2*). In each of these regions there are absorption peaks caused by the vibrations of certain bonds within the molecule. In the near-IR region the two most common peaks are at 5200 and 4500 cm^{-1}, the first is associated with the bending and stretching of molecular H_2O (mH_2O) (Scholze 1960; Bartholemew et al. 1980), and the second a combination of the stretching of both Si-OH and Al-OH groups (Stolper 1982b). In the mid-IR region the 3550 cm^{-1} peak is a combination peak representing the H_2O_t content associated with the stretching of mH_2O and OH, while the peak at 1630 cm^{-1} is a symmetrical peak associated with the bending of mH_2O (Stolper 1982b).

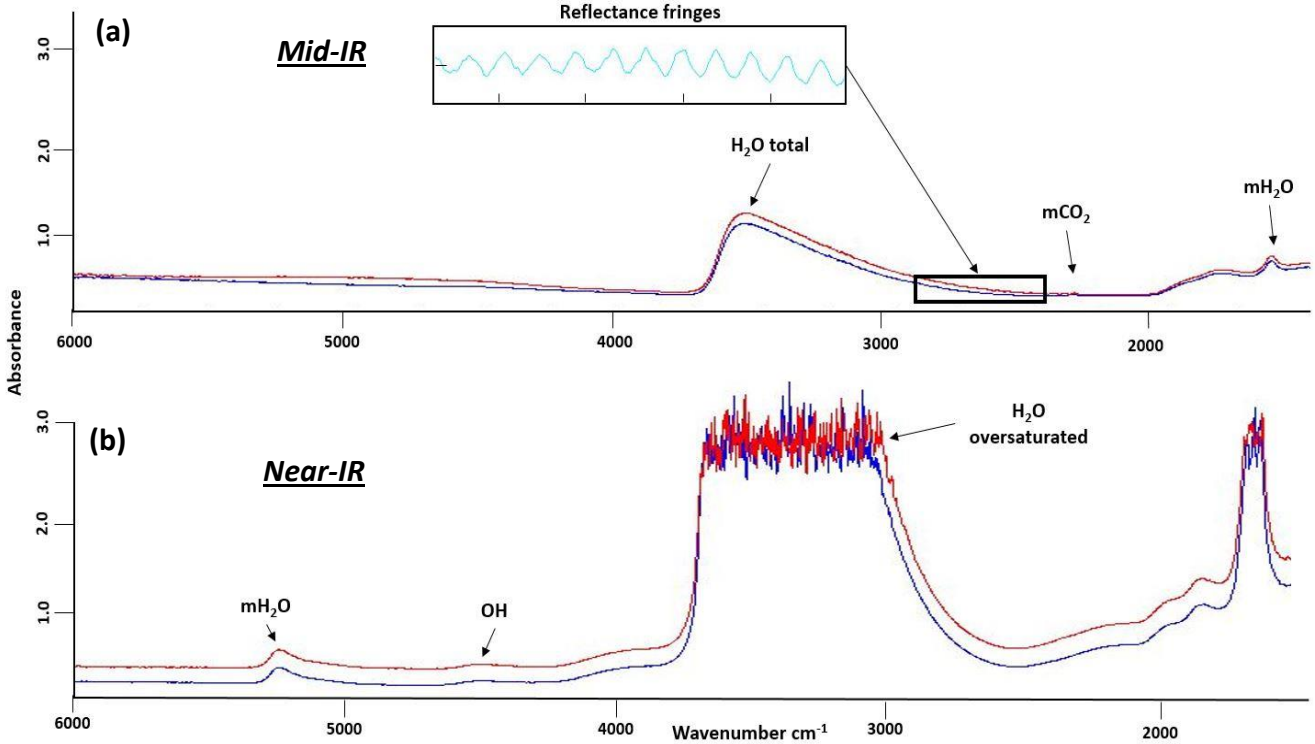

***Fig 4.2**: Example of FTIR spectra showing peaks of each species. (a) Mid-IR range showing H_2O_t, mH_2O and mCO_2 peaks at 3500, 1630 and 2350 cm^{-1}, respectively, and additionally reflectance fringes used to calculate thickness. (b) Near-IR range showing OH and mH_2O peaks, at 4500 and 5200 cm^{-1}, respectively, note the oversaturated peaks for H_2O_t at 3500 cm^{-1} and mH_2O at 1630 cm^{-1}.*

As well as H_2O, there are peaks that represent the different species of CO_2, including 2350 cm^{-1} associated with the stretching of molecular CO_2 (mCO_2) and a double peak at 1515 and 1435 cm^{-1} associated with the asymmetric stretching of CO_3^{2-} (*Fig 4.3*) (Newman et al. 1986; Stolper 1989). Unlike H_2O, the species of CO_2 present is a factor of melt composition rather than total CO_2 concentration, as discussed above in section *3.3.4*. If the mCO_2 peak at 2350 cm^{-1} is a doublet or is noisy, this indicates that the machine was not completely purged from atmospheric CO_2 or the presence of gaseous CO_2 in the beam path (Newman et al. 1986) (*Fig 4.3*). If there are no bubbles in the sample, it is likely that the gaseous CO_2 is present in the atmosphere in which the measurements were conducted, rather than in the sample itself. If the sample is kept under purge during the analysis by using a protective jacket around the sample, atmospheric CO_2 can be kept to a minimum. However, during the measurement of samples in this study, technical problems with the FTIR meant that the sample was at times open to the atmosphere.

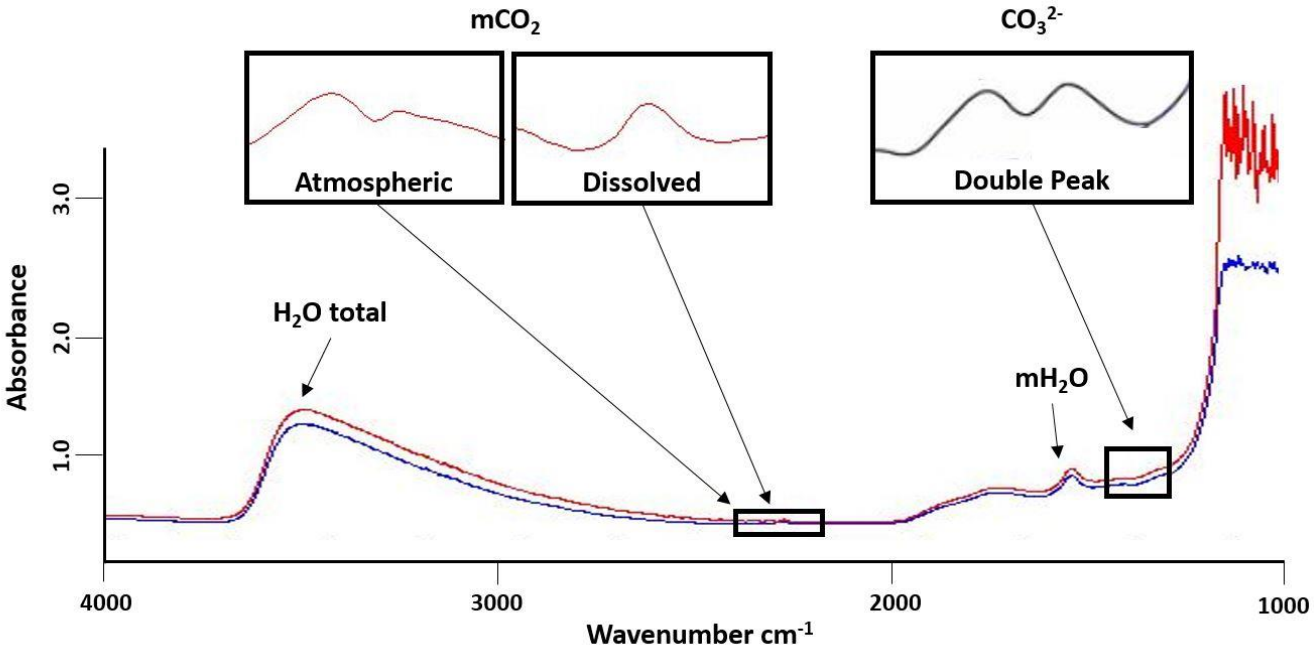

***Fig 4.3**: Example of FTIR spectra showing the representative peaks of CO_2 species. Molecular CO_2 is present at the 2350 cm^{-1} peak, but a double or noisy peak can represent gaseous CO_2. CO_3^{2-} is present as a double peak at 1515 and 1435 cm^{-1}.*

4.4.3 Measurement set up

FTIR analysis was conducted at the University of Canterbury on a Bruker Vertex 70 spectrometer to which a Bruker Hyperion 2000 microscope was attached. Single spot analyses were carried out using a conventional globar source, a potassium bromide (KBr) beamsplitter and a liquid nitrogen cooled mercury cadmium telluride (MCT) detector over a wavenumber range of 1000 to 6000. Apertures were set at 20 x 20 μm. At least 6 measurements were carried out on each sample, positioned randomly but ensuring the results are representative of the entire glass chip. Each sample was analysed in transmitted light to obtain absorbances of each species of interest (mH_2O, OH, CO_2) and reflected light in order to use the reflectance fringes to determine thickness (*Figs 4.2, 4.5*). In total, 44 samples were measured. In addition, a subset of nine samples were re-analysed at the Australian Synchrotron on their Bruker Vertex 70 spectrometer, to which a Bruker Hyperion 3000 infrared microscope with a focal plane array (FPA) detector was attached. The set up was the same as that used at the University of Canterbury, with the addition of the FPA detector (the spectrometer was not on the synchrotron beamline). The FPA detector allowed maps of 350 x 350 μm at a spatial resolution of 5.5 μm to be collected. These could be tiled to cover larger areas enabling more detailed analysis of the distribution of water to be measured across the entire chips.

4.4.4 Concentration calculations

In order to calculate the concentration (*c*) of individual H_2O and CO_2 species in the samples from the absorption values obtained from the FTIR, the Beer-Lambert Law must be utilised (Bouguer 1729, Ballentyne 1970):

[4.1]

$$c = \frac{M.A}{p.d.\varepsilon}\ x\ 100$$

Where *c* is the concentration of the species concerned (wt%), *M* is the molar mass of the molecule of the species of interest (i.e., H_2O or CO_2) ($g.mol^{-1}$), *A* is the absorbance of the species concerned (unitless), *p* is the density of the sample ($kg.m^{-3}$), *d* is sample thickness (cm) and ε is the molar absorptivity for the absorbance band concerned ($l.mol^{-1}.cm^{-1}$) (Newman et al. 1986).

4.4.4.1 Absorbance (A)

Each measurement in transmitted light produces an absorbance spectrum that includes the absorbances of the different volatile species at different wavenumbers, as demonstrated by the red and blue lines in *Fig 4.2* that represent different analysis points on the same sample. Using the Bruker software OPUS 7.8, the absorbance value (*A*) for each peak is extracted using the height of the peak above a linear baseline at a specified wavenumber. In the near-IR these are 4500 cm^{-1} for OH and 5200 cm^{-1} for mH_2O, and in the mid-IR these 3550 cm^{-1} for H_2O_t, 1630 cm^{-1} for mH_2O and 2350 cm^{-1} for mCO_2. The linear baseline is defined by a flat line connecting either end of the peak (as shown for the 3550 cm^{-1} peak for total H_2O_t in *Fig 4.4*, integration mode K in OPUS 7.8).

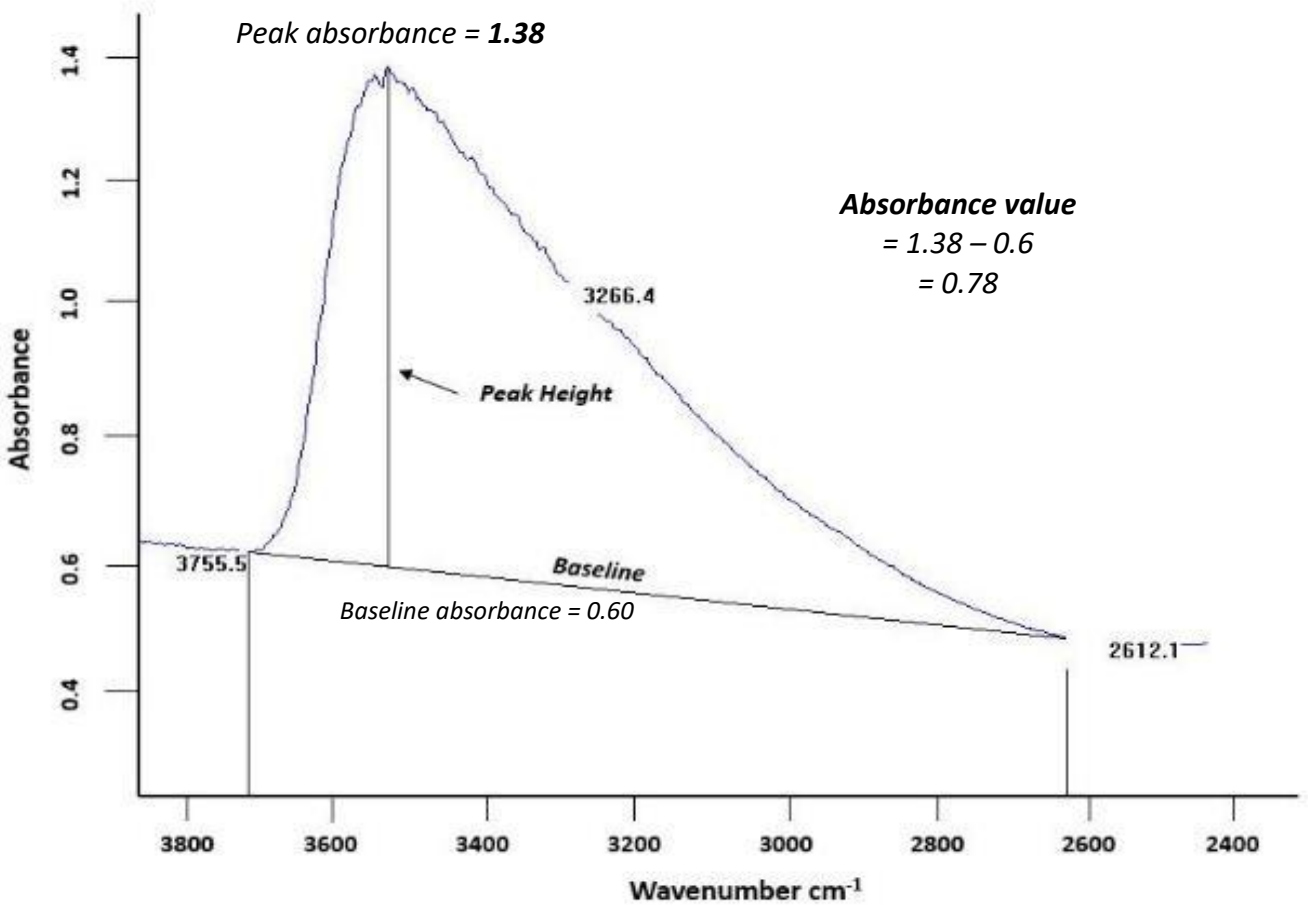

Fig 4.4: *Example of the integration method used in OPUS 7.8 to define the absorption value for individual points and species.*

4.4.4.2 Molar absorptivity coefficient (ε)

The molar absorptivity coefficient (ε) used varies depending on the species being calculated (Stolper 1982b, Newman et al. 1986) and the bulk composition of the glass. The molar absorptivity coefficient value for H_2O_t (3550 cm^{-1}) also depends on the amount of mH_2O and OH as this peak is a combination of the stretching of these two species (Newman et al. 1986, McIntosh et al. 2017) (*Equation 4.2*):

[4.2]

$$\varepsilon 3550 = X_{OH}\,\varepsilon 3500_{OH} + X_{mH2O}\varepsilon 3500_{mH2O}$$

Where X_{OH} and X_{mH2O} are the mass fractions of water dissolved as OH and mH_2O respectively. However, this equation requires the speciation of the sample to be known prior. McIntosh et al. (2017) rewrote *Equation 4.2* in terms of species concentrations (*Equation 4.3*) where $X_{OH} = C_{OH}/C_{H2Ot}$ and $X_{mH2O} = C_{mH2O}/C_{H2Ot}$;

[4.3]

$$\varepsilon 3550 = \frac{C_{OH}\varepsilon 3500_{OH} + C_{mH2O}\varepsilon 3500_{mH2O}}{C_{H2Ot}}$$

Then rearranged for CH_2O_t and substituted into the Beer-Lambert Law (*Equation 4.1*) to provide an expression in terms of the concentration of OH;

[4.4]

$$C_{OH} = \frac{1}{\varepsilon 3500_{OH}} \left(\frac{100 MA_{3550}}{p} - \varepsilon 3500_{mH2O} C_{mH2O} \right)$$

Where A_{3550} is the absorbance (peak height) at 3550 cm^{-1} normalised for the sample thickness. This equation allows the OH concentration of a sample to be calculated directly, providing that the thickness, absorbance, mH_2O concentration and end member ε values for the glass composition (described below) are known. Finally H_2O_t to be calculated simply as;

[4.5]

$$C_{H2Ot} = C_{mH2O} + C_{OH}$$

Because the EPMA analysis indicated a wide range of SiO_2 values the ε3500 end members for Fe-bearing andesite of 79 ± 11 $l.mol^{-1}.cm^{-1}$ for OH, and 49 ± 6 $l.mol^{-1}.cm^{-1}$ for mH_2O developed by McIntosh et al. (2017) were used along with the rhyolite end member values from Newman et al. (1986) 100 $l.mol^{-1}.cm^{-1}$ for OH, and 56 $l.mol^{-1}.cm^{-1}$ for mH_2O, depending on the composition of the sample. However, some of the KJ-39 glass chips were dacitic in composition (SiO_2 content 63-75 wt%) for which no end member ε values have been determined. Therefore, samples that had SiO_2 contents <68 wt% were calculated using the Fe-bearing andesite molar absorptivity coefficient end members from McIntosh et al (2017) and those with SiO_2 >68 wt% were calculated with molar absorptivity coefficient end member values for rhyolite from Newman et al. (1986).

The molar absorptivity coefficient values for the 4500 OH and 5200 mH_2O peaks in the near-IR region also differed based on the SiO_2 content of the individual samples. For samples with SiO_2 content >68 wt% a ε4500 value of 1.73 $l.mol^{-1}.cm^{-1}$ and ε5200 value of 1.61 $l.mol^{-1}.cm^{-1}$ were used, from Newman et al. (1986). For samples with more intermediate compositions (SiO_2 content <68 wt%) a ε4500 value of 0.79 $l.mol^{-1}.cm^{-1}$ and ε5200 value of 1.07 $l.mol^{-1}.cm^{-1}$ were used, from Mandeville et al. (2002).

4.4.4.3 Density (ρ)

Density values for each individual point were calculated from the oxide data measured by EPMA using the principles, partial molar volumes and volume changes with temperature from Lange & Carmichael (1990) and Lange (1997), including those for H_2O from Ochs and Lange (1999). An average density of 2543 g/L was used for any samples that did not have major element data. This however, only applied to one sample (Chip 7).

4.4.4.4 Molar mass (M)

(*M*) is the molar mass of the species that is being calculated; 18.02 for OH and mH_2O and 44.01 CO_2.

4.4.4.5 Thickness (d)

Thickness measurements were primarily measured using a digital indicator micrometer before and after the samples were measured. Although this method is the quickest and easiest method and has an accuracy of 1 μm, there is a degree of uncertainty with the exact location of each sample point. The needle of the micrometer is larger than the area measured by the beam and it is difficult to place the needle in exactly the same location as the FTIR analysis because it is being positioned by eye.

Another method of obtaining the thickness of the sample is to use the interference fringes from the reflectance data (*Fig 4.5*). These interference fringes appear on many of the samples, but are particularly clear in the reflected light spectra of the thinner samples. Nishikida et al. (1996) showed that these fringes are directly related to the thickness and the refractive index of the sample (*Equation 4.6*).

[4.6]

$$t = \frac{m}{2n\ (v1 - v2)}$$

where *t* is the thickness of the area measured (cm), *m* is the number of interference fringes between wavenumbers $v1$ and $v2$ and *n* is the refractive index of the glass (*Fig 4.5*). For this study a refractive index of 1.5 (Friedman & Long 1976) was used for samples that classified as rhyolite, 1.55 for dacite and 1.58 for andesite (Vogel et al. 2017). Where interference fringes were present on the spectra, this method of calculation was preferred over the digital micrometer because the reflectance spectra were taken in exactly the same spot as the spectra

in the transmitted light. In this study the two methods yielded very similar results, with maximum discrepancies being 7 μm.

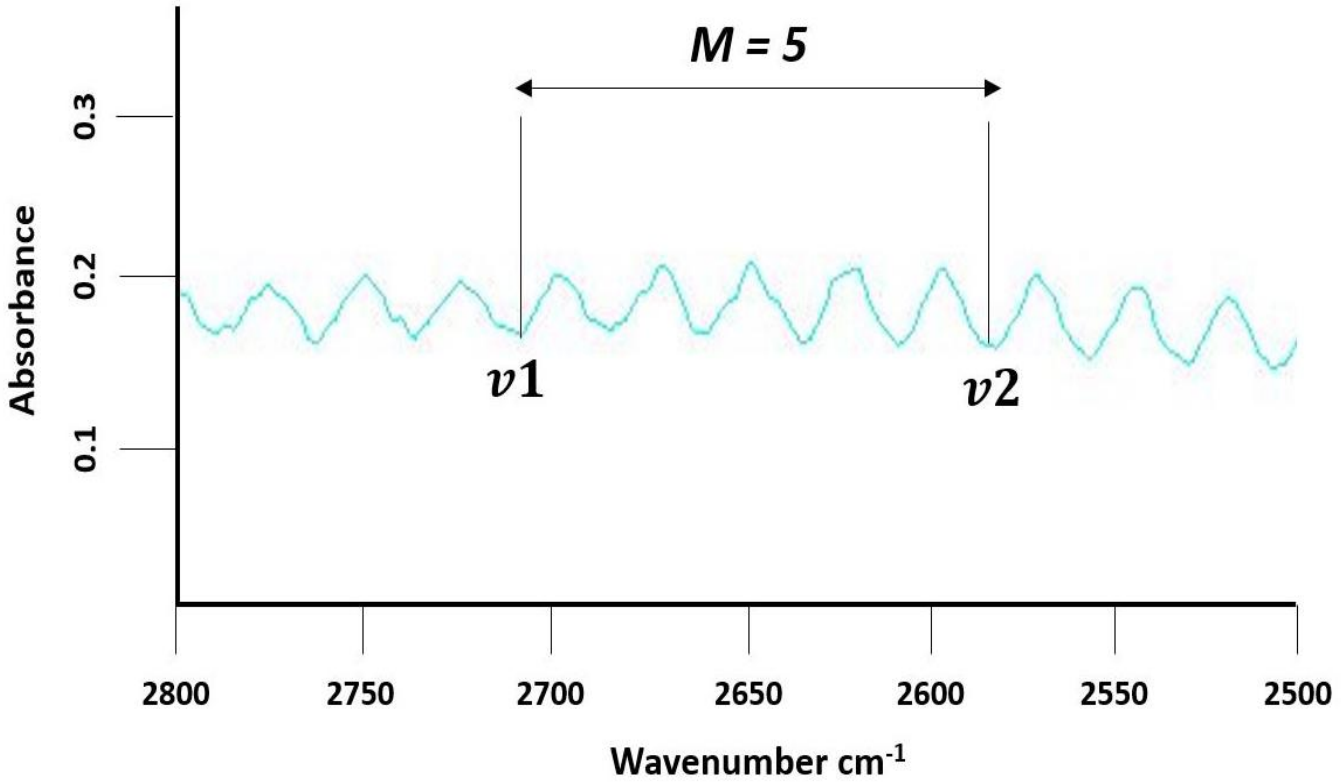

Fig 4.5: *Example of the calculation of thickness using the fringes from reflectance spectrum on the FTIR.*

4.4.5 Sample measurement

Firstly, in order to detect the full vibrational wavelength of each relevant band it is important that the samples are thin enough to allow sufficient infrared radiation to reach the detector after passing through the sample.

To determine the minimum thickness of the samples required for the near-IR (4500 and 5200 cm^{-1}) measurements to ensure that the peaks of interest were detectable, an estimate of the water content was required prior to measurement. Water content had not been previously measured in the KJ-39 glass chips, so water content was estimated from the difference of the total concentration of major elements from 100 wt%. Results from Mortensen et al. (2010) show that the major element totals add up to between 92-95 wt%, indicating that water content may be as high as 5-8 wt%. The Beer-Lambert Law (*Equation 4.1*) was re-arranged to determine a target thickness (*d*):

[4.7]

$$d = \frac{M.A}{p.c.\varepsilon}\ x\ 100$$

Because the Mortensen et al. (2010) data suggests that the total water content of the sample set is approximately 5 wt%, using the speciation model of Stolper (1982b) at this total water content, concentrations of 2.6 wt% for mH_2O and 2.4 wt% for OH were used. *A* values of 0.05 were used because this is the minimum detectable absorbance for the peaks in any range. Molar absorption coefficient values (ε) were taken from Ihinger et al. (1994) for rhyolitic compositions because the Mortensen et al. (2010) suggested the samples were rhyolitic in composition. Thicknesses calculated for the near-IR peaks using *Equation 4.7* ranged from 60-100 μm, so samples were initially prepared to fall within this range, with variations dependant on the pre-existing size of the glass chip and whether it broke up further. Values and references used for the initial calculation of thickness are displayed in *Table 4.1*.

Although thicker samples will allow the less intense near-infrared mH_2O and OH peaks to be detected as well as CO_2 in the mid-IR, the radiation at the more intense mid-IR H_2O_t and mH_2O peaks may be completely absorbed by the sample, resulting in no radiation reaching the detector. In this case, the absorbance peak will appear cut off (*Fig 4.2*) and will not be proportional to concentration (von Aulock et al. 2014).

***Table 4.1**: Table outlining the values used to calculate thickness required for the samples and the sources that the values were obtained from.*

	mH_2O	**OH**	**CO_2**		**Source**
c	2.6	2.4	0.0085	**Speciation**	Stolper (1982b)
M	18.02	18.02	44.01		
A	0.05	0.05	0.05		
p	2350	2350	2350		Stevenson et al. 1994
ε	1.86	1.5	1214		Ihinger et al. 1994
cm	0.008	0.011	0.009		
μm	79	107	91	**Thickness**	

To detect the mid-IR peaks (3550 and 1630 cm^{-1}), which are more intense, the sample wafer used to detect the near-IR peaks and CO_2 must be thinned until the radiation is not completely absorbed by the sample at that wavenumber. This time a maximum target thickness was obtained using *Equation 4.7* and the actual concentrations measured in the sample using the near-IR peaks. Newman et al. (1986) calculated that the thickness of samples required to detect absorbances in the mid-IR region would need to be 10-20 times thinner than those used to detect near-IR absorbances so samples were thinned to between 15-55 μm, which was about the limit of the preparation process without breaking the samples. If possible, the samples were measured both in the near-IR and mid-IR ranges to get absorbances for the full range of species present in the samples and check the accuracy of the methods. The concentrations from OH and mH_2O peaks in the near-IR region should add up to the same concentration of the H_2O_t peak in the mid-IR region. Because of the high H_2O contents in some of the samples, it was not always possible to thin the samples sufficiently that the radiation was not completely absorbed at the mid-IR peaks.

4.5 Temperature estimation using geothermometers

Crystallisation temperatures can be calculated using mineral and mineral-melt thermometers. For this study I used the two-pyroxene thermometer developed by Purtika (2008) using the composition of augite with pigeonite lamellae and augite with ferrosillite lamellae. This method uses the temperature dependence of the partitioning between the two pyroxenes and the diffusivity of Ca to calculate the temperature of crystallisation (Davis & Boyd 1966).

4.6 Textural Analysis

The vesicularity of the glass chips was analysed using backscatter electron images (BSEI) taken on the EPMA. Images of each sample were taken, ensuring that the contrast and brightness of each image was suitable to allow for the different phases within the chip (glass, vesicles, crystals and sulphides) to be identifiable. Each of the images was processed using Adobe Photoshop and Image J to identify the relative percentages of glass, vesicles and crystals as well as sulphides *(Fig 4.6)*. The shape of vesicles was also analysed to determine whether there is any compositional difference between samples with elongated versus rounded bubbles.

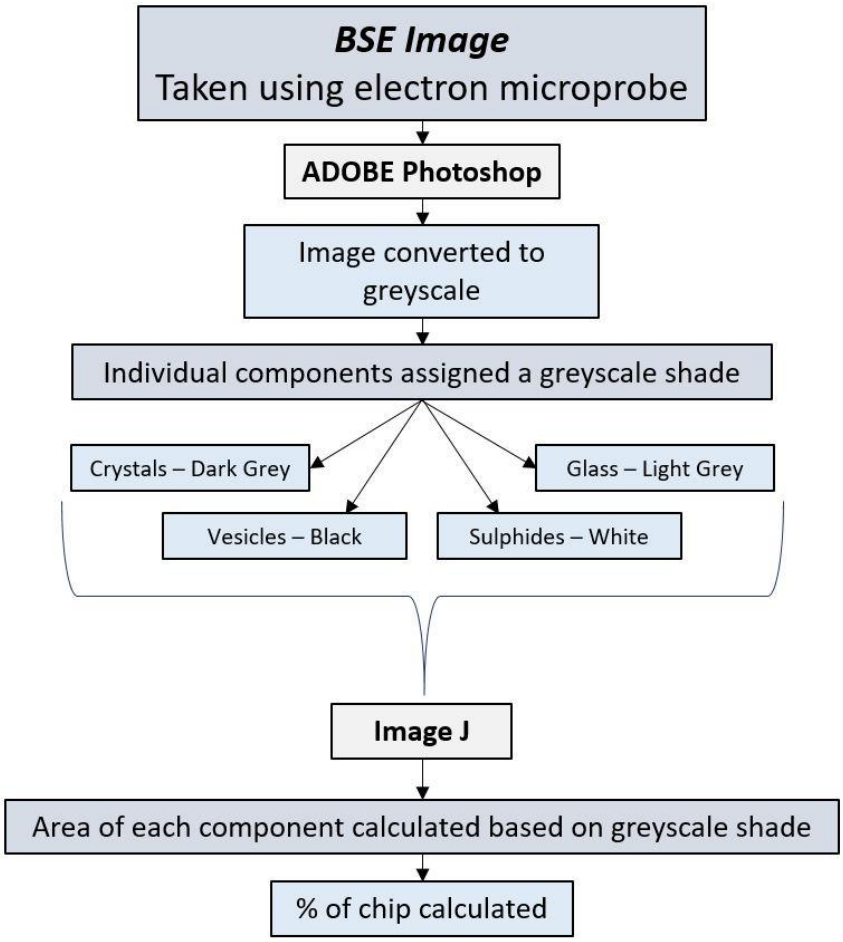

Fig 4.6: *Flow chart outlining the process used to calculate the percentage of vesicles, glass, minerals and sulphides (opaques) in the glass chips analysed for major elements. The images used are back scattered electron images (BSEI) taken using the electron probe.*

4.7 Summary

EPMA was used to measure the major element, Cl, F and S concentrations and FTIR was used to measure H_2O and CO_2 concentrations in the KJ-39 glass chips. BSEI were also collected using the electron probe and processed using Adobe Photoshop and Image J to enable the relative percentages of glass, vesicles and crystals to be calculated, and also investigate vesicle shape in each chip.

5 Petrography and Geochemistry of KJ-39 Cuttings

5.1 Introduction

This chapter will present the results from the textural and geochemical analysis of the KJ-39 glass chips. I will also address the phenocryst assemblage that was present alongside the glass and the opaques that were found in the glass. The implications of these data will be discussed in Chapter 6 in order to determine the origin of the KJ-39 melt.

5.2 Textural Analysis

The KJ-39 sample consists of a collection of glass and crystal chips (*Fig 5.1*). The crystals have been identified as pyroxene and plagioclase feldspar by EPMA analysis; there are also opaques in the glass, some of which infill vesicles.

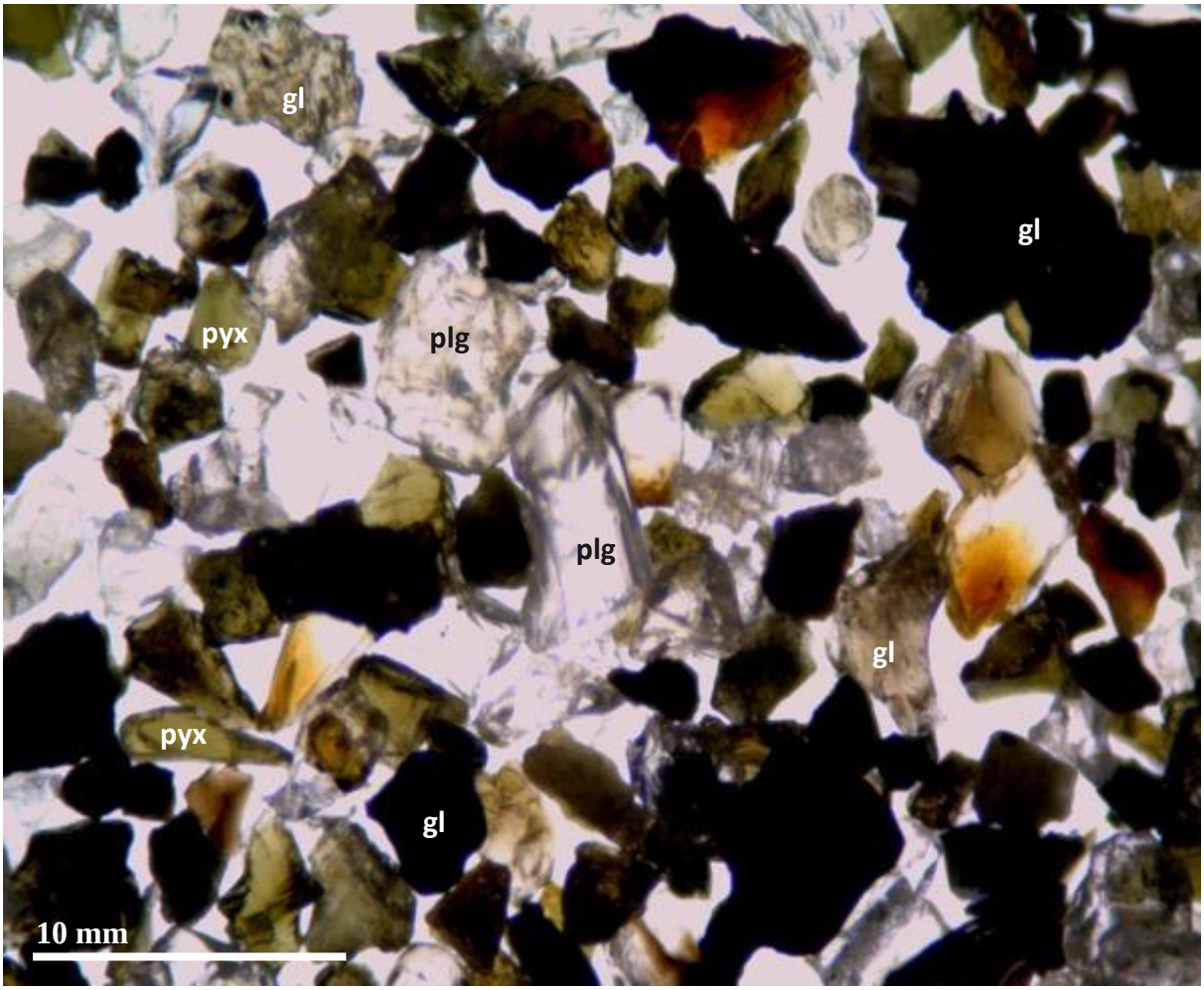

Fig 5.1: *Representative image of KJ-39, including glass and minerals. Pyx = pyroxene (augite), plg = plagioclase, gl = glass.*

Glass chips from the KJ-39 sample were analysed to determine the percentage of vesicles, crystals and opaques so that any relationship between the texture and the geochemistry of the glass could be identified. All of the glass chips selected were brown in colour, with the shade ranging from dark to light *(Fig 5.2)*. However, because of the differences in size and shape of the glass chips, the variations in colour are likely related to differences in thickness and/or vesicularity, with thicker chips looking darker, and thinner chips looking lighter. This was confirmed when chips were thinned for FTIR analysis and at similar thickness all appeared very similar in colour. Because of this, all of the chips analysed are considered brown and thus no separation can be made based on colour alone (cf. Watson, 2018, Saubin et al., In Review, for the IDDP-1 cuttings which could be divided into brown and clear glass, see *Section 2.6.4*).

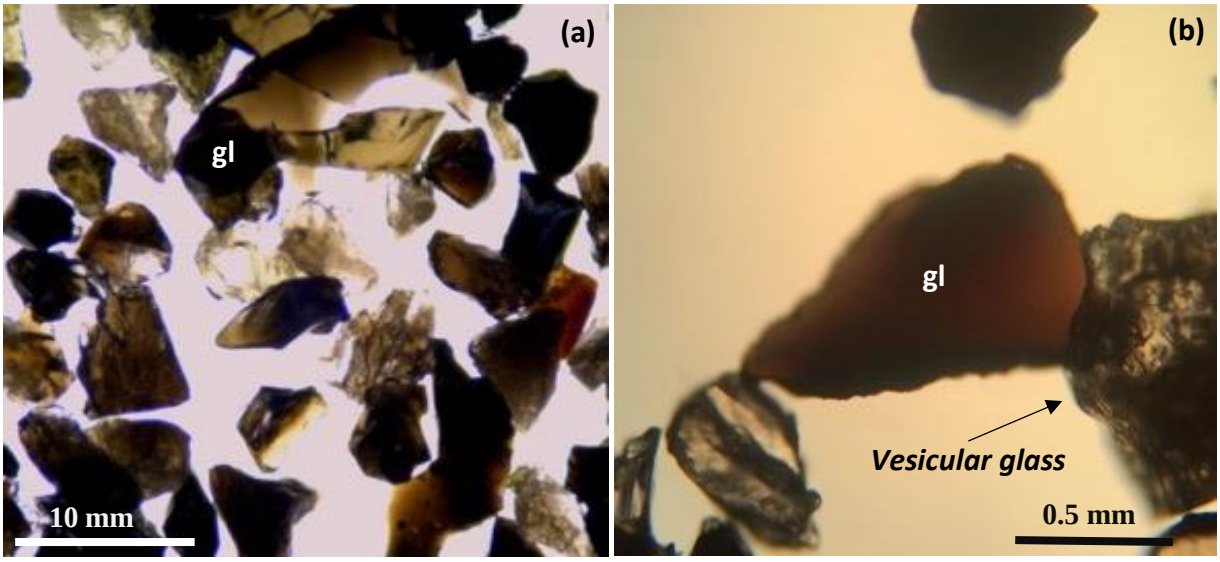

***Fig 5.2**: Images of the KJ-39 glass sample. (a) Glass chips showing the variation in colour and vesicularity. (b) Example of a non-vesicular glass chip. gl =glass.*

Glass chips containing crystals (plagioclase and/or pyroxene) were also selected from the entire sample to investigate the relationship between the glass and crystals. Owing to the fact that these chips were selected because they contain obvious crystals, and thus the crystal fraction is over-represented, these chips were removed from the textural analysis.

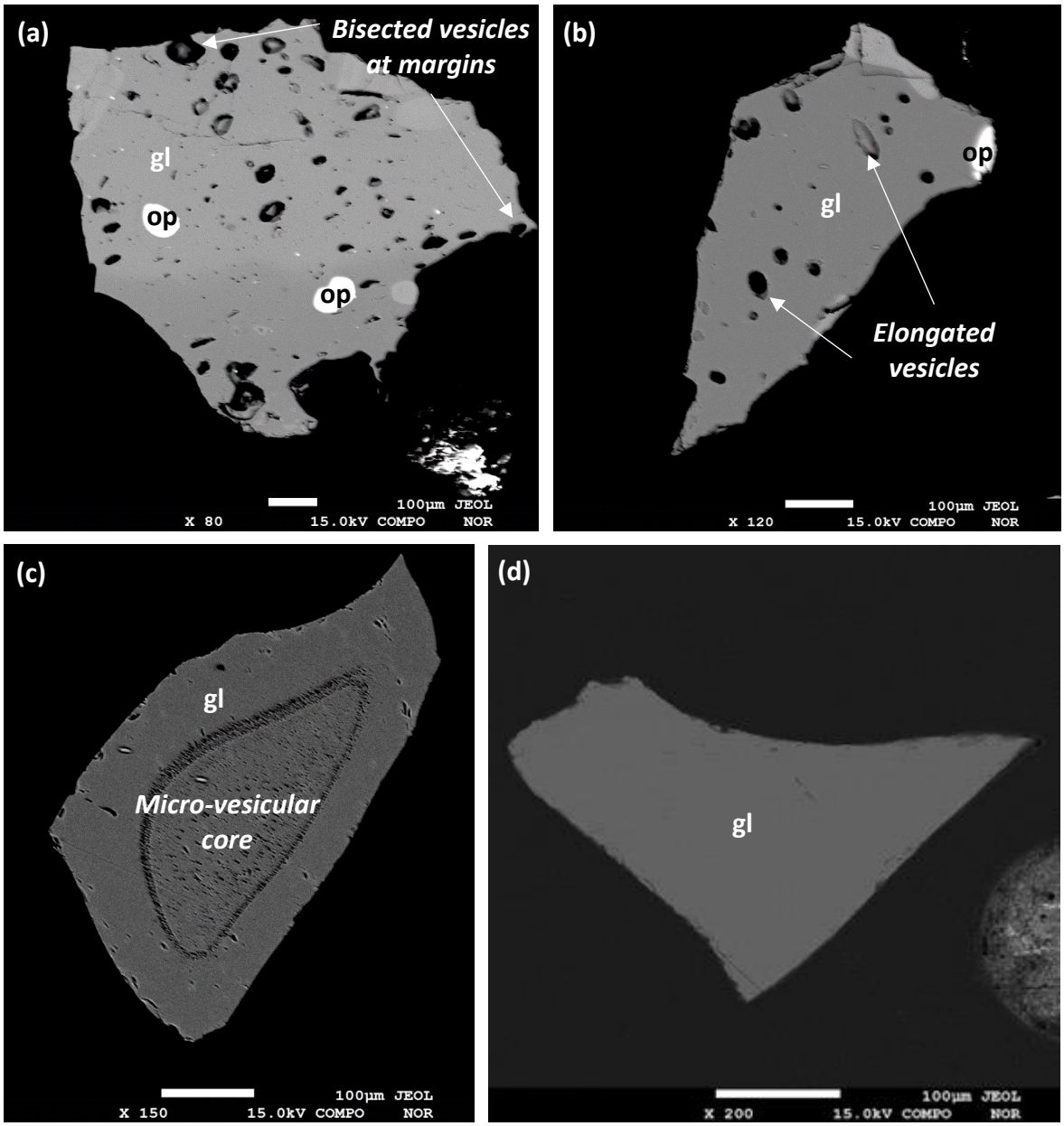

***Fig 5.3**: BSE images of glass chips showing different vesicle textures found in the KJ-39 sample set. (a) and (b) show vesicular glass chips. (c) shows a micro-vesicular core with less vesicular rim. (d) shows poorly vesicular chips: gl = glass, op = opaques.*

Chips range in texture from highly vesicular with crystals, to non-vesicular *(Fig 5.3)* and the percentage of vesicles ranges from 0.7 to 21.7%, with two chips showing no vesicularity (*Fig 5.3d*). For the purpose of this study, we classify chips with less than 5% vesicles as 'non-vesicular' and any with more than 5% as 'vesicular', which is consistent with the studies of Watson (2018) and Saubin et al. (In Review). Based on this system, five of the 46 chips analysed are 'vesicular' *(Fig 5.4)*. The vesicles range in shape, from spherical to elliptical, and size, with maximum length approximately 10 µm and maximum width approximately 5 µm.

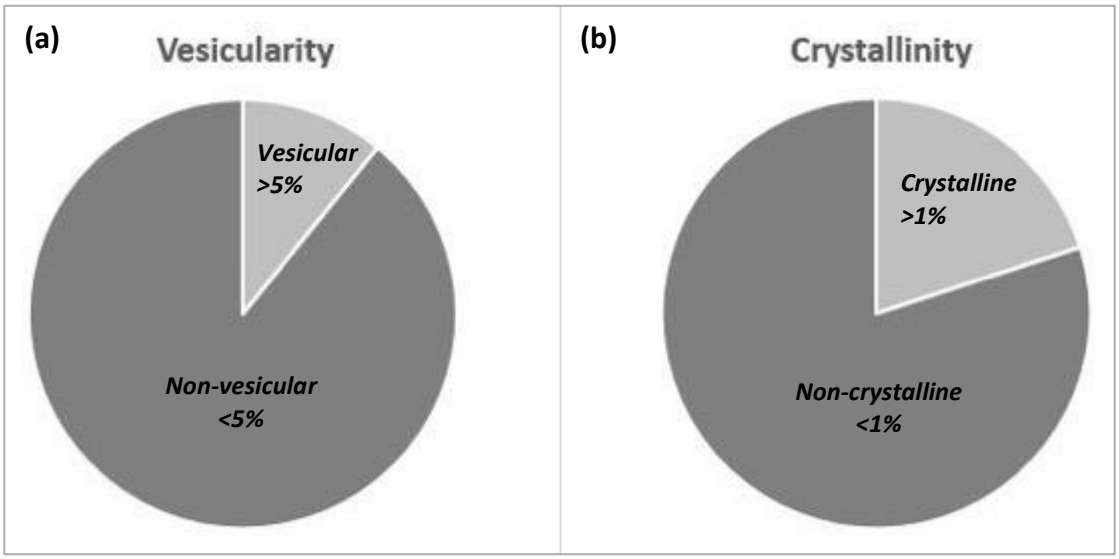

Fig 5.4: *(a) Percentage of samples that were vesicular vs. non vesicular and (b) crystalline vs non-crystalline based on image analysis from BSE images taken on the electron microprobe.*

The percentage of crystals ranges from 1.2 to 61.3% which is likely a factor of the size of the crystal, rather than the abundance. Because of this, any chips containing crystals are identified as ‘crystalline’.

5.3 Major Element Chemistry of Glass

5.3.1 Low totals

Major element data were measured on the EPMA and produced totals ranging from 85.14-99.62 wt%, despite the standards run during the measurements, having consistent totals close to 100 wt% (98.7-99.1 wt%) and closely reproducing their known compositions (*Table 5.1*).

Table 5.1*: Table outlining the standards measured using the electron probe and the published values. IO, from Jarosewich et al. (1980), VG2, VG568 and VGA99 from Jochum et al. (2005).*

	IO		**VG2**		**VG568**		**VGA99**	
	Measured	**Published**	**Measured**	**Published**	**Measured**	**Published**	**Measured**	**Published**
SiO_2	51.44	51.52	50.45	49.51	77.57	76.77	50.94	51.00
TiO_2	1.29	1.30	1.82	1.79	0.06	0.08	4.05	4.10
Al_2O_3	15.32	15.39	13.95	13.99	12.38	12.14	12.53	12.49
FeO	9.07	8.12	11.66	11.64	1.11	1.11	13.44	13.24
MnO	0.15	0.17	0.19	0.17	0.03	0.03	0.17	0.20
MgO	8.09	8.21	7.02	4.88	0.03	0.04	5.10	5.10
CaO	11.45	11.31	11.04	9.26	0.42	0.42	9.24	9.21
Na_2O	2.53	2.48	2.60	2.56	3.51	3.74	2.63	2.70
K_2O	0.07	0.09	0.19	0.12	5.80	4.97	0.82	0.86
Cr_2O_3	0.05	0.75	0.01	0.02	0.01	0.02	0.02	0.02
Total	**99.63**		**99.20**		**101.27**		**99.05**	

The quality of sample preparation could have an impact on the low totals produced by the analysis. Low totals may arise if the chip was not flat, not well polished or the analysis spot was poorly chosen. Most of the glass chips have similar totals for all analysis points across the surface of the chip, although there are some chips that have one analysis that has a significantly lower total than the other analyses for that chip. In this case, it is likely that the analysis was measured on a pit on the surface of the chip or partially measured another phase, which produced the low total and thus this analysis was removed from further consideration. *Fig 5.5* shows the surfaces of two chips, one that produced normal totals (chip 'c' – 98.5 wt%) and the other that produced low totals (chip 'g' – 90.7 wt%). Both chips show a well-polished surface suggesting that the difference in the totals was not due to poor sample preparation.

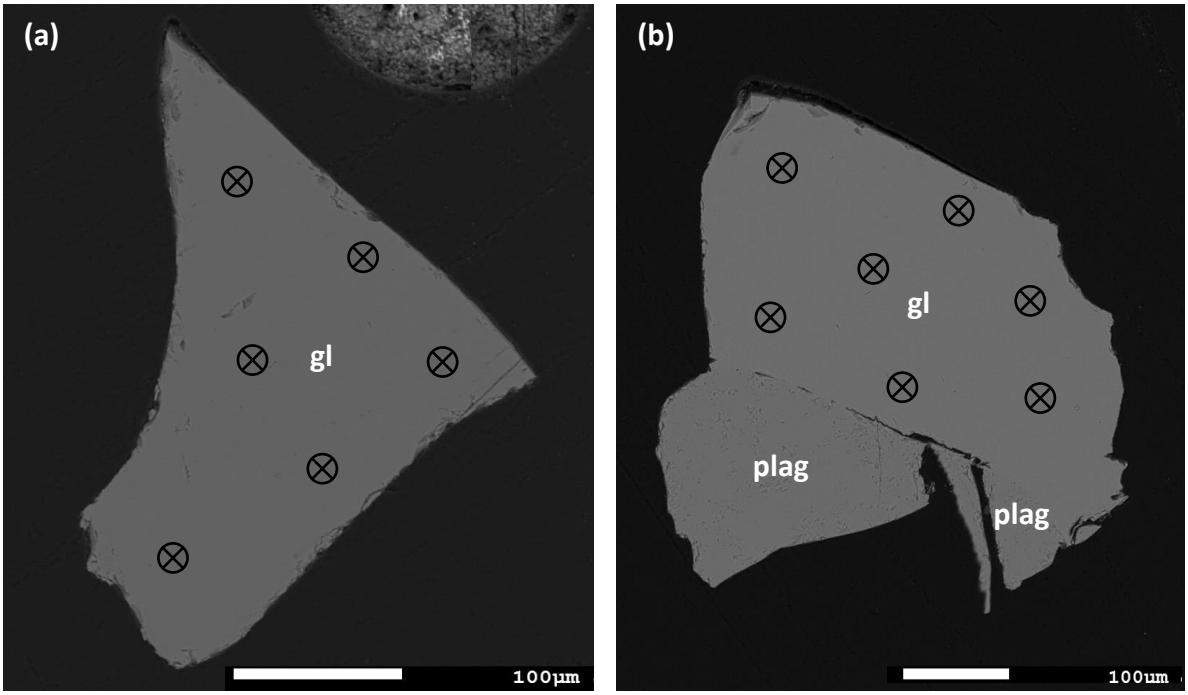

Fig 5.5: *BSE images of two glass chips showing analysis points (black crosses). (a) Chip 'c' which had normal totals (98.5 wt%) and (b) chip 'g' which had low totals (90.7 wt%).*

The measurements of the standards do not produce low totals, and the sample preparation is the same for chips with high and low totals (*Fig 5.5*), so it is unlikely that the reason for the low totals is an analytical issue. A previous study on the KJ-39 sample by Mortensen et al. (2010) also produced low totals, ranging from 92 to 95 wt% when the chips were analysed for major elements.

The chips with the lowest totals also show low Na_2O and Al_2O_3. When the totals are plotted against these oxides, there is a positive correlation (*Fig 5.6*) suggesting that the low totals may be related to Na_2O and Al_2O_3 loss during analysis. The Na_2O was measured first during the analysis, and for a shorter interval of time (10 s on peak/5 s on background) to minimise the possibility of Na volatilisation (e.g. Schipper et al. 2019). Further to this, the rhyolite standard VG568 contains 3.74 wt% Na_2O, similar to the highest value measured in the KJ-39 glass chips, and measurements on VG568 closely reproduced that value (3.51 wt%), indicating that these levels of Na_2O can be accurately measured. The KJ-39 glass with low totals thus may contain even higher Na_2O contents, and despite the measures already taken, Na_2O volatilisation still occurred. Based on the lowest totals Na_2O contents would need to be in excess of 5 wt% to make up the shortfall. Similarly, low totals and low Al_2O_3 suggest Al_2O_3 may also be being lost, despite no evidence of this occurring in the standard measurements. Na_2O and Al_2O_3 loss

would need to be confirmed by measuring a standard with even higher Na_2O and Al_2O_3 contents than those use here, and to examine whether measurement conditions could be refined further to minimise it.

Alternatively, or additionally, the low totals may reflect something in the glass was not included in the EPMA analysis. Volatiles Cl, F and S were measured so these are not missing, and H_2O and CO_2 contents measured by FTIR (*Section 5.4*) are not high enough to make up the missing totals. Other possible candidates are carbonate minerals, but there was no evidence of these phases optically or in BSE images.

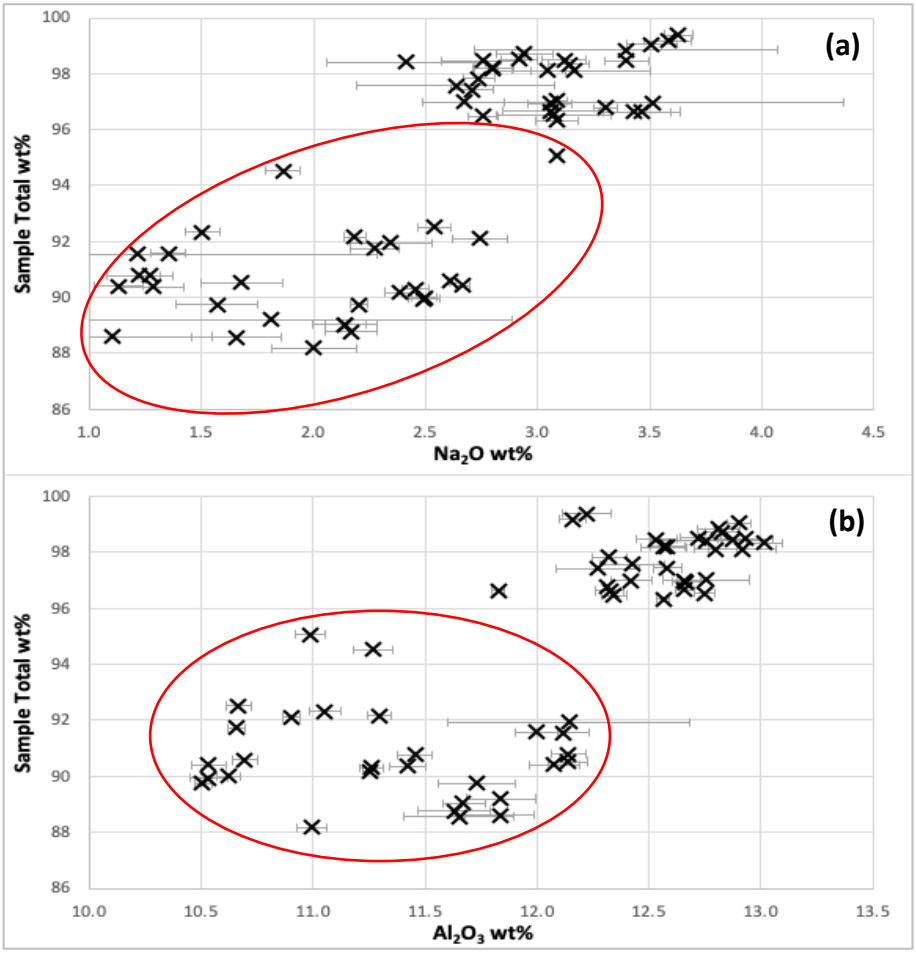

Fig 5.6: *Graphs showing analysis totals plotted against (a) Na_2O and (b) Al_2O_3. Low totals are circled and these analyses are not considered any further. Error bars show standard deviation.*

The likeliest explanation for the lowest totals does appear to be Na_2O and Al_2O_3 loss. Based on the relationships between the totals and Na_2O and Al_2O_3, samples with totals less than 96 wt% are believed to have been affected by Na and Al loss, and as a result are not considered further in the results**.**

5.3.2 Major element content

The SiO_2 and total alkali content ($Na_2O + K_2O$) of the KJ-39 glass chips are displayed in *Fig 5.7* on the total alkali-silica (TAS) classification diagram of Le Bas & Streckeisen (1986). The results show that the chemistry of the glass is quite variable, ranging from andesitic, 58.14 wt% SiO_2, to rhyolitic, 79.89 wt% SiO_2, in composition. Total alkali content ranges from 2.28 to 6.31 wt% and all glass chips are subalkaline. When analyses with totals lower than 96 % are removed (red crosses *Fig 5.7*), the SiO_2 content ranges from 58.21 to 74.51 wt% and total alkali content ranges from 3.52 to 6.14 wt%.

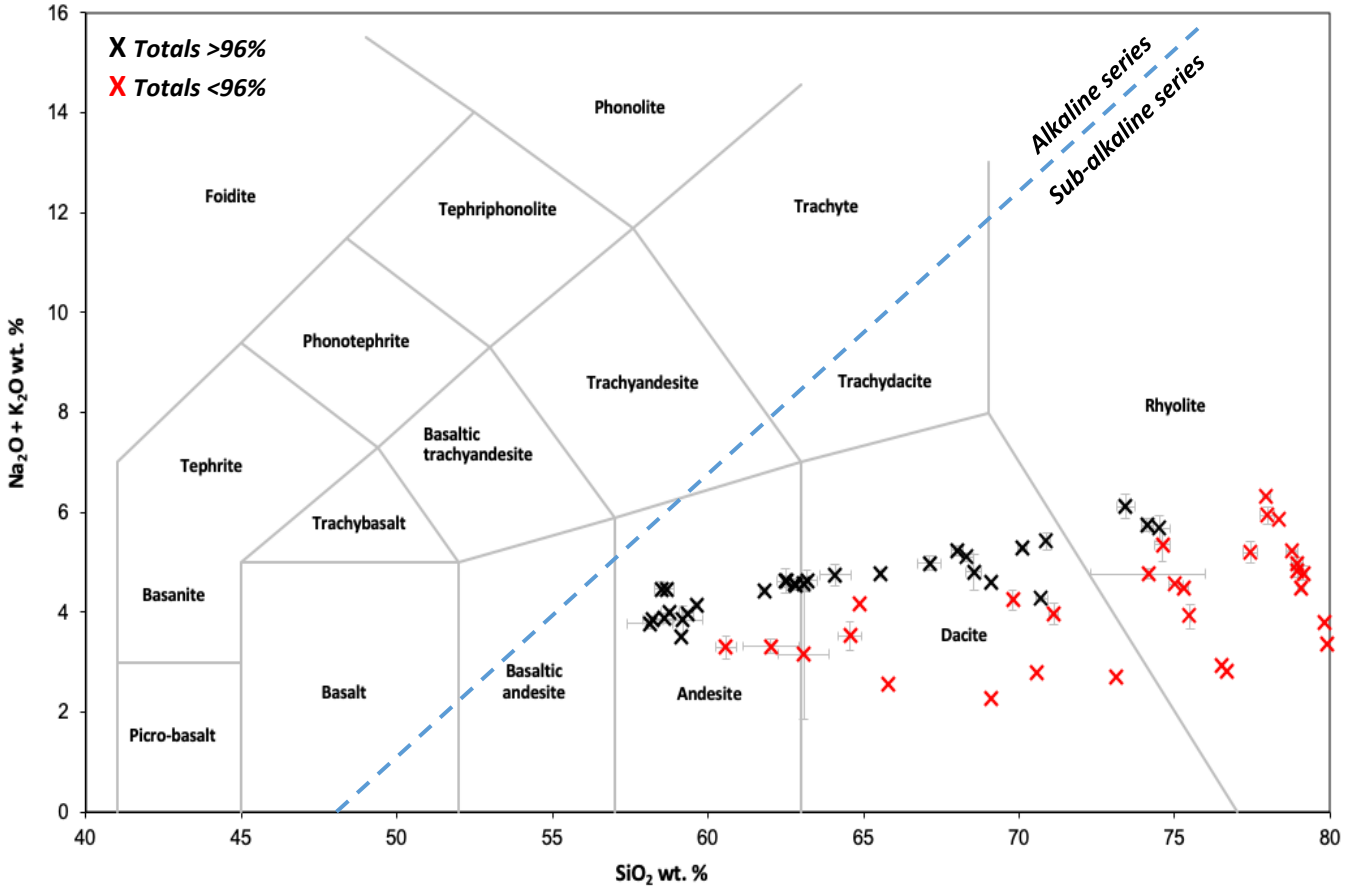

Fig 5.7: *Total-Alkali-Silica (TAS) diagram from Le Bas & Streckeisen (1986) showing the KJ-39 glass chips. The dotted line represents the boundary between the alkaline and sub-alkaline series. Red crosses are analyses with low totals. Error bars represent standard deviation. Concentrations normalised to 100 wt% on an anhydrous basis.*

Analyses with totals lower than 96 % were removed from the analysis and will not be considered further in this study. All of the major element data measured by EPMA was normalised to 100% on an anhydrous basis. Because of this, chips with lower totals will have a larger difference between the measured value and the presented value, particularly for the SiO_2 content, because it is the major component of the melt.

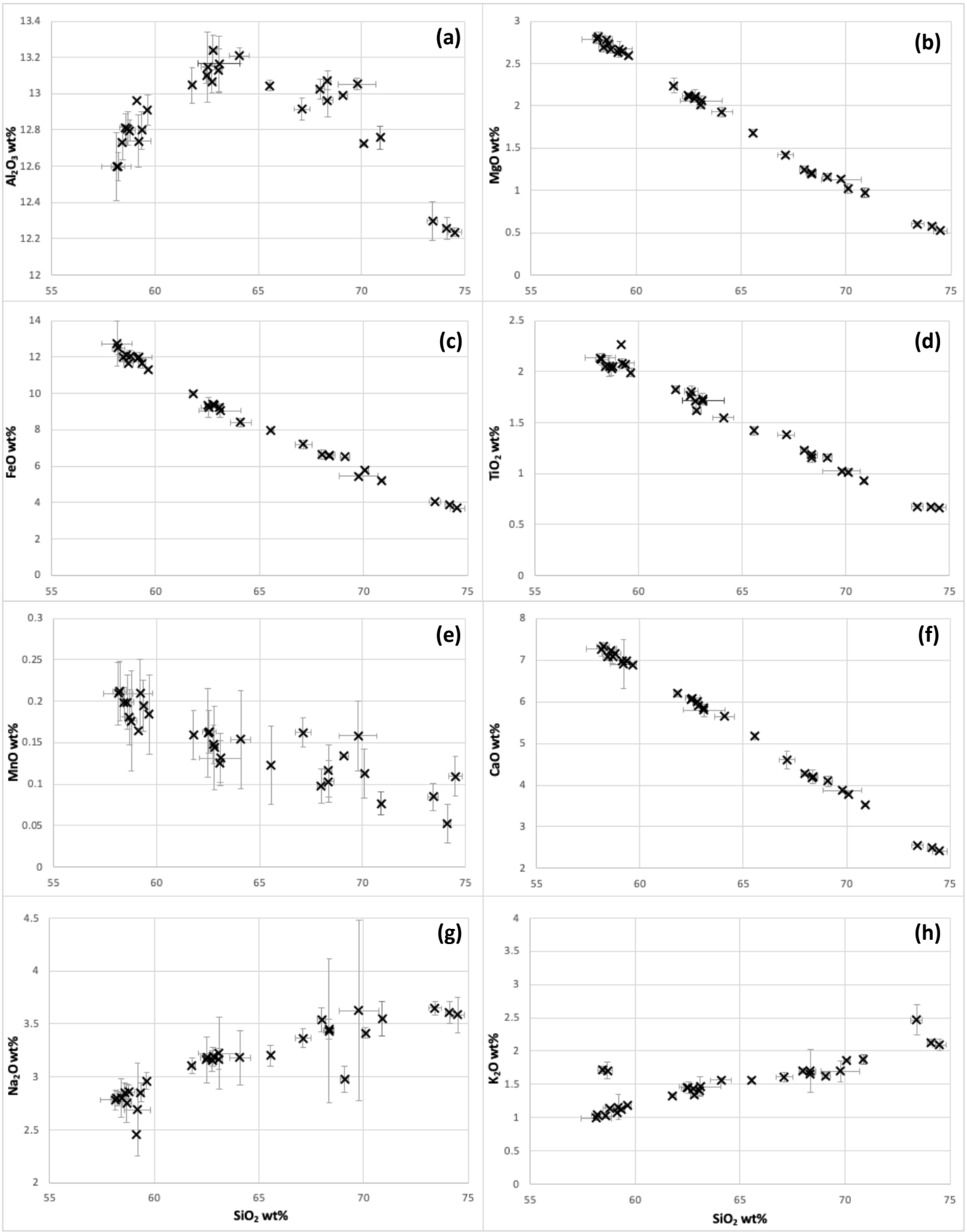

Fig 5.8: *SiO_2 variation diagrams of KJ-39 glass data. Concentrations normalised to 100% on an anhydrous basis. Error bars represent standard deviation.*

SiO_2 variation diagrams show strong negative correlations between SiO_2 and MgO, as well as FeO, TiO_2 and CaO (*Fig 5.8b, c, d, f*). MnO also shows a negative correlation with SiO_2, but the trend shows slightly more scatter (*Fig 5.8e*). The concentration of Al_2O_3 increases until 65 wt% SiO_2 then decreases with increasing SiO_2 (*Fig 5.8a*). There is a weak positive correlation between K_2O and SiO_2 with significant scatter (*Fig 5.8h*). Na_2O also shows a weak positive correlation with SiO_2 (*Fig 5.8g*). Al_2O_3 concentrations range from 12.23 to 13.23 wt% and FeO concentrations span a wide range from 3.61 to 12.70 wt%. CaO contents range from 2.41 to 7.33 wt% and K_2O contents range from 0.99 to 2.46 wt%. MgO contents range from 0.52 to 2.81 wt%, TiO_2 ranges from 0.66 to 2.26 wt%, MnO ranges from 0.05 to 0.21 wt% and Na_2O ranges from 2.45 to 3.62 wt%.

As shown in *Fig 5.9* there is no relationship between the SiO_2 content and the vesicularity of the glass chips.

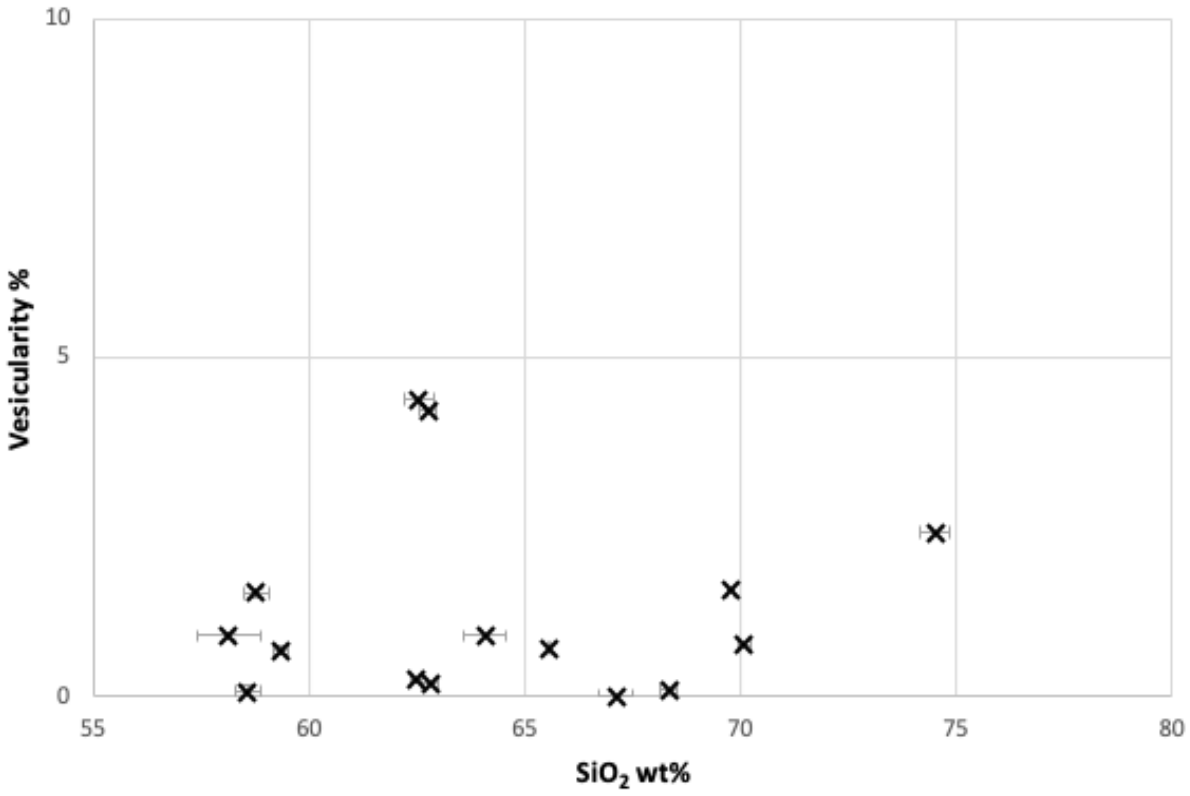

Fig 5.9: *Relationship between SiO_2 content and vesicularity. Error bars show standard deviation.*

5.4 Volatile Contents of Glass

5.4.1 Total Water Content

The total H_2O (H_2O_t) content was analysed using FTIR and firstly water speciation, was examined to determine if the glass was hydrated. Of the chips that were analysed, six were considered to be entirely hydrated, because the mH_2O content plotted well above the speciation model at the same H_2O_t content (*Fig 5.10*) (Seligman et al. 2016). This suggests that these chips were still absorbing water at temperatures below magmatic (~500 °C) (Nowak & Behrens 2001), possibly from the drilling fluid. These chips are not considered any further, and any hydrated analyses from partially hydrated chips have been removed from calculations of the means.

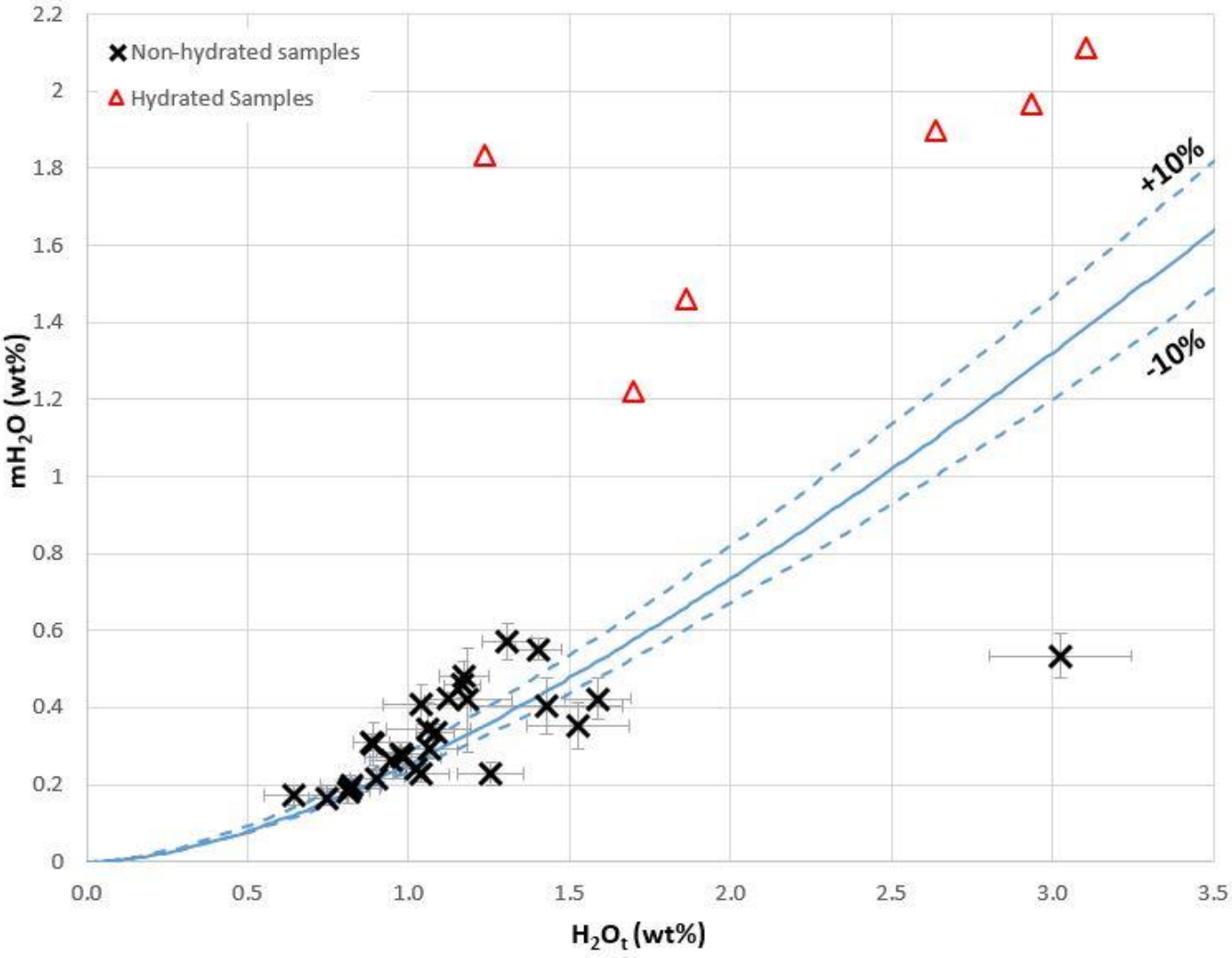

Fig 5.10: *H_2O_t content plotted against mH_2O content for the KJ-39 glass. Red triangles show the hydrated analyses and black crosses are not hydrated. Blue line represents the modelled speciation of mH_2O calculated using the Nowak & Behrens (2001) model at 550 °C. Dotted lines show plus and minus 10% of the modelled line. Error bars show the standard deviation.*

The chips that are not hydrated have H_2O_t contents ranging from 0.63 to 3.02 wt% and all of the chips have higher OH than mH_2O. H_2O_t content was plotted against major element data to determine if there was any correlation between H_2O_t and the magma composition. H_2O_t and SiO_2 show a weak positive correlation, although there is significant scatter within the trend (*Fig 5.11a*). H_2O_t also shows a weak positive correlation with K_2O (*Fig 5.11b*). H_2O_t and MgO CaO, Al_2O_3, FeO and Na_2O are more scattered (not shown).

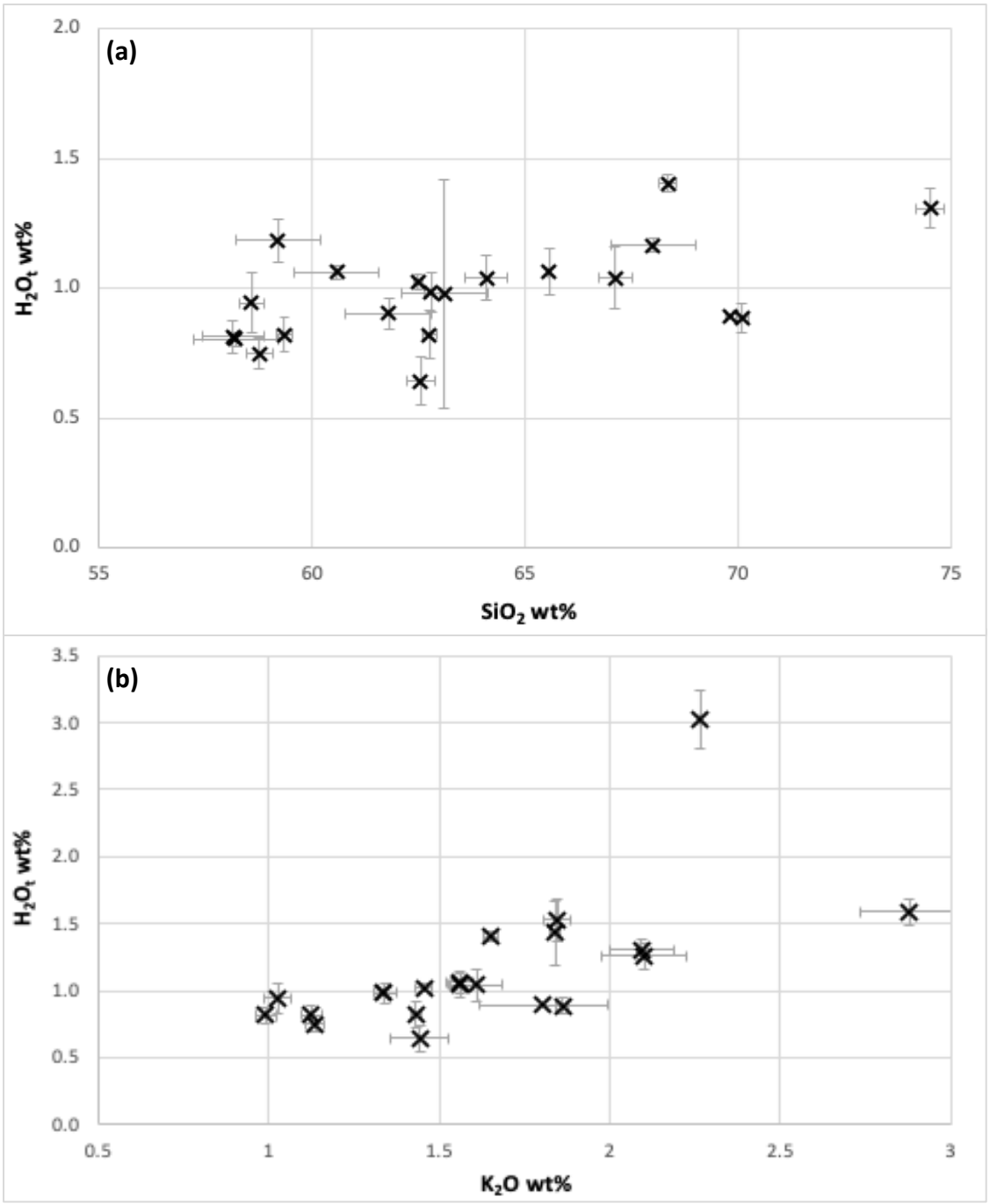

Fig 5.11: *H_2O_t compared to (a) SiO_2 and (b) K_2O. Error bars show standard deviation.*

5.4.2 Water Speciation

The mH_2O concentrations range from 0.15 to 0.57 wt% and all of the chips had lower mH_2O than OH. When plotted on a speciation diagram, chips with low H_2O_t plot close to the Nowak & Behrens (2001) model, which was best fit using a temperature of 550 °C. As H_2O_t contents increases above 1.2 wt% there is more spread within the data, with some chips plotting above and below the speciation model *(Fig 5.12)*. The OH concentration of the glass ranges from 0.13 to 3.12 wt% with averages over individual glass chips ranging from 0.47 to 2.40 wt%.

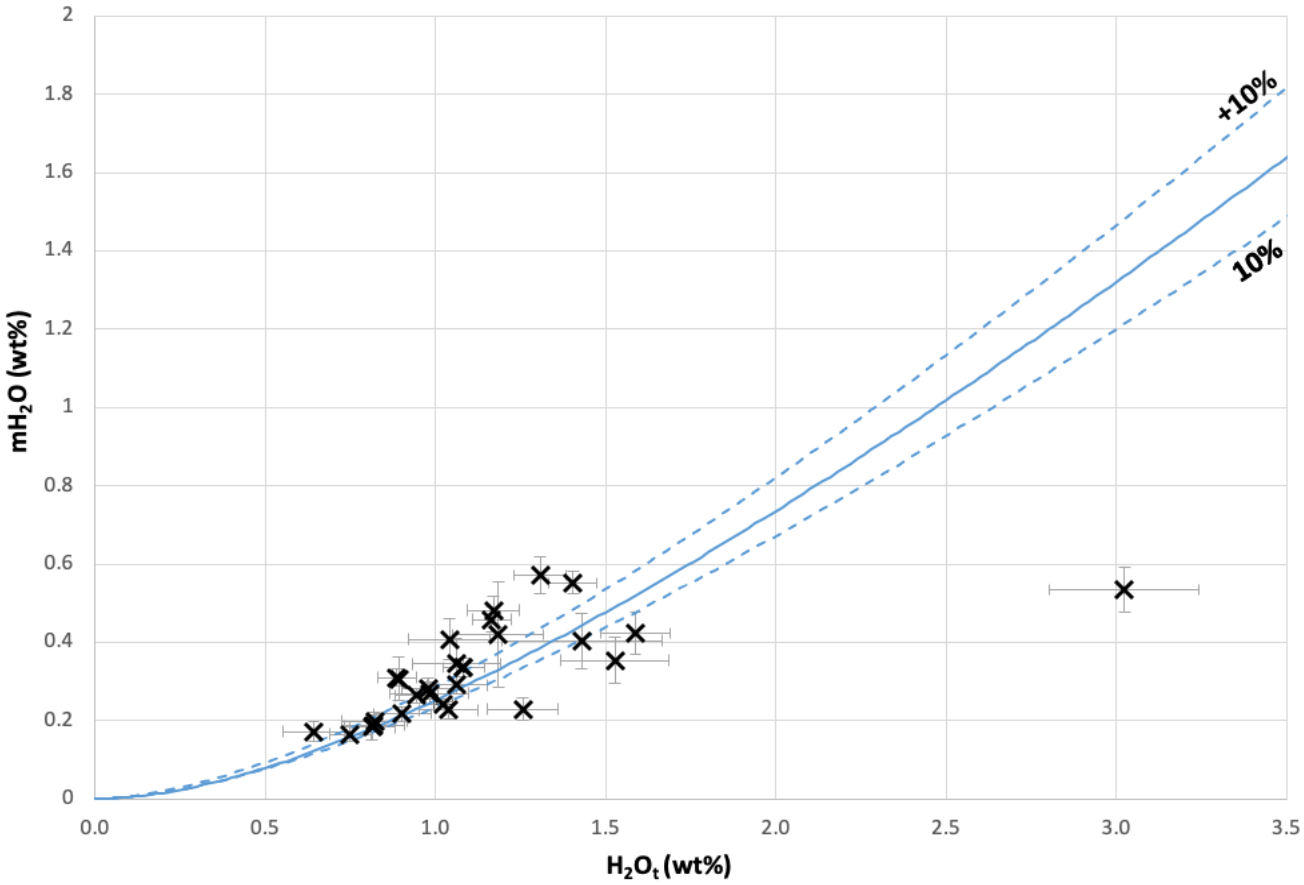

Fig 5.12: *H_2O_t content plotted against mH_2O content for the KJ-39 glass. Blue line represents the modelled speciation of mH_2O calculated using the Nowak & Behrens (2001) model at 550 °C. Dotted lines show plus and minus 10% of the modelled line. Error bars show the standard deviation.*

It is important to note that the speciation model used in this study, from Nowak & Behrens (2001) is designed primarily for use in rhyolites and not all of the glass in the KJ-39 sample is rhyolitic. However, the parameter *W*, representing the anhydrous composition of the glass (Zhang & Ni 2010) is input into the Nowak & Behrens (2001) model during the calculation of the speciation, allowing the model to be composition specific. To produce a speciation model for the entire range of compositions, an average glass composition was used.

5.4.3 FTIR Transects

Transects were measured across the chips in order to identify any variation in H_2O_t contents and H_2O speciation across the chips. The nine chips for which spectroscopic imaging was undertaken using the FPA detector at the Australian Synchrotron were used, as concentrations were measured at a higher spatial resolution (~5.5 μm).

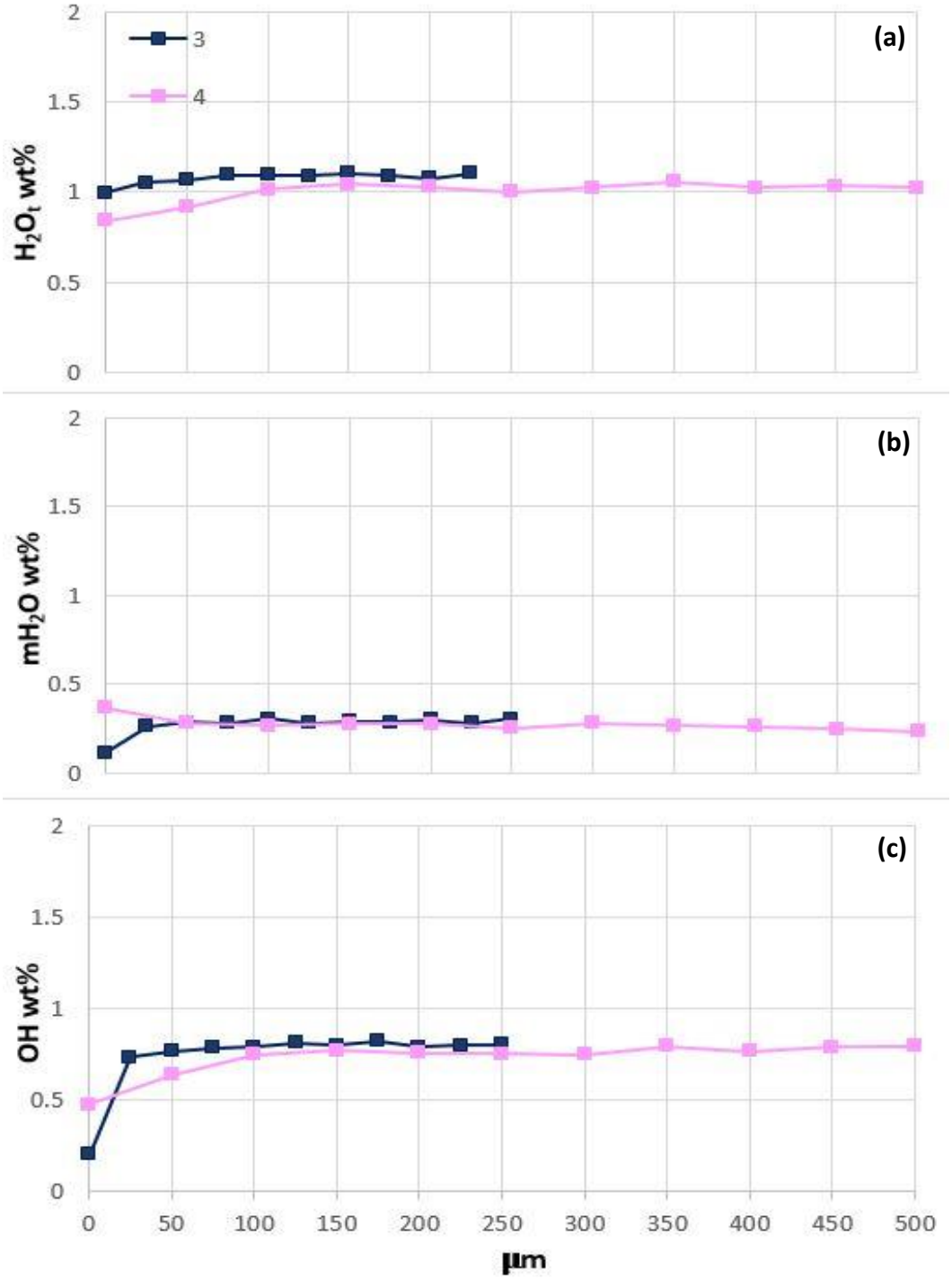

Fig 5.13: *FTIR transects from one edge of the chip to the other for glass chips showing no change in H_2O_t across the centre of the chips. (a) H_2O_t (b) mH_2O and (c) OH. X axis shows distance across chip in microns.*

Chips 3, and 4 show minimal variation in H_2O_t contents across the chip (*Fig 5.13*), which is mirrored by the mH_2O and OH contents. Chips 1, 5, 8, and 11 show an increase in H_2O_t towards the centre of the chip, then decrease towards the edges of the chip (*Fig 5.14*). These patterns are mirrored by the OH content for all of the chips, and the mH_2O of chip 5, which has a zone on the left of the chip that has higher mH_2O content. The mH_2O contents of the other chips show minimal variation across the chips.

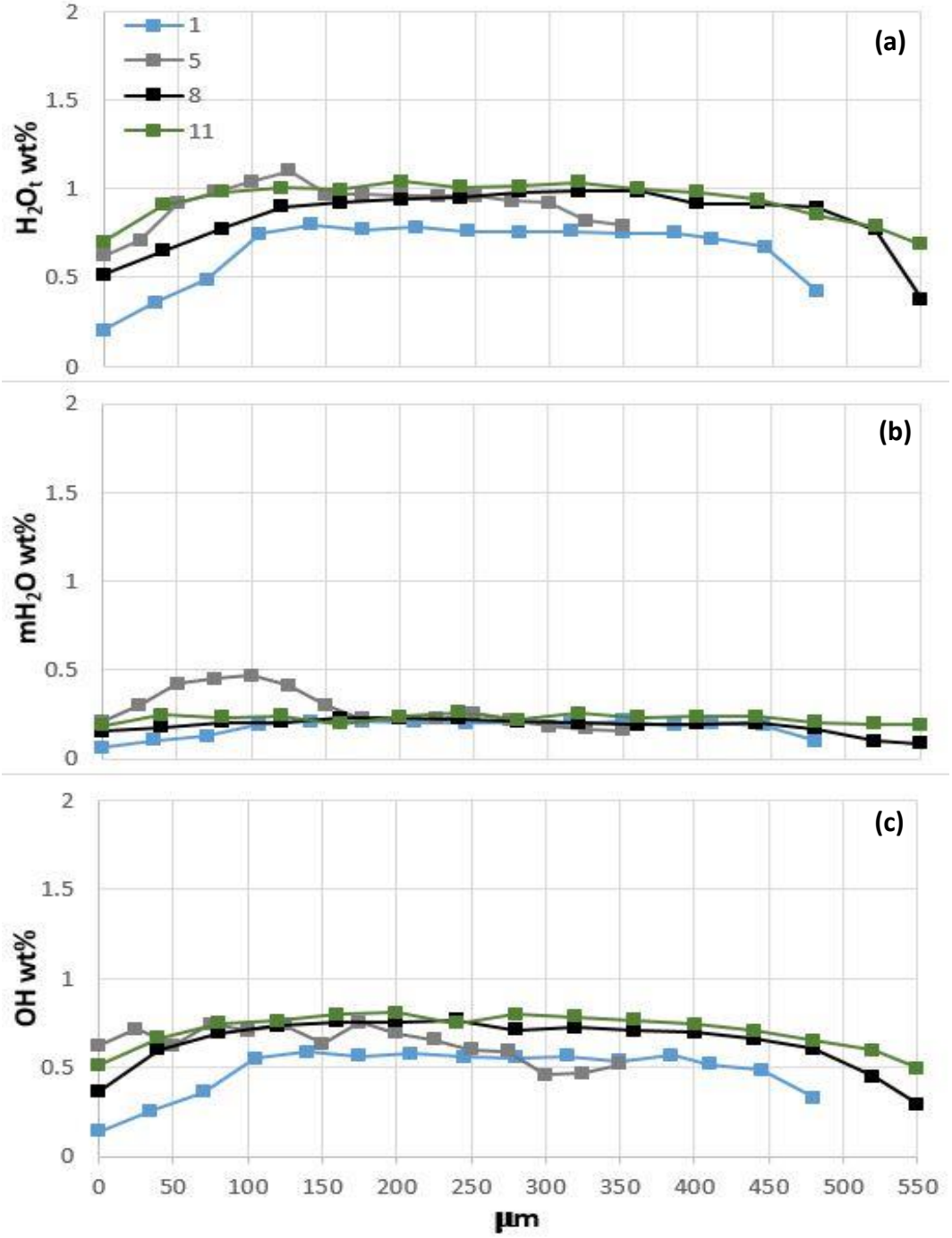

Fig 5.14: *FTIR transects from one edge of the chip to the other for glass chips showing an increase in H_2O_t towards the centre of the chips from both edges. (a) H_2O_t (b) mH_2O and (c) OH. X axis shows distance across chip in microns.*

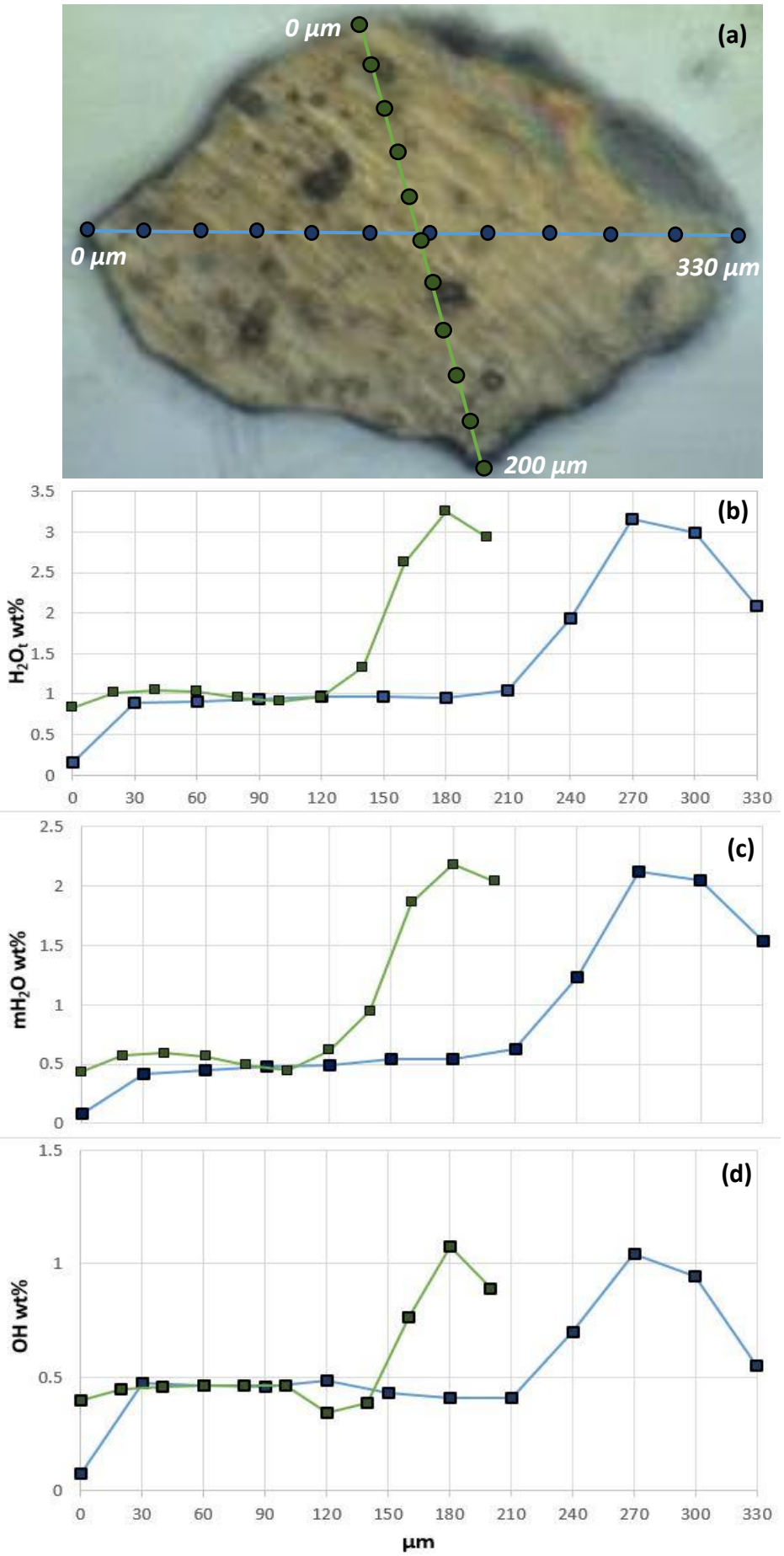

Fig 5.15: *FTIR transects for chip 7. (a) FTIR image showing location of transects. (b) Transect H_2O_t, (c) mH_2O and (d) OH. X axis shows distance across chip in microns.*

Chip 7 shows a flat pattern across one side of the chip, then a sharp increase in the H_2O_t content, which is mirrored by the mH_2O and OH contents (*Fig 5.15*). The absorbance image for the whole chip (*Fig 5.16*) shows that there was elevated absorbance along three edges of the sample, for H_2O_t, OH and mH_2O. Chip 7 was the only chip of those analysed that showed this pattern. Because reflectance data cannot be obtained using the FPA detector, a constant thickness was inferred across the whole chip.

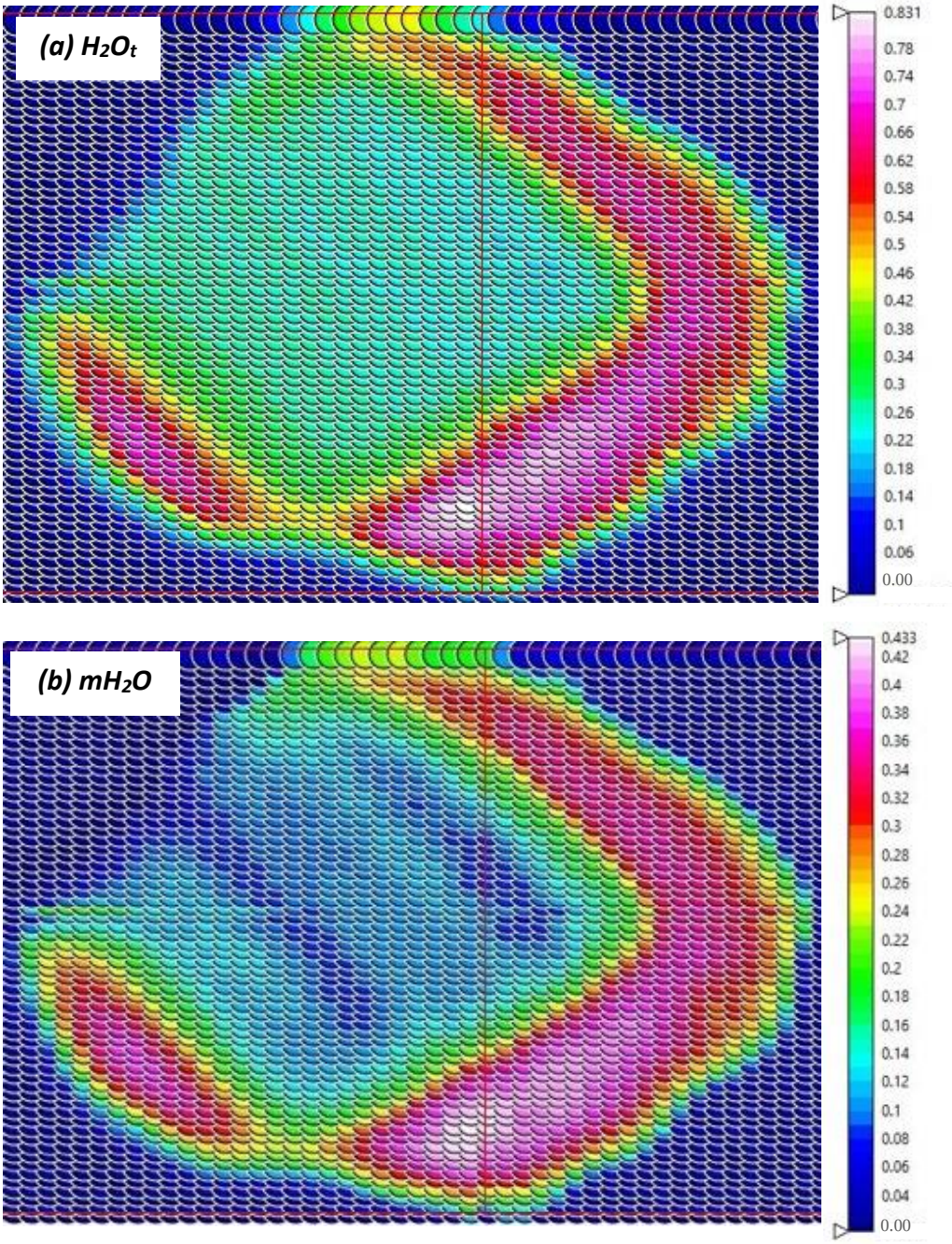

Fig 5.16: *FTIR absorbance images of (a) H_2O_t from the 3500 cm^{-1} peak and (b) mH_2O from the 1630 cm^{-1} peak showing the increase in absorbance around the edges. Numbers on the scale are absorbance.*

The thickness of the chip was 25 µm, calculated from the reflectance spectra measured using the MCT detector on the FTIR at the University of Canterbury (*Section 4.43*) and confirmed by the digital micrometer measurements.

5.4.4 CO_2

Because CO_2 speciation depends on the composition of the melt (Zhang et al. 2007), and the wide range of SiO_2 in the KJ-39 glass chips, CO_2 may be present as mCO_2 and CO_3^{2-} in the chips (*Section 3.3.4*). However, during the analysis of the volatiles on the FTIR, there were problems with the automated joystick moving without being touched. Because of this, chips analysed in the first group of FTIR analysis (Group 2) were left open to the atmosphere to avoid the chips being swept off the machine. No double peaks were seen at 1515 and 1435 cm^{-1} in any of the FTIR spectra (both Group 1 and Group 2), representative of CO_3^{2-} (Newman et al. 1986, Stolper 1989) and mCO_2 peaks were mostly poorly defined and obscured by atmospheric CO_2 double peaks. CO_2 could only be detected in seven of the chips, ranging from 5 to 40 ppm.

5.4.5 Sulphur, chlorine and fluorine

S contents range from below detection, approximately 9 ppm (Schipper et al. 2019), to 1373 ppm and show a strong negative correlation with SiO_2 (*Fig 5.17a*). F also shows a negative correlation with SiO_2, but not as strong as S and has maximum abundance of 1868 ppm *(Fig. 5.17b)*.

***Table 5.2**: Table outlining the standards measured using the electron probe and the published values from Jochum et al. (2005).*

	VG2		VG568		VGA99	
	Measured	**Published**	**Measured**	**Published**	**Measured**	**Published**
S	1571	1466.53	20	19.68	200	139.24
Cl	300-900	731.36	1400-1968	2276.80	874-1021	631.24
F	0.025-500	344.29	900-1400	1121.14	195-238	207.79

Cl shows a positive correlation with SiO_2 with a wider spread of data than the S and F, ranging from 474 to 851 ppm *(Fig 5.17b)*. When S, F and Cl were plotted against H_2O_t *(Fig 5.18)*, S shows a weak negative correlation with H_2O_t, as does F, and Cl has a weak positive relationship. Standards measured and the published values are presented in *Table 5.2*.

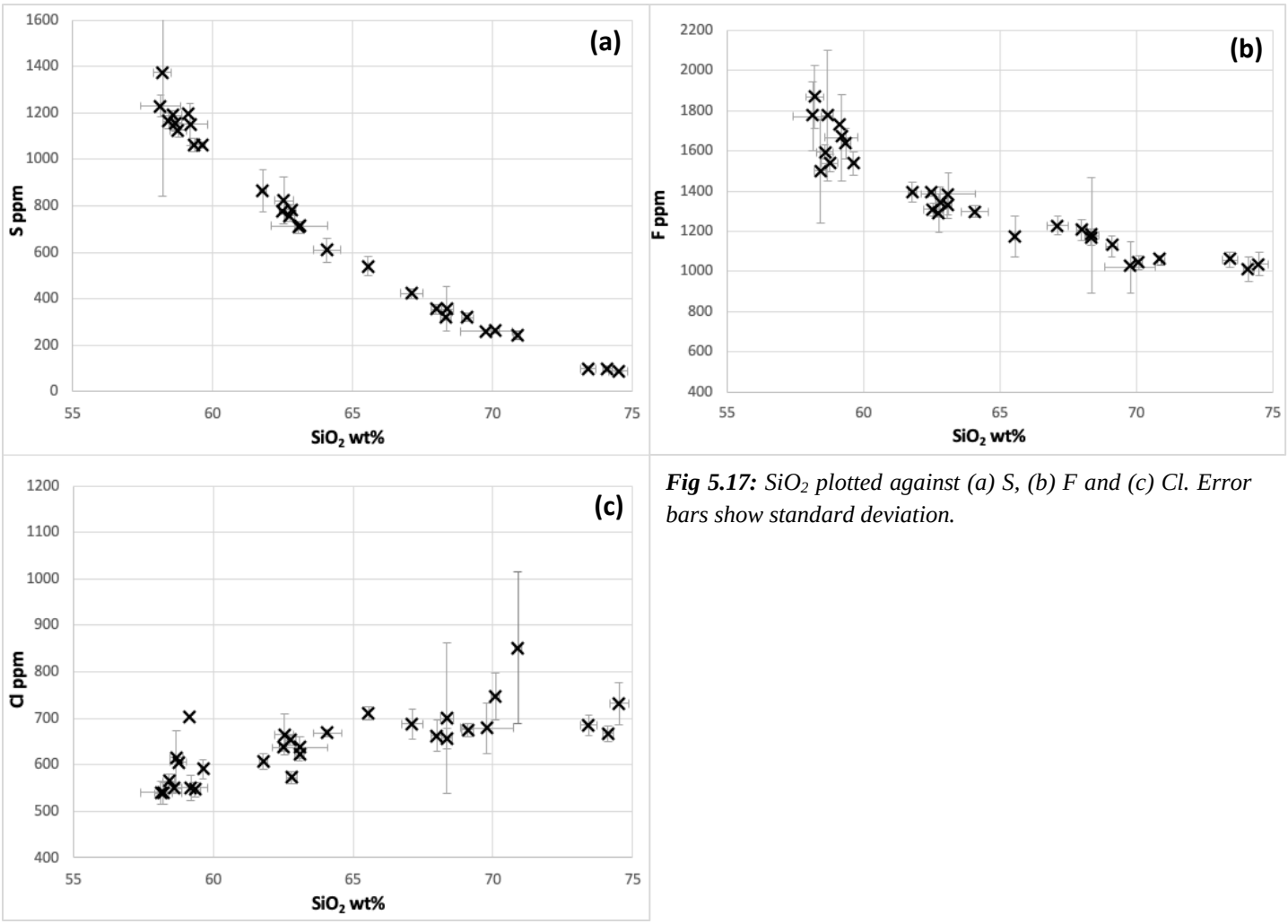

Fig 5.17: *SiO_2 plotted against (a) S, (b) F and (c) Cl. Error bars show standard deviation.*

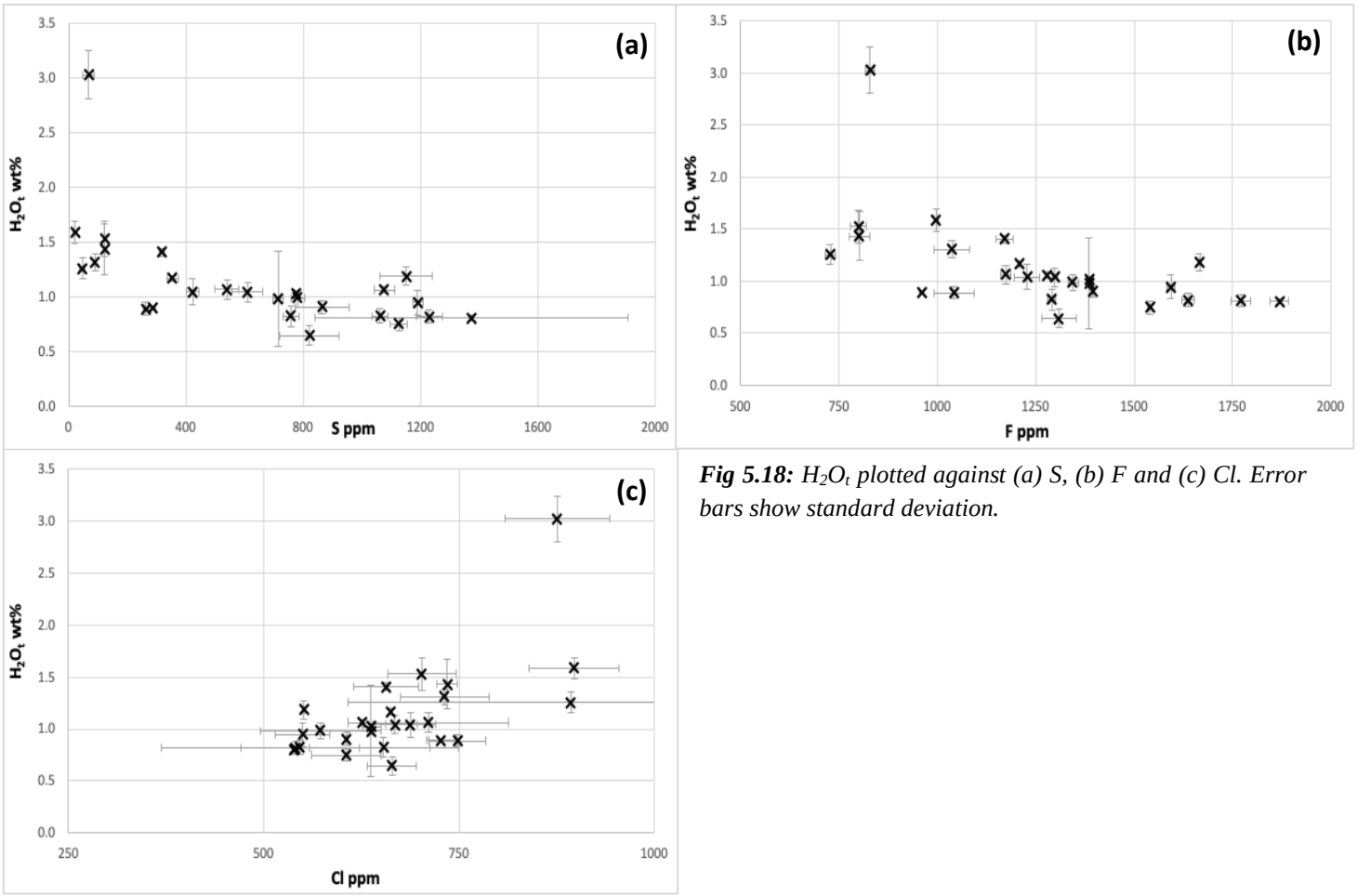

Fig 5.18: *H_2O_t plotted against (a) S, (b) F and (c) Cl. Error bars show standard deviation.*

5.5 Mineral Assemblage

As well as the glass that was returned to the surface, which comprised approximately 30% of the total cuttings, a phenocryst assemblage identified as basaltic by Mortensen et al (2010), consisting of augite, plagioclase and minor titanomagnetite was also retrieved. In this study smaller concentrations of iron-copper-sulphides were found in the glass and melt inclusions were observed in some crystals (*Fig 5.19*). Because of time constraints, the melt inclusions have not been analysed.

The BSE images show zoning within the plagioclase and exsolution lamellae in the augite *(Fig 5.19a, c respectively).* EPMA data suggests that the plagioclase is mostly bytownite with a few crystals falling in the anorthite field, with An numbers ranging from 69.1 to 95.6 (*Fig 5.20*).

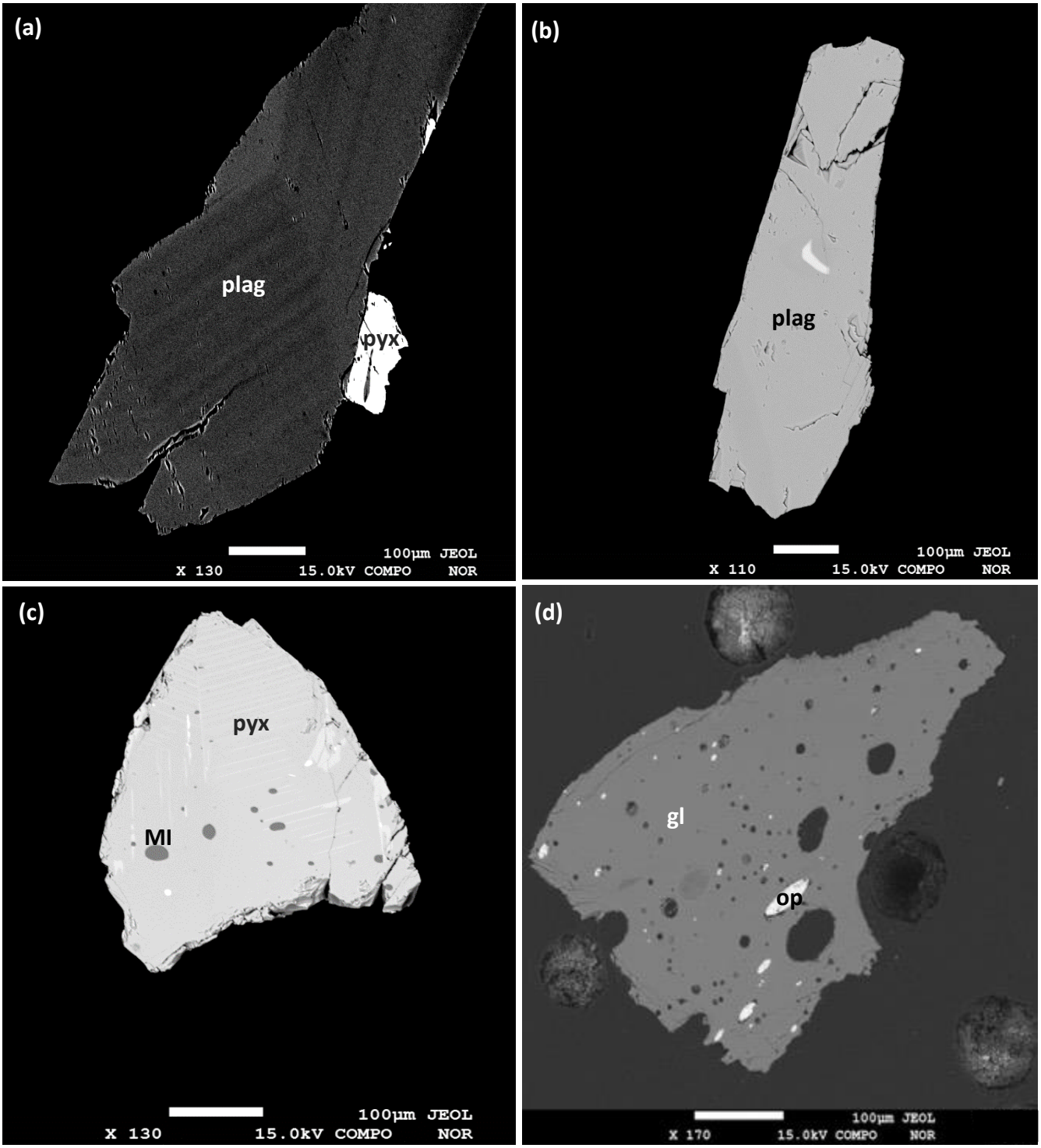

Fig 5.19: *BSE images taken during EPMA analysis showing the mineral assemblage present in the KJ-39 sample. (a) Plagioclase (plag) crystal showing zoning with enstatite pyroxene (pyx) crystal attached. (b) Plagioclase crystal with opaque in the centre. (c) Augite crystal with melt inclusions and lamellae. (d) Vesicular glass (gl) with opaque pockets (op). Plagioclase crystals in (a) and (b) appear different colours because of differences in the contrast and brightness when the*

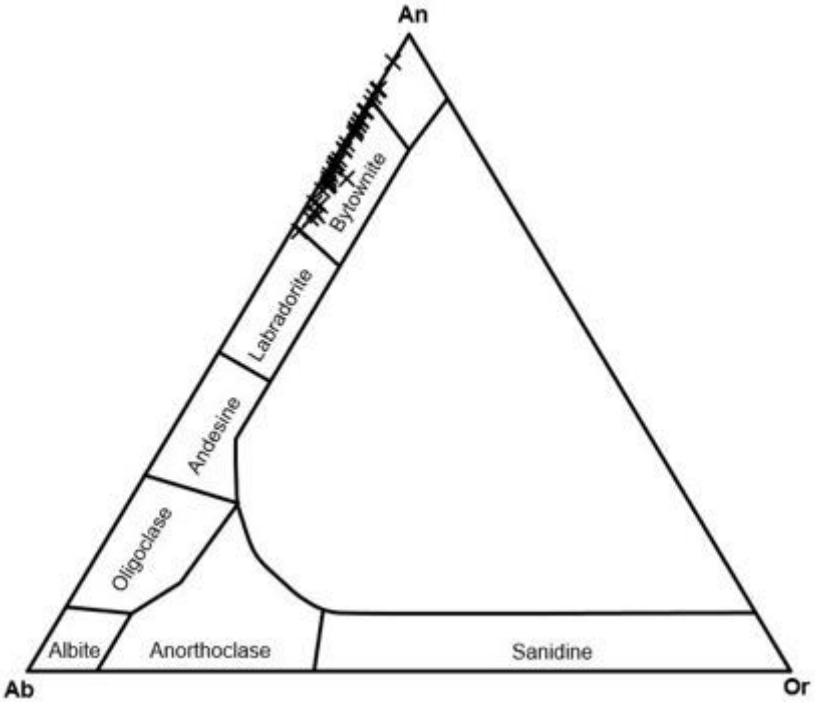

***Fig 5.20**: Feldspar ternary diagram from Marshall (1996) showing the composition of feldspar crystals in KJ-39 measured in this study.*

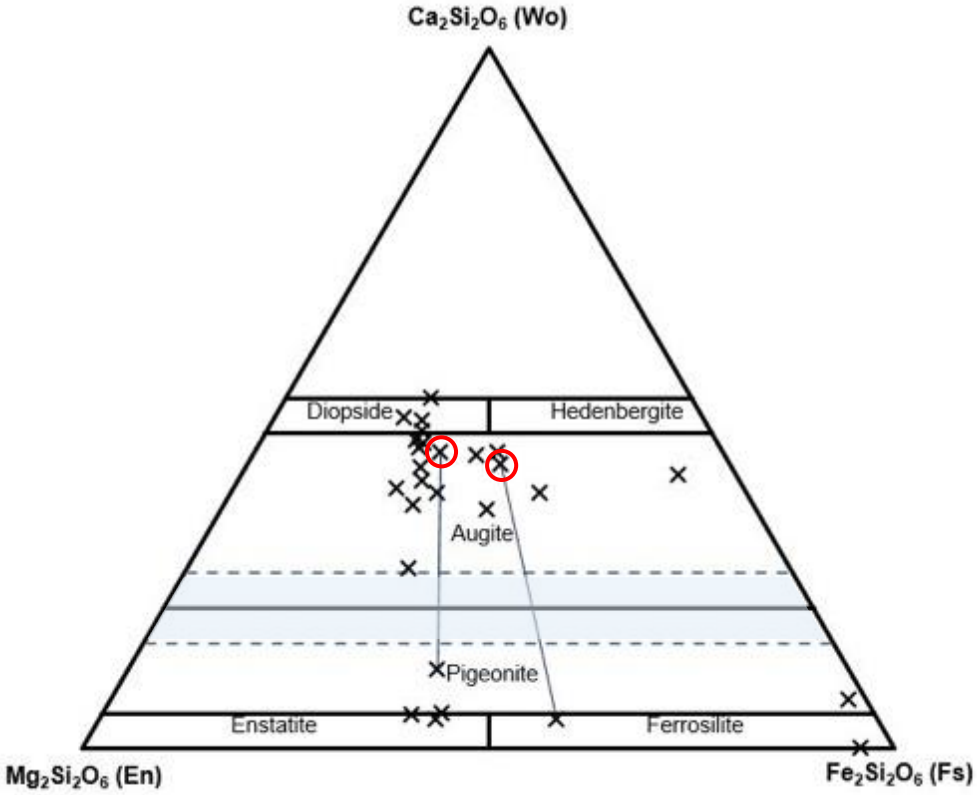

***Fig 5.21**: Pyroxene ternary diagram from Morimoto (1988) showing compositions of the pyroxenes from KJ-39 measured in this study. Blue area represents miscibility gap, lines joining points show measurements from the same crystal, host crystal is circled.*

Pyroxenes in the KJ-39 sample have exsolution lamellae (*Fig 5.19c*) of pigeonite or ortho-pyroxene hosted in augite *(Fig 5.21).* The presence of the two pyroxenes means that an in-situ temperature estimate of the magma can be made using the two-pyroxene geothermometer (Purtika 2008) (*Section 4.5*).

5.5.1 Opaques

The opaques were found within the glass chips of sample KJ-39 (*Fig 5.19d*). These opaques range in size, with a maximum length of approximately 10 μm and a maximum width of approximately 5 μm. They also range in shape, from spherical to elliptical but are always rounded.

Energy dispersive x-ray spectroscopy (EDS) analysis, using the EPMA, identified these opaques as being rich in copper and iron. They were then analysed for metals using the EPMA, to identify their relative abundance. Some analyses produced totals as low as 32 %, and thus were likely measured on the boundary between the opaques and the surrounding glass. Because of this, all opaques with totals lower than 90 % were discarded. The average analyses are summarised in *Table 5.3*.

Table 5.3: *Average composition of the metals in the opaques found within the glass, measured by EPMA. The average composition is outlined along with the standard deviation and the number of samples measured (n).*

	wt%	St Dev	n
S	32.58	2.75	5
Mo	0.65	0.06	5
Zn	0.02	0.02	5
Si	0.12	0.07	5
Ni	1.12	0.52	5
Co	0.79	0.27	5
Ag	0.01	0.01	5
Pb	0.00	0.01	5
Cl	0.01	0.00	5
Fe	54.28	1.37	5
Cu	5.60	2.05	5
Au	0.01	0.01	5

Opaques showed Si content lower than 1 wt%, high Fe contents ranging from 52.98 to 55.74 wt% and S contents ranging from 30.81 to 37.46 wt%. These opaques also contain Cu contents ranging from 2.26 to 7.48 wt % and minor amounts of Ni ranging from 0.76 to 2.02 wt%. These data are presented in *Fig 5.22*.

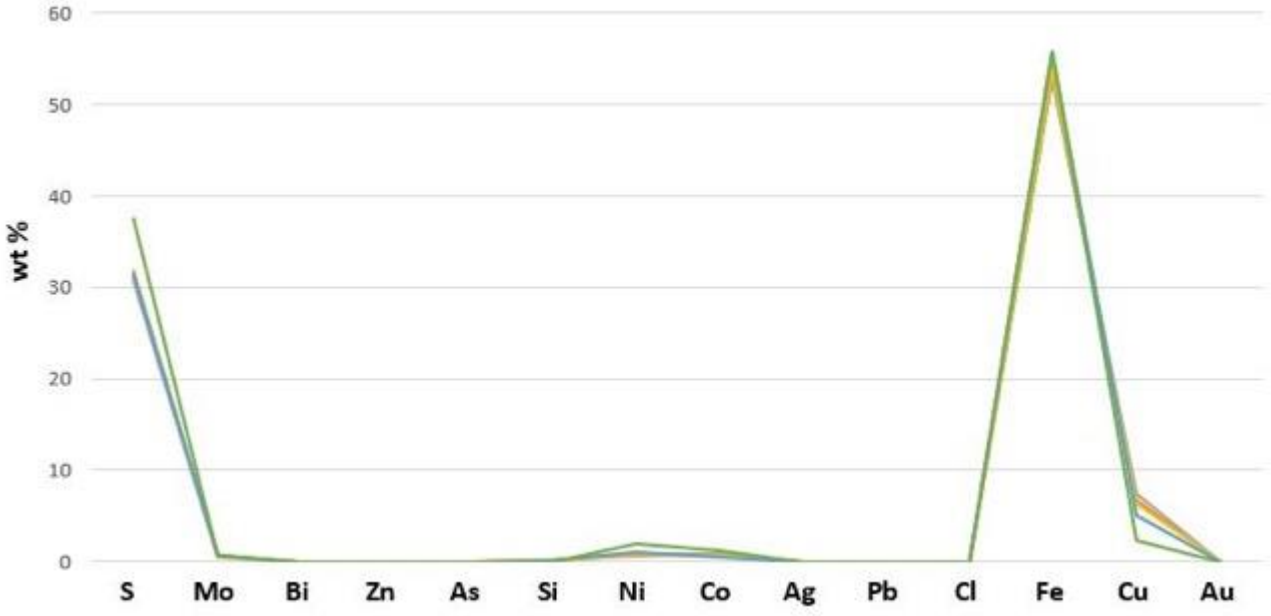

***Fig 5.22**: Plot showing the metal composition of the opaques found in the sample set.*

5.6 Summary

This chapter presents the results of the analysis of the KJ-39 sample. All glass chips analysed were brown and ranged in vesicularity; highly vesicular (>5 % vesicles) and non-vesicular (<5 % vesicles) based on BSE images. The shape of the vesicles varies between spherical and elliptical.

The glass has a wide range of SiO_2 content, varying from andesitic (58 wt%) to rhyolitic (75 wt%). The total alkali (Na_2O+K_2O) content ranges from 3.5-6.1 wt% and all the chips plot in the subalkaline field. The H_2O_t contents range from 0.63 to 3.02 wt % and all of the chips have higher OH than mH_2O. CO_2 could only be detected in seven chips, measuring concentrations ranging from 5-40 ppm, but most of the samples had contamination from gaseous CO_2 in the atmosphere. SiO_2 and K_2O are positively correlated, while SiO_2 and MnO, TiO_2, Al_2O_3, MgO, FeO and CaO exhibit strong negative correlations. The volatiles S and F show negative

relationships with SiO_2, and Cl shows a positive relationship. There is no correlation between major element composition and vesicularity or crystallinity.

The mineral assemblage present is representative of a basalt, with plagioclase, primarily bytownite with some oscillatory zoning, and pyroxene, mostly augite, with some low Ca orthopyroxene lamellae. The sulphides present in the glass are identified to be iron-copper-sulphides.

The implications of these results will be discussed in Chapter 6.

6 Origin of the KJ-39 Magma and the Relationship with IDDP-1

6.1 Introduction

This chapter will address the main aims of the project; to examine the origin and evolution of the magma that was intersected during the drilling of KJ-39 by using the major element analyses and volatile compositions presented in Chapter 5. I will also compare the KJ-39 magma and the IDDP-1 magma, using geochemical data from the literature, to determine any relationship between the two.

6.2 KJ-39 magma

6.2.1 Major element data

The TAS classification diagram (*Fig 5.7*) shows that there is a wide range of compositions within the KJ-39 sample. This range could be explained by crystallisation trends as the melt evolves, with MgO and FeO being removed by pyroxene, TiO_2 and FeO removed by Fe-Ti oxides and CaO removed by clinopyroxene and Ca-rich plagioclase. The inflection in the Al_2O_3 indicates the point at which plagioclase crystallisation becomes the dominant process, at approximately 65 wt% (Rollinson 1993). Alternatively these trends could be explained by the reverse, as a rock is re-melted. The linear trends of SiO_2 with MgO, FeO, TiO_2 and CaO could also be explained by simple binary mixing of basaltic-intermediate composition and rhyolitic end-member compositions. However, there is no direct evidence of mixing within the chips, with minimal variation in composition and no mingling textures within individual chips.

6.2.1.1 Previous study

The KJ-39 sample has been previously studied by Mortensen et al. (2010) who identified the cuttings as up to 30% fresh rhyolitic glass and a basaltic mineral assemblage of plagioclase, clinopyroxene, opaque oxides and minor olivine. The study measured SiO_2 contents from 68.9 – 78.7 wt%, which is a narrower range than the data obtained from this study (58.2 – 74.5 wt%) and, as discussed above (*Section 5.3.1*), the samples had totals between 92-95 wt%. Mortensen et al. (2010) noted the anomalously high corundum content (4-5 wt%) as well as the strong sub-alkaline pattern of the samples and because of this, speculated that the KJ-39 magma was formed by anatexis, or partial melting, of a hydrated basalt at depth, forming an isolated pocket of high-SiO_2 rhyolite. This process has been observed worldwide and is known to occur in the early stages of contact metamorphism (Droop et al. 2003; Mortensen et al. 2010).

The reason for the wider range of major element compositions in this study compared to that of Mortensen et al. (2010) could be a result of a bias in sample selection towards a specific kind of chip e.g., the largest or darkest brown chips were selected. Twenty-two analyses were undertaken in the Mortensen et al. (2010) study, although it is unclear whether this was 22 separate chips, or multiple analyses on fewer chips. The study here carried out 312 glass analyses, on 59 chips, so the wider range of results may be a factor of the greater number of samples that were analysed.

Using the evidence from major element diagrams, and information from the Mortensen et al. (2010) study, I infer that the major element patterns are primarily produced by re-melting processes. Although crystallisation could produce similar patterns, it would not cause the partial melting textures seen in the mineral assemblage (*Section 6.3*).

6.2.2 Volatile contents

The volatile contents of the KJ-39 glass have not been previously measured so this study provides the first ever volatile data.

6.2.2.1 Water

The glass chips were stuck at the base of the well for approximately a week before being recovered (Mortensen et al. 2010). Therefore, there is a possibility that there has been alteration of the glass by the circulating water used for drilling and thus the water concentrations may represent secondary hydration, rather than the original magmatic water content. As a result, firstly water speciation, measured by FTIR, was used to determine if the glass was partially hydrated (*Section 5.4*) and any affected analyses were removed.

Figs 5.13 and *5.14*, show that most of the chips with transects have lower H_2O_t contents at the edge of the chips that increase towards the centre, with two showing no variation across the entire chip. In the samples that have increased H_2O_t across the centre of the chip, the mH_2O remains stable, while the OH increases for all but one. This increase in OH across the centre of the chips is in accordance with the equilibrium speciation at these H_2O_t contents. At low H_2O_t, the OH increases more sharply while the mH_2O remains stable (Stolper 1982, Burnham 1975). Chip 5 (*Fig 5.14*) shows an increase in mH_2O across the centre of the chip, while the OH content is very variable. This pattern could be because the water in this chip was added at temperatures below magmatic. If this was the case, any H_2O added to the chip would remain

as mH_2O because there is insufficient energy to convert the mH_2O into OH (Seligman et al. 2016). Lower H_2O_t contents at the edges of the chips indicates degassing and diffusion of OH towards the margins of the chips (Von Aulock et al. 2017) and could explain the patterns shown in *Fig 5.14*.

When H_2O_t is plotted against vesicularity there is no correlation (*Fig 6.1*). A positive correlation could suggest secondary hydration from the drilling fluid circulating the well, because samples with higher percentage vesicularity would provide a larger surface area for the water to enter the glass. However, preparing highly vesicular samples for analysis, for both FTIR and EPMA, was very difficult as they were more likely to break during the preparation process. The highly vesicular samples were also more susceptible to break along the boundaries of the vesicles so the total vesicularity values may be under-representative as it is unclear what is the edge of the glass and what is the edge of a bubble. Therefore, the vesicularity data may not be representative of the whole sample set.

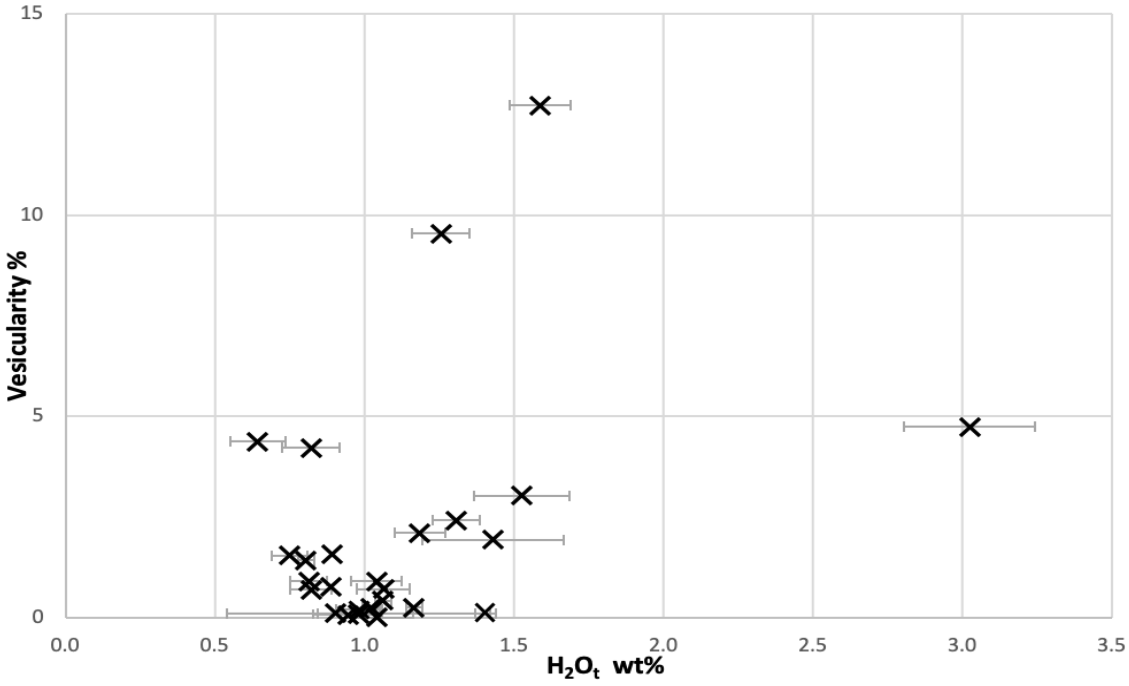

Fig 6.1: *H_2O_t contents plotted against vesicularity, measured using ImageJ on BSE images taken on the electron microprobe. Error bars show standard deviation.*

Chip 7 shows an interesting pattern, with H_2O_t showing a consistent concentration across most of the chip, then rapidly increasing approximately two thirds of the way across the glass chip (*Fig 5.16*). The fact that mH_2O, OH and H_2O_t all increase suggests that this pattern is not due

to secondary hydration; if this was the case you would see constant OH across the chip. Careful analysis of the absorbance spectra was carried out in order to identify whether this pattern was due to crystal bond leftover on the chip and contaminating the spectra, but there was no evidence for this. It could be a matter of the edge of the chip being thicker than the centre, but it would need to be approximately double the thickness, which would be clearly observable and this was not the case. The speciation for chip 7 (*Fig 6.2*) shows the group of low H_2O_t and low mH_2O analyses, from the centre of the chip (circled) and an increase in mH_2O and OH as H_2O_t increases at the edge.

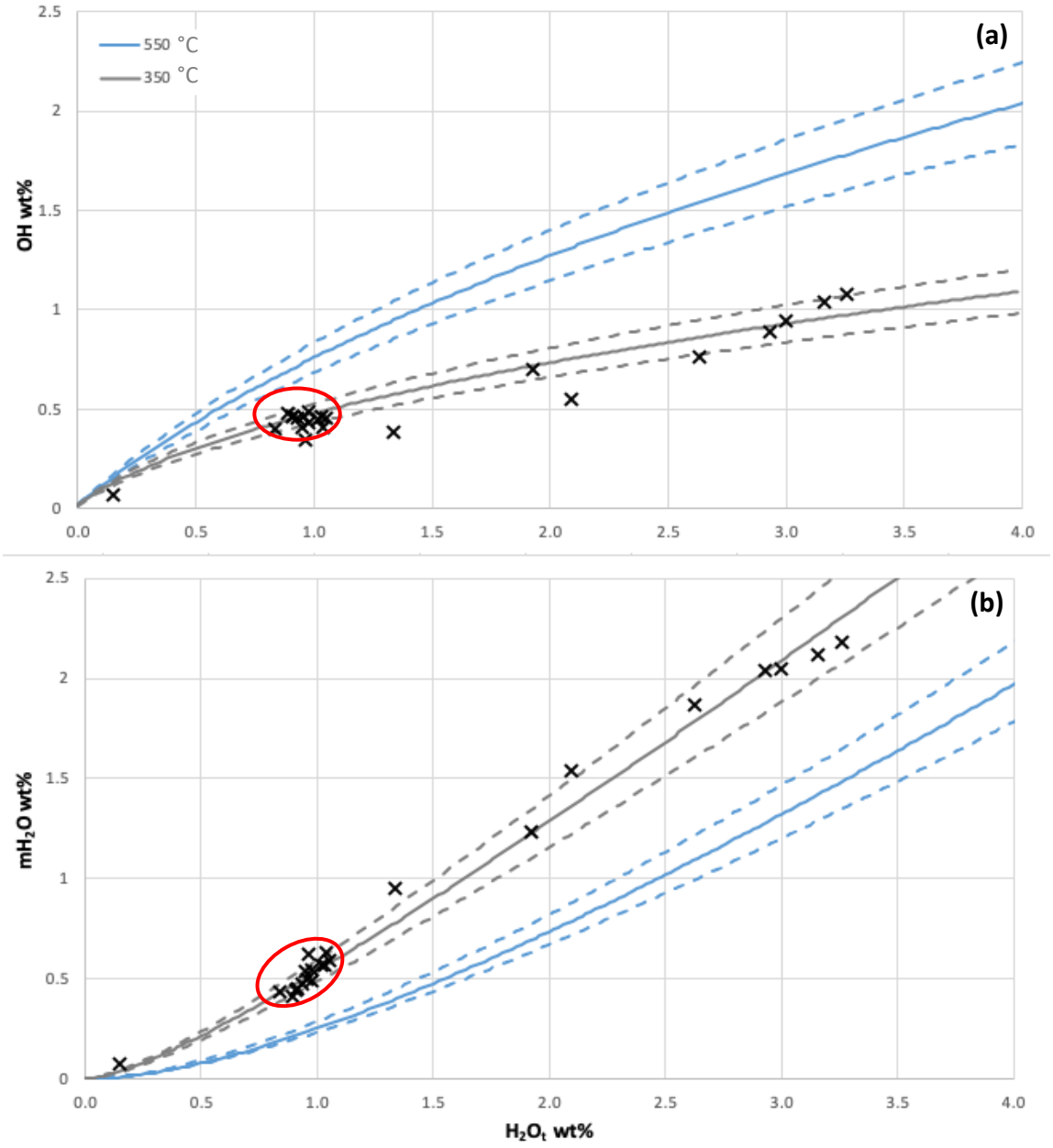

Fig 6:2: *Speciation models showing (a) the OH and (b) mH_2O contents plotted against H_2O_t of individual analyses from chip 7. Blue line shows speciation model from Nowak & Behrens (2001) at a temperature of 550 °C and grey line at 350 °C, with dotted lines showing +10 and -10 % of the models. Circled are the analyses from the centre of the chip.*

The reason for the increased OH and mH_2O could be because of water resorption at magmatic temperatures (McIntosh et al. 2014, where the melt resorbs water from the bubbles as it cools and the solubility increases at temperatures high enough to allow the conversion between the OH and mH_2O species to continue (Stolper 1982a). If the melt was quenched fast enough, this speciation would be preserved.

The pattern of chip 7 could also be explained by slow cooling, approximately 35 °C per minute (Zhang et al. 1997), which would allow the mH_2O and OH species to continue to interchange until the glass is quenched (Zhang et al. 1997). *Fig 6.2* shows that a speciation model at an apparent equilibrium temperature of 350 °C best fits the speciation of this chip, however, the Nowak & Behrens (2001) model is not calibrated for such low temperatures. Alternatively the whole chip is hydrated, with the middle, hydrated to a lesser extent than the edges, because these analyses plot closer to the speciation model.

Using the evidence above, I suggest that the patterns displayed in *Fig 6.2* for chip 7 are probably the result of water resorption at magmatic temperatures with the melt absorbing water from bubbles as it cools.

6.2.2.2 Sulphur, chlorine and fluorine

The relationship between S and SiO_2 is strongly negative (*Fig 5.17a*) as is the relationship between F and SiO_2 (*Fig 5.17b*). Cl shows a positive relationship with SiO_2 (*Fig 5.17c*), as is expected because it behaves incompatibly and thus remains in the melt longest (Balcone-Boissard et al. 2010). The scatter for F and Cl is greater than that for S.

When Cl, F and S are plotted against one another (*Fig 6.3*) there is a clear correlation in all cases. F and S show a positive correlation and F and Cl show a negative correlation, as do Cl and S. A positive linear correlation between the volatile species shows that they display similar behaviour, as shown by the F and S relationship.

S is usually not found in high concentrations in felsic magmas, so the trend shown in *Fig 5.17a* is likely a saturation curve (Zajacz et al. 2012) showing the removal of S during formation of sulphide pockets (*Fig 5.3*), which is supported by the relationship between FeO (the only sulphide that was measured) and S (*Fig 6.4*). As the S increases, so does the FeO, suggesting that the melt was saturated with Fe-sulphides and thus crystallised them.

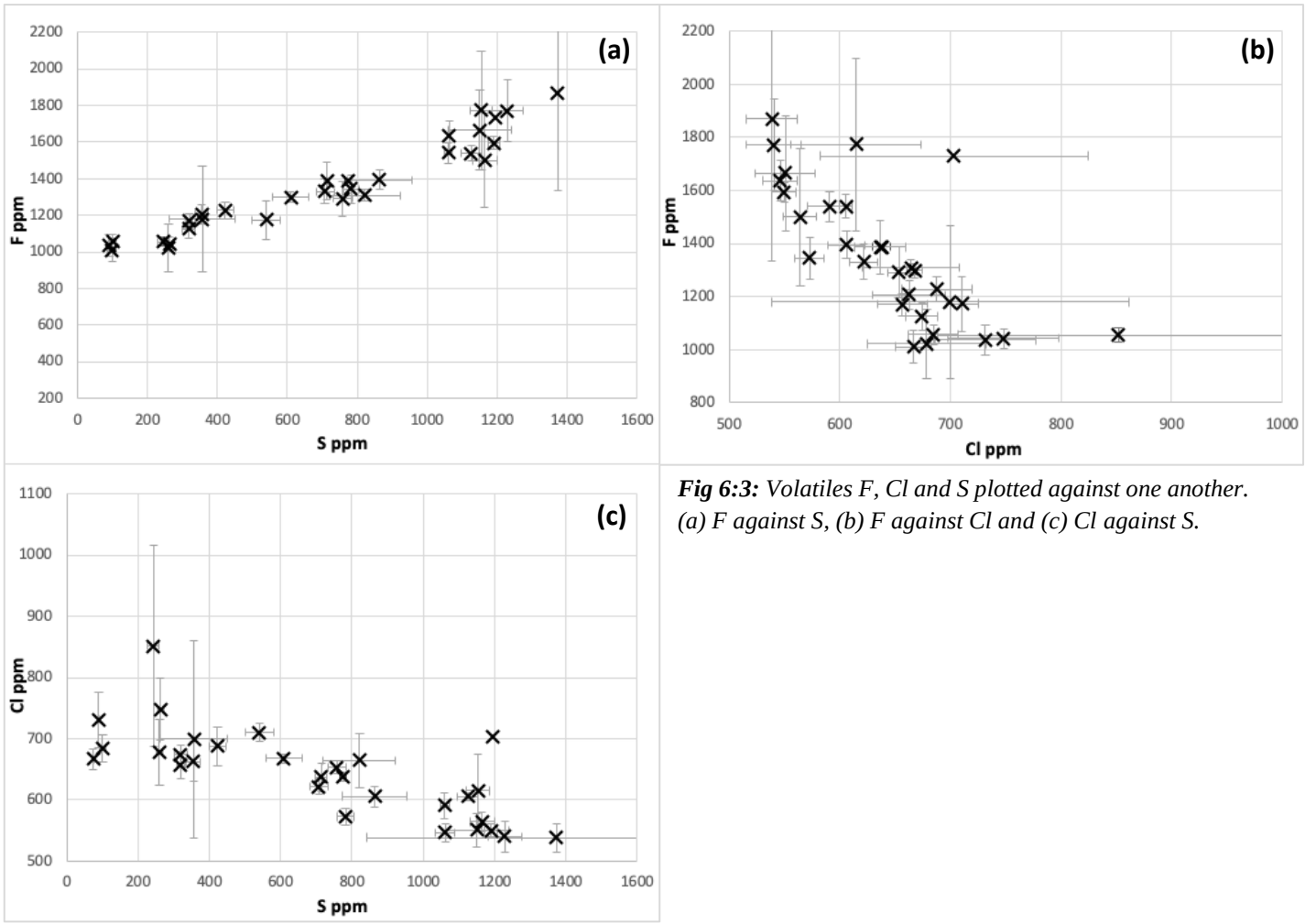

Fig 6:3: *Volatiles F, Cl and S plotted against one another. (a) F against S, (b) F against Cl and (c) Cl against S.*

The negative relationship between F and SiO_2 is interesting, because F is highly soluble and thus should not degas significantly (Balcone-Boissard et al. 2010). Therefore the magma needs to be quite shallow in the crust (~2 km) to allow F to degas (Balcone-Boissard et al. 2010). F also has a tendency to adsorb onto surfaces of salts that are formed and then dissolve into the aqueous phase, which may also explain the negative correlation with SiO_2 (Wardell et al. 2008).

The positive relationship between Cl and SiO_2 is to be expected, because Cl behaves incompatibly. However, Cl is not solely controlled by degassing processes because of the weakly inverse relationship between pressure and solubility (Metrich & Rutherford 1992). This means that it is not easily removed from the melt by degassing until the melt is shallow (~2 km) (Baker & Balcone-Boissard 2009). An alternative theory for the enrichment in Cl at high SiO_2 content is that the magma body is partially melting the surrounding crust that is rich in Cl because of the high degree of hydrothermal alteration in the Krafla region (Westrich et al. 1988, Schipper et al. 2019).

Based on the depth that the KJ-39 melt was intersected (2571 m) it is possible that the melt was shallow enough for F to degas. However, Cl is less soluble in silicate magmas than F so if F is degassing, Cl should be as well and thus you would expect to see a positive correlation in *Fig 6.3b* (Westrich et al. 1988). It is possible, that the Cl is degassing but is being overprinted by another process that is enriching the magma in Cl, such as partial melting of a rock rich in Cl. As discussed above, S could also be being removed from the melt by the formation of sulphides so it is possible that degassing of volatiles is not a major process in the KJ-39 melt.

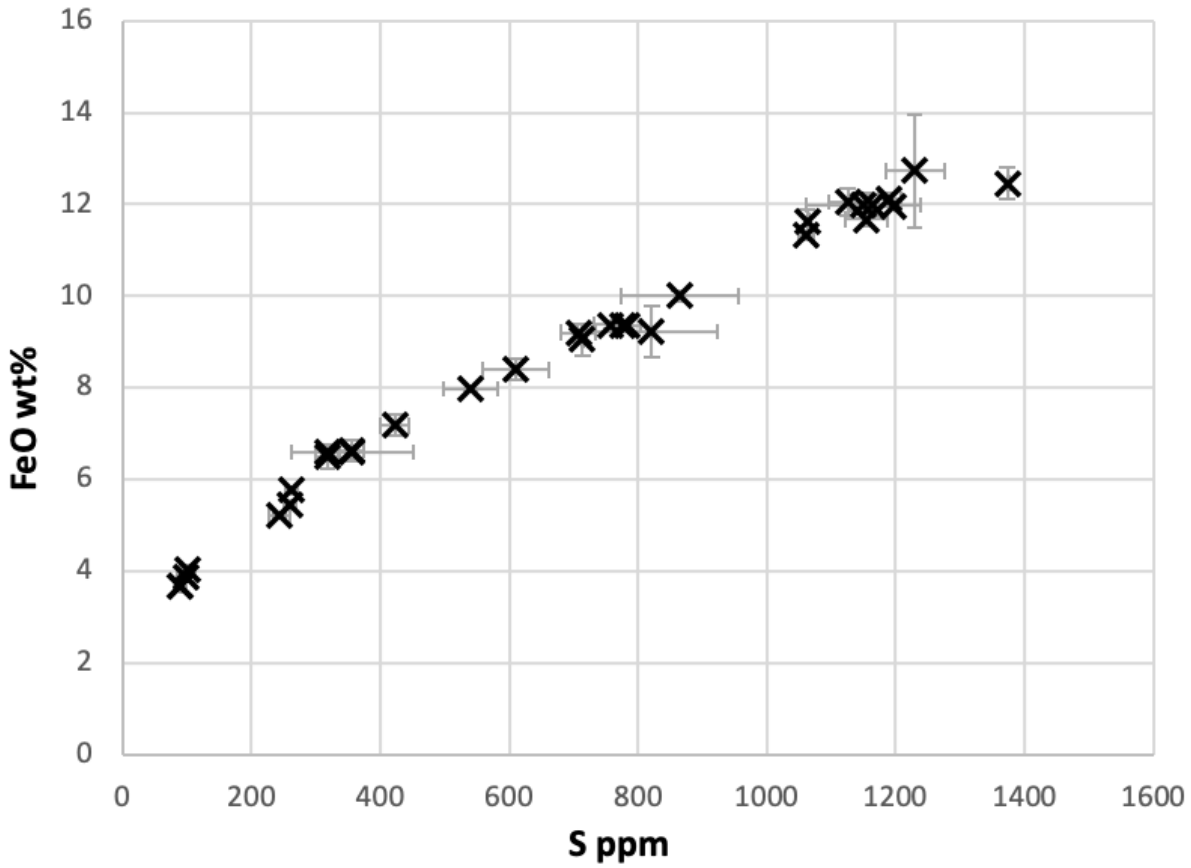

Fig 6.4: *Variation diagram showing the relationship between S and FeO.*

The patterns shown by S, F and Cl presented above cannot be explained by degassing or simple crystallisation processes. Instead, it is suggested that these trends are produced by re-melting of a mafic-intermediate rock with high S and F and low Cl, and a more evolved felsic rock with low S and F and high Cl.

6.2.3 Temperature estimation

6.2.3.1 Quenching temperature

Quenching temperatures for the glass chips were estimated using the speciation model of Nowak & Behrens (2001) by finding the quenching temperature that 'best fit' the speciation measured in the chips and areas of chips unaffected by hydration. The best fit was obtained using a temperature of 550 °C and shown in *Fig 5.12.*

6.2.3.2 Crystallisation temperature

Pyroxene crystallisation temperatures were estimated using the two-pyroxene thermometer developed by Purtika (2008) (*Section 4.5*) on the two pyroxene crystals hosting exsolution lamellae. The hosts in both cases were augite, and the lamellae were pigeonite and ferrosilite. The thermometer calculated temperatures 1083 and 967 °C, respectively (average 1025 °C) with uncertainties approximately ±60 °C (Purtika 2008).

Using the above modelled temperatures, the pyroxenes in the KJ-39 sample crystallised at approximately 1000 °C, suggesting that they formed deeper in the crust and cooled as the melt rose upwards. The magma body then cooled to a temperature of 550 °C when it pooled in the shallow crust, where it was quenched by the drilling fluid.

6.2.4 Pressure estimation

Using the model developed by Papale et al. (2006), it is possible to obtain H_2O saturation pressures for the melt that formed the glass. The model requires the H_2O_t content, CO_2 content and major element composition of the glass. It then calculates the partitioning of H_2O between the silicate melt and another phase (gas/fluid) based on the percentage of H_2O and CO_2 in the magma, by applying thermodynamic equilibrium between the liquid and gaseous volatile constituents.

H_2O saturation pressures calculated using the model of Papale et al. (2006) are lower than the hydrostatic pressure at their depth of collection (2571 metres below the surface), with one chip plotting above (*Fig 6.5a*). Because the cuttings were stuck at the base of the well after the magma was intersected, it is impossible to differentiate the depths of intersection of individual chips, hence the use of 2571 m for all of the glass. Lithostatic pressure values were also obtained using a depth of 2571 m; minimum and maximum lithostatic pressures were calculated using the minimum (2266 g/L) and maximum (2737 g/L) densities calculated for

the KJ-39 glass based on their major element composition (*Section 4.4.3.3*). All of the samples plotted below the minimum lithostatic pressure. Owing to problems with the FTIR analyses (*Section 5.4.4*) useable CO_2 data were only obtained for seven of the KJ-39 chips. This means that for the rest of chips, (without CO_2 detected) the saturation pressures were calculated using an average from the seven chips that data was measured, 21 ppm.

Several solubility models exist for H_2O and CO_2. Zierenberg et al., (2013) used VolatileCalc (Newman & Lowenstern, 2002) to estimate the H_2O-CO_2 saturation pressures of the rhyolitic IDDP-1 glass. In order to permit direct comparison VolatileCalc was also used to provide a second set of pressure calculations (*Fig 6.5*). It is recognised that VolatileCalc is calibrated for rhyolitic, or basaltic compositions, with no option for calculating pressures for intermediate compositions, such as those found in this study. As a result all calculations for the KJ-39 glass were conducted assuming a rhyolitic composition. Calculations were also conducted at 600 °C, although the speciation in the KJ-39 glass suggests a quench temperature of 550 °C, as this is the minimum temperature that VolatileCalc accepts.

Despite these limitations, the saturation pressures calculated using VolatileCalc, show a very similar trend (*Fig 6.5b*) to those calculated using the Papale et al. (2006) model, with all but one chip plotting below the hydrostatic pressure. Minimal variations between the two pressure sets indicates that the choice of model is not a major issue.

Irrespective of whether the model of Papale et al. (2006) or VolatileCalc (Newman & Lowenstern 2002) is used, almost all the glass chips analysed from KJ-39 appear to be under-saturated for the depth of collection. The reason for this could be because CO_2 contents used in the calculation could be lower than the concentration actually in the chips, but in order for the samples to plot above the hydrostatic pressure the CO_2 content would need to be between 180 and 325 ppm. CO_2 this high would produce peaks with absorbances greater than 0.12 in chips with the thickness of those analysed. This would have been very clear on the spectra, and was not observed. Thus, even though some CO_2 may have been present below detection, which may raise the saturation pressures slightly, this would not raise them enough to exceed even hydrostatic pressures.

Alternatively, the chips could be under-saturated because the melt from which they formed did not contain enough volatiles to reach saturation. However, the vesicular nature of the chips

suggests they were oversaturated with volatiles causing degassing, making it most likely that degassing was promoted by a sharp drop in pressure, caused by intersection of the melt during drilling. For pressures to be as low as calculated for the KJ-39 sample, they would have to have been exposed to surface atmospheric pressures. However, the well was circulated with drilling water during drilling so this is not likely. Further work is required to determine the reason for the low pressures.

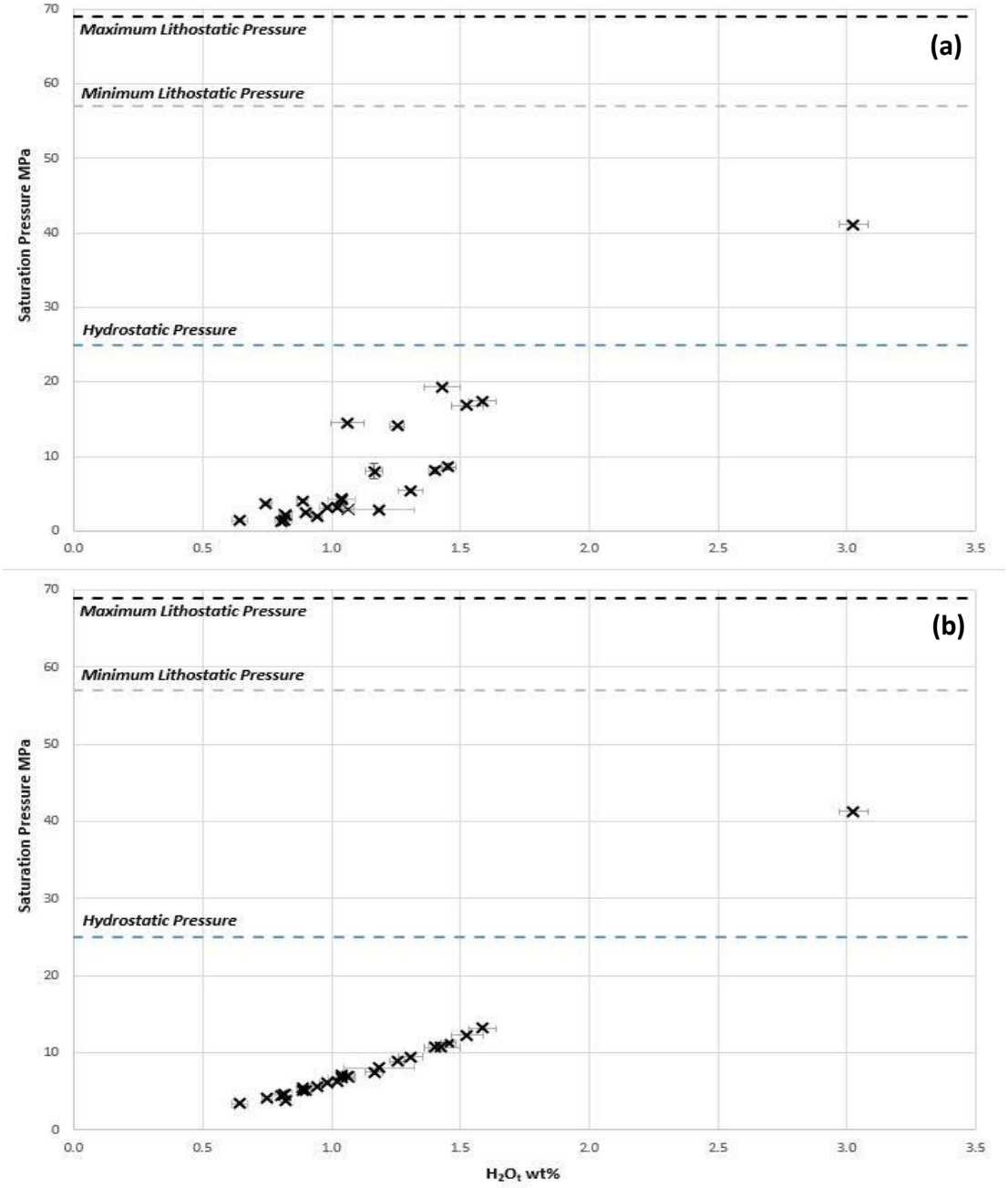

Fig 6.5: *H_2O_t content plotted against saturation pressure for the KJ-39 sample, (a) calculated using Papale et al. (2006) and (b) calculated using VolatileCalc (Newman & Lowenstern 2002). Blue dotted line represents the hydrostatic pressure and grey dotted lines represent minimum and maximum lithostatic pressures calculated using a depth of 2571 m, the depth below surface that the KJ-39 sample was collected from and densities of 2266 and 2737 g/L respectively. Error bars show standard deviation.*

6.3 Mineral assemblage

The mineral assemblage that was retrieved along with the glass consists of plagioclase feldspar, primarily bytownite with some anorthite, and pyroxene, present as augite, pigeonite and ortho-pyroxene. As well as the crystals, there were also some pockets of opaques, identified as iron-copper-sulphides. Using the textures and the composition of the minerals it is possible to determine whether the minerals were crystallised from the melt or if they were entrained from surrounding country rock.

6.3.1 Mineral textures and shape

6.3.1.1 Zoning

The plagioclase crystals show zoning that is visible in the BSE images (*Fig 5.19*), with zones 1-10 µm wide and variations in An of approximately 1-10%, consistent with oscillatory zoning (Pearce & Kolisnik 1990). This type of zoning is indicative of near-equilibrium, diffusion controlled growth driven by minor fluctuations in the immediate area around the growing crystal and suggests slow cooling rates (Pearce & Kolisnik 1990). This slow cooling indicates that the crystals nucleated at depth and were then brought shallow enough to be intersected by the KJ-39 well.

6.3.1.2 Exsolution lamellae

Pyroxenes in the KJ-39 sample have exsolution lamellae (*Fig 6.6*) of pigeonite or ortho-pyroxene in augite which are indicative of slow cooling (Deer et al. 1998).

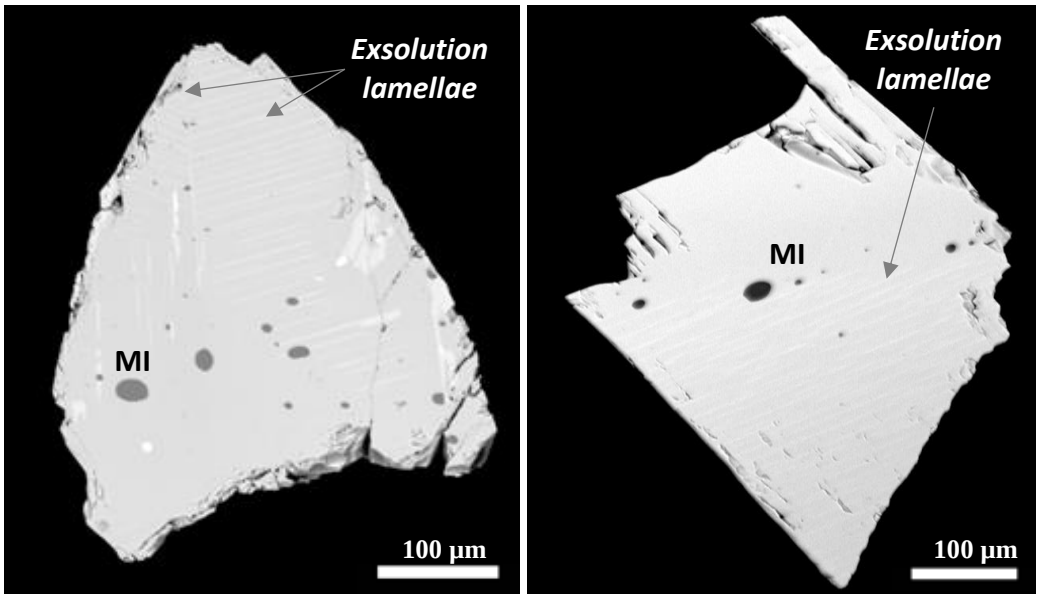

Fig 6.6: *BSE images of two pyroxene crystals from KJ-39 showing exsolution lamellae and melt inclusions (MI).*

As the crystal cools, it re-equilibrates in the solid state into the two end members. If the cooling is too rapid the crystal does not have time to re-organise into the two different structures (Deer et al. 1998). The lamellae (*Fig 6.6*) are approximately 10 µm wide and in some cases occur in more than one orientation. The presence of exsolution lamellae also suggests that these crystals have nucleated at depth and slowly cooled.

6.3.1.3 Shape

Some of the minerals that were retrieved from the KJ-39 well are euhedral, but most show anhedral shapes, particularly those found in the glass. The anhedral habit of the plagioclase and pyroxene crystals associated with the glass suggests resorption of these minerals (*Fig 6.7*). This evidence of resorption indicates partial melting of the crystals once they have crystallised.

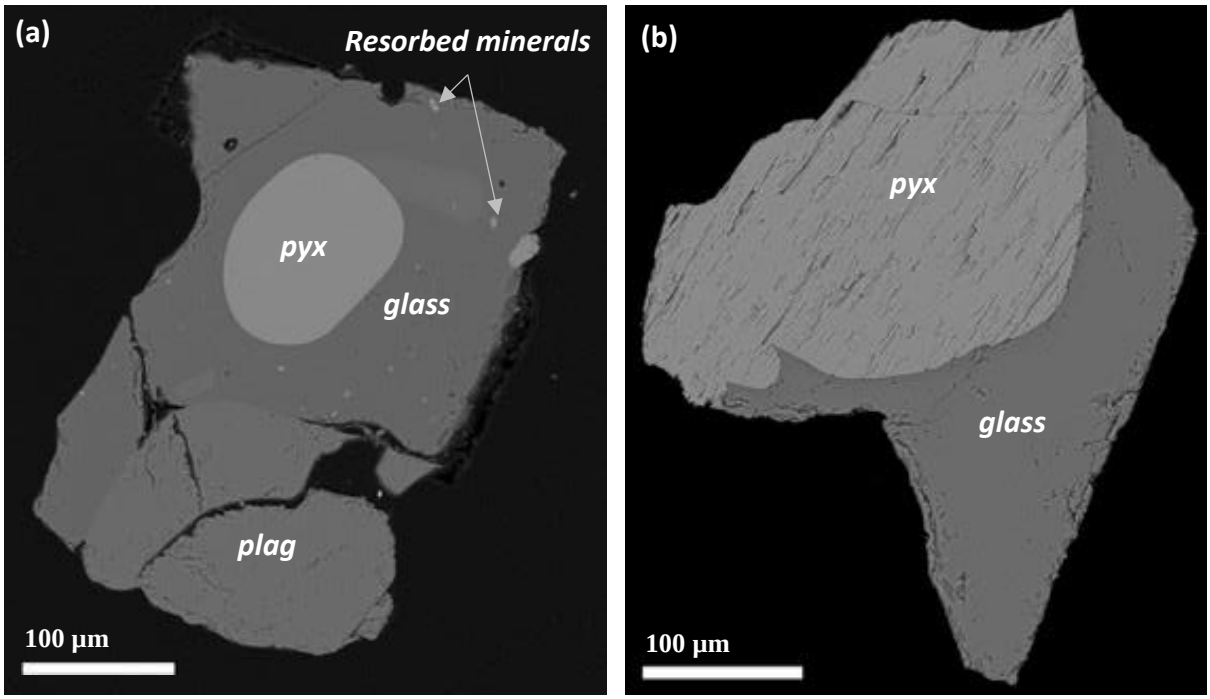

Fig 6.7*: Glass chips with resorbed crystals of pyroxene and plagioclase. (a) Plagioclase (plag) and pyroxene (pyx) crystals showing evidence of resorption, as well as some micron-scale resorbed minerals. (b) Resorbed pyroxene in glass chip.*

The melt must therefore be hot enough to partially melt these crystals, but not hot enough to completely remelt them (Perugini & Poli 2012). This is the case with the crystals from KJ-39, with some crystals only showing partial resorption (*Fig 6.7*) and suggesting either that the melt they were crystallising from mixed with hotter magma or that the source rock containing these crystals was partially re-melted.

6.3.1.4 Microlites

There are multiple glass chips that contain microlites, micron scale crystals, as shown in *Fig 6.8*. The presence of these microlites indicates slightly slower cooling rates than glass without microlites, which cool extremely quickly (Ross 1962). They are most common in mafic to intermediate compositions because the lower viscosity of the melt allows the microlites to nucleate more readily (Ross 1962). *Fig 6.8* shows a glass chip that is andesitic in composition (59 wt% SiO_2) with microlites radiating from the edge of the plagioclase into the glass. Other glass chips also showed possible microlites but they are more randomly distributed throughout the glass (*Fig 6.7a*). The glass in *Fig 6.7a* is much more rhyolitic in composition (74.4 wt% SiO_2) and the more rounded shape of the microlites suggests that they could be remnants of resorbed crystals rather than microlites nucleated during cooling.

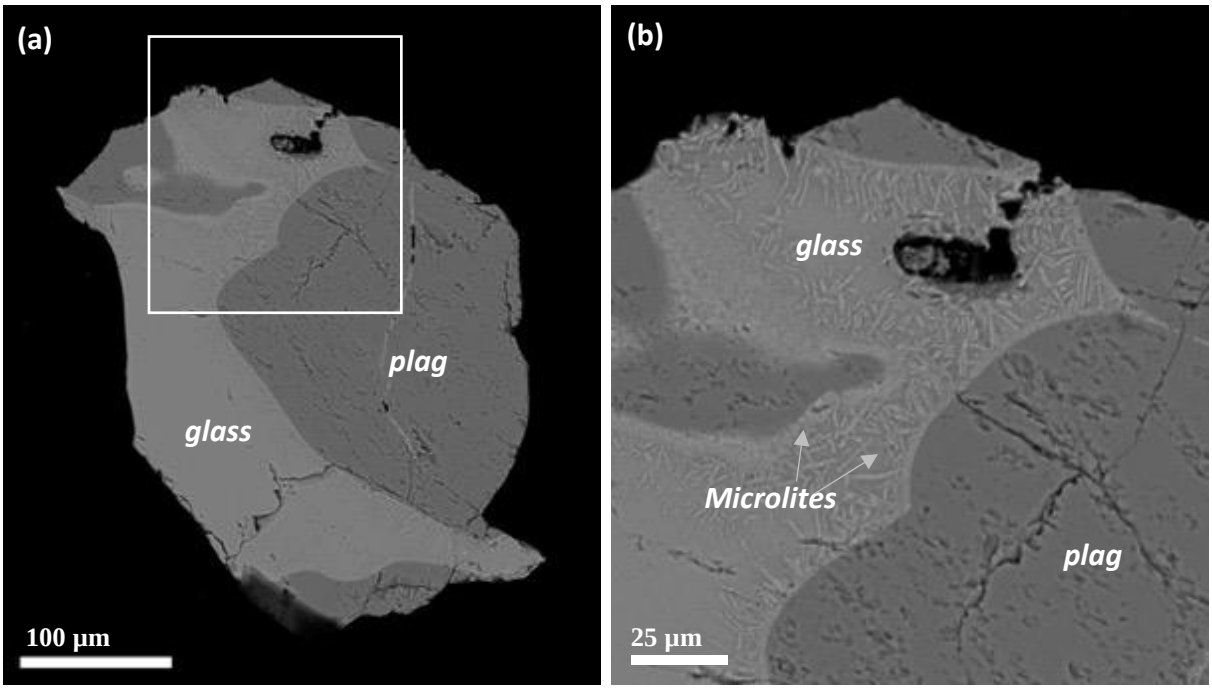

Fig 6.8: *BSE images showing microlites found in plagioclase and glass from the KJ-39 sample set. (a) Microlitic texture in glass with white box representing image shown in (b) to show the microlites in more detail.*

6.3.2 Mineral and glass composition

The above mineral textures suggest partial melting, and the major element data of the glass shows evidence of this re-melting as well, with strong negative relationships between SiO_2 and MgO, FeO, TiO_2, and CaO (*Fig 5.8*). When Na_2O is plotted with K_2O (*Fig 6.9a*) there is a positive trend, although there is a lot of scatter. This indicates that the K_2O is becoming saturated in the melt, because of partial melting of pyroxene, which would also cause an

increase in Na_2O. The K_2O content decreases steadily with increasing CaO content (*Fig 6.9b*) also suggesting the K_2O is being added to the melt during melting of pyroxene. Alternatively, these trends could be explained by crystallisation, which would produce similar trends.

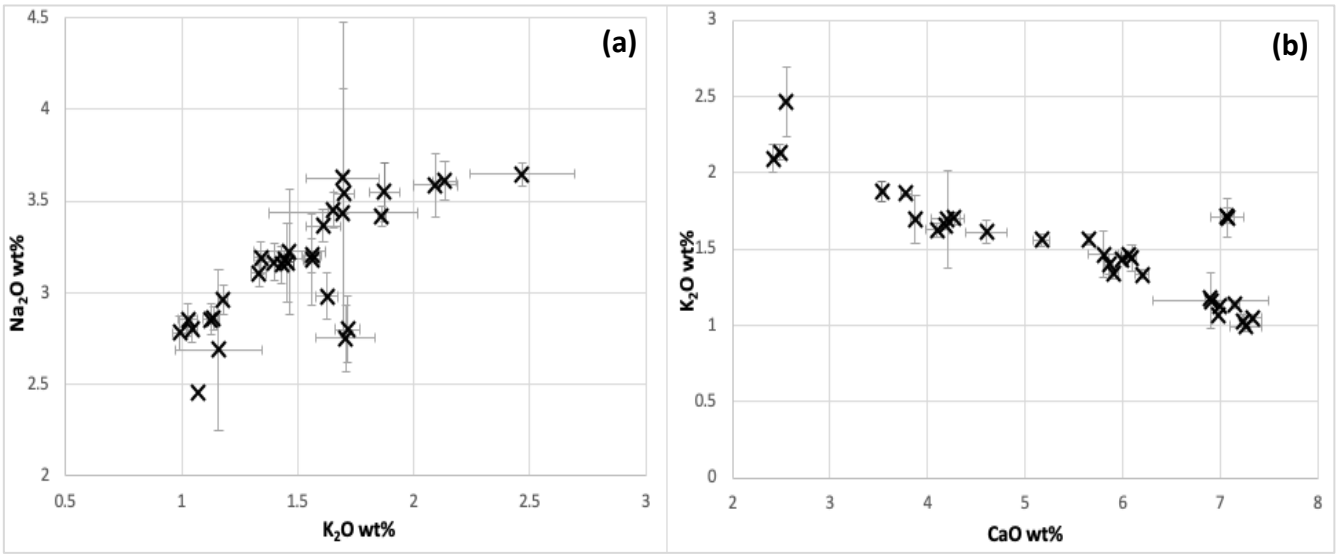

Fig 6.9: *Variation diagrams for KJ-39 glass. (a) Na_2O plotted against K_2O and (b) K_2O plotted against CaO. Concentrations normalised to 100% on an anhydrous basis. Error bars show standard deviation.*

Analysis of the crystal compositions, particularly the An content of the plagioclase crystals, can indicate the origin of the crystals. *Fig 6.10* shows that most of the crystals analysed have $An_{75\text{-}90}$ with only a few plagioclase crystals with An numbers <70 or >90.

When the An contents of plagioclase phenocrysts within glass chips are compared with the SiO_2 content of the surrounding glass, there is a slight correlation, with slightly higher An content in the crystals surrounded by lower SiO_2 glass (*Fig 6.11*). There is one glass chip with low SiO_2 (59 wt%) and low An content (75.6 %) that does not fit the trend (circled). The plagioclase crystals that were separate from the glass are not plotted on *Fig 6.11* because the SiO_2 content of the glass that they crystallised from is not known.

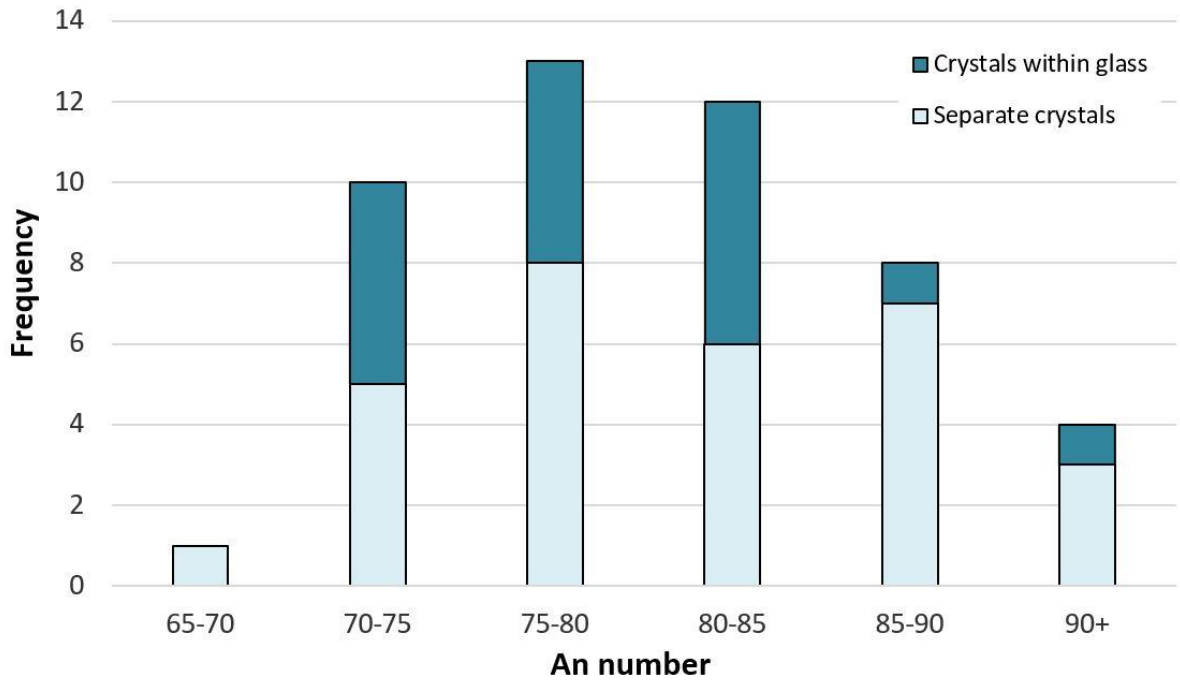

***Fig 6.10**: Histogram showing the frequency of plagioclase An contents in separate crystals and crystals within glass chips.*

CaO content has the strongest control on the An content of plagioclase because anorthite is the calcium end member of plagioclase. There is an inverse relationship between SiO_2 and CaO, with higher CaO content in less evolved magmas *(Fig 5.8f)* (Panjasawatwong et al. 1995).

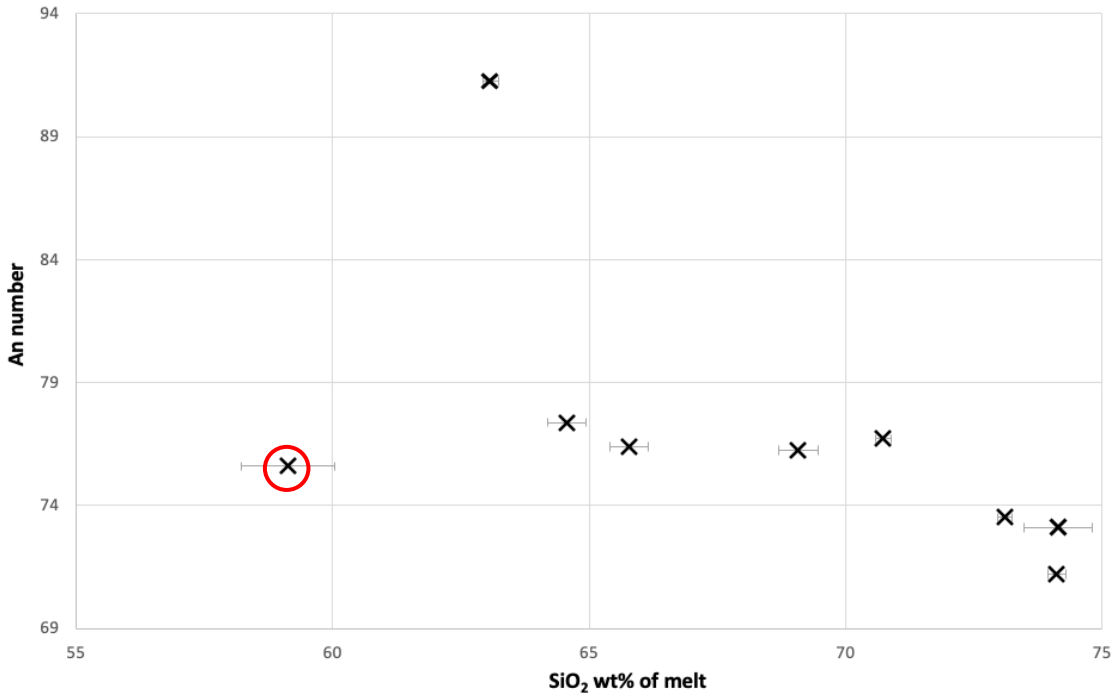

***Fig 6.11:** An content of plagioclase crystals plotted against the SiO_2 content (wt%) of the surrounding glass. Anomalous sample is circled in red. Error bars show standard deviation.*

Therefore, the plagioclase crystals with the highest An content (>90) are likely crystallised from the least evolved magma, and as the An content drops, the SiO_2 content of the melt increases. However, An content also increases with increasing H_2O content (Sisson & Grove 1993) and decreases with increasing pressure (Fram & Longhi 1992). Based on this information it is likely that the plagioclase crystals are not in equilibrium with the high-SiO_2 melt and were crystallised from a more mafic melt. The evidence of partial melting suggests that they were re-melted and entrained into the KJ-39 melt.

6.4 Response to drilling

Because of the high temperatures at the base of the well, and the glass chips that were retrieved at the surface, it is inferred that the well intersected magma (Mortensen et al. 2010). However, it is unclear whether the magma was still liquid when it fragmented. Some glass chips show dense outer surfaces and more vesicular centres (*Fig 6.12*). Similar textures have been observed in subglacially erupted pillow lavas in Iceland, where the core of a pillow can be up to 40% more vesicular than the rim. Höskuldsson et al. (2006) suggest that this reflects emplacement and partial cooling of the pillow in a subglacial meltwater lake, before sudden draining of the lake in a jökulhlaup causes rapid decompression and vesiculation of the still molten pillow core. Although pillow lavas are much larger than the glass chips in this study, a similar mechanism, where the dense chip exterior had quenched at higher pressures, followed by rapid decompression caused by intersection by the drill, vesiculation, and then quenching of the centre of the chip, could be invoked to explain these chip textures (*Fig. 6.12*).

Evidence of fragmentation while the magma is liquid is further supported by the vesicles having two shapes, elongated and spherical (*Fig 5.19*). The elongated vesicles are often infilled by the opaque iron sulphides. The elongated nature of these vesicles indicates that they formed, and then were elongated, by shearing of the magma body, or formed during a shearing event and then when the melt became oversaturated with these iron rich sulphide fluids they precipitated in these voids. In order for these vesicles to become filled with fluids there must have been some small scale fractures throughout the magma body to allow for the fluid flow. The more spherical vesicles have not undergone shearing and are not filled with opaque iron sulphides, suggesting they formed post-shearing and post-fluid movement, or, they are not interconnected and thus did not allow fluids to pass through. It is likely therefore, that these spherical vesicles formed once the magma was intersected by the drill. With no subsequent

deformation of the magma between vesicle formation and quenching, the vesicles remained circular.

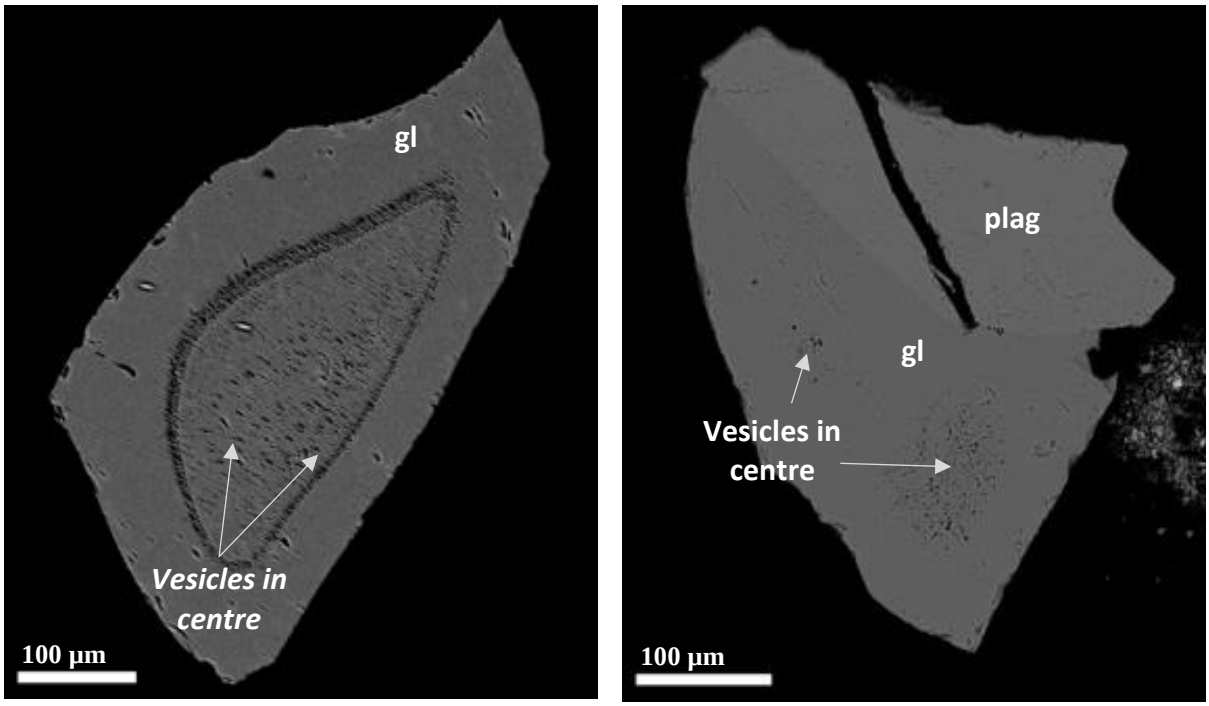

Fig 6.12: *BSE images of two glass chips from KJ-39 showing vesicles concentrated in the centre of the chips. gl = glass, plag = plagioclase.*

As discussed above (*Section 6.2.2.1*) the results of the volatile analysis indicate that the water in the samples is primarily magmatic, although there are six chips that were identified as hydrated and ten that were partially hydrated. This hydration is likely 'secondary hydration' caused by the interaction of the glass with the drilling fluid while the cuttings were stuck at the base of the well.

Based on the above information, I infer that the magma body was liquid when it was intersected, and fragmented in association with the drilling, causing very rapid quenching of the outer surfaces and degassing, followed by quenching of the vesiculated centre of the fragments. Although the samples were at the base of the well for a week, and during this time in almost continuous contact with the drilling water, only a few of the chips have absorbed the drilling water and appear hydrated. However, as there is not a set of cuttings recovered over a recorded time interval for KJ-39, like there is for the IDDP-1 drilling (Watson 2018, Saubin et al. In Review), it is impossible to identify whether there was a temporal change in the chemistry and texture of the cuttings as the melt was intersected by the drilling, and whether the magma was drawn up the well after intersection.

6.5 Origin of KJ-39 magma

The key findings from the KJ-39 data set are as follows;

- Glass compositions range from andesitic to rhyolitic.
- H_2O_t contents range from 0.64 – 3.02 wt% (unhydrated).
- There is evidence for molten magma being intersected by drilling.
- Plagioclase and pyroxene phenocrysts are not in equilibrium with the melt.
- There is textural evidence for crystals having re-melted.

Using the results presented in Chapter 5 and the evidence for magmatic processes above, the formation of the KJ-39 magma may be primarily the result of re-melting. Although crystallisation could also explain the wide range of glass compositions and trends in the KJ-39 sample, crystallisation would not produce the partial melting textures. There is evidence for partial melting in the phenocryst assemblage found within the glass, suggesting that either the melt crystallising these phenocrysts mixed with a hotter melt, or that there was partial melting of crystals from the surrounding crust. The crystal data (*Section 6.3.2*) shows that the phenocrysts crystallised from a melt with a mafic composition and that they cooled slowly (based on the presence of zoning and exsolution lamellae). This suggests that this more mafic melt from which the phenocrysts crystallised was formed deeper in the crust. These crystals could have been entrained from the surrounding, more mafic crust, during partial melting. The hotter melt is confirmed by the geothermometry of the pyroxene lamellae, producing temperatures of approximately 1000 °C.

The more felsic component of the glass can also be explained by re-melting. The previous study by Mortensen et al. (2010) analysed the major element chemistry of the glass from well KJ-39 and presented evidence for formation of a high-SiO_2 rhyolite by partial melting of hydrated basalt during the early stages of contact metamorphism. The key piece of evidence for this is the high abundance of corundum (4-5 wt%) (Droop et al. 2003). Because this felsic melt is more buoyant, it rises through the crust and can pool in the shallow crust where it is accessible by drilling (Árnason 2020).

Based on the evidence for partial melting in the mineral assemblage, and the wide range of compositions in the KJ-39 sample I suggest that the KJ-39 melt could have formed from the re-melting of a hydrated basalt to form the high-SiO_2 rhyolite and re-melting of a more mafic

(intermediate) rock, in the immediate vicinity of a basaltic intrusion. The homogeneous compositions of individual chips indicates that mixing is not a major process occurring in the KJ-39 melt, however, as shown in *Fig 6.13*, there may be a zone between the rhyolitic and andesitic melt, where there is minor mixing to produce the complete range of compositions displayed in this study. Mortensen et al. (2010) speculate that the heat source that generated the melts could have been from the Hólseldar Fires, which occurred 2500 years ago. However, because of the proximity of the KJ-39 well to the Krafla magma chamber, the source of the heat could also be a basaltic intrusion associated with more recent eruptions at Krafla (Mortensen et al. 2010). Individual pockets of magma caused by melting by the intrusion were then intersected by the KJ-39 drill bit causing the melts to get 'sucked up' the well and quenched by the drilling fluid. A summary of the formation mechanism is presented in *Fig 6.13*.

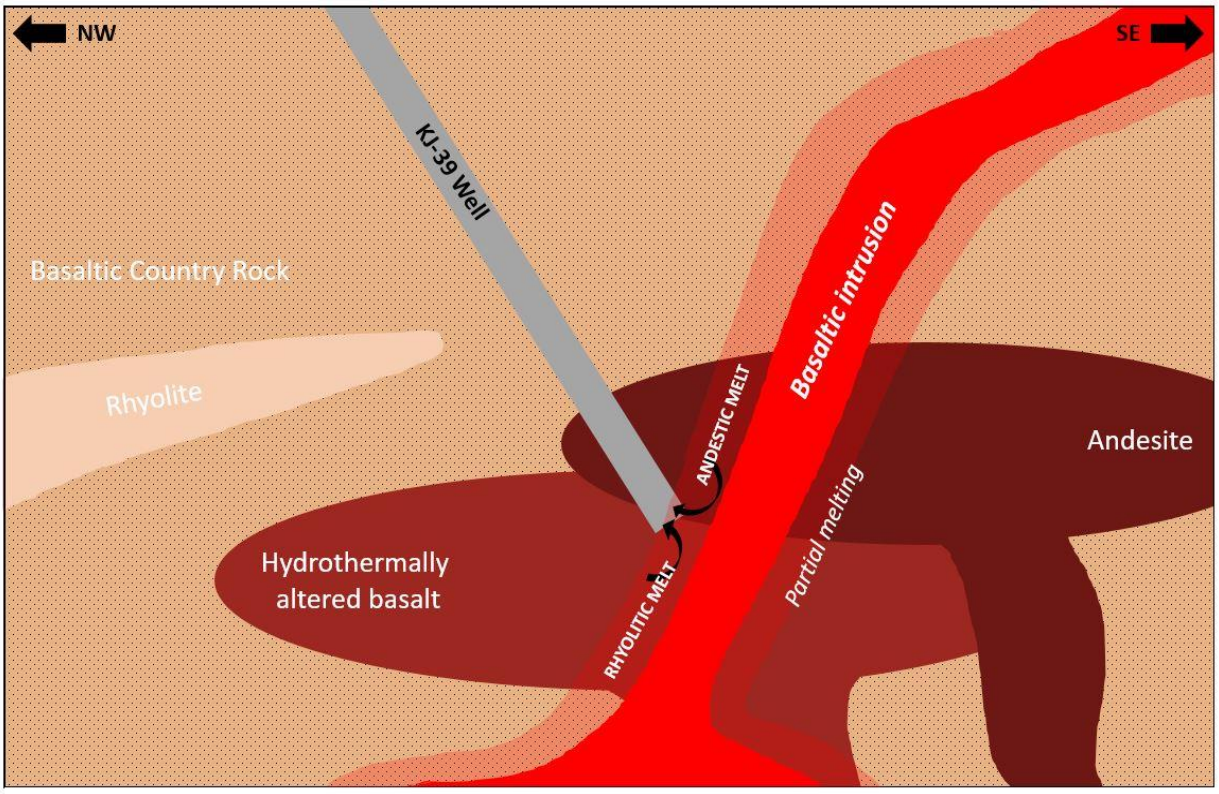

Fig 6.13: *Schematic model for the formation of the KJ-39 melt. Heating of surrounding hydrothermally altered basalt to form rhyolitic melt and andesite to form andesitic melt by a basaltic intrusion. Not to scale. Size and shape of intrusions and rock masses not constrained.*

6.6 Comparison with the IDDP-1 magma

The relationship between the KJ-39 magma and the IDDP-1 magma is important to investigate because it will help to constrain the geometry of the wider Krafla geothermal region. This will provide an insight into the best places for geothermal drilling in the area and could have economic implications. The two wells are located approximately 2.5 km apart (*Fig 6.14*) and hit magma at depths of 2571 m and 2103 m (Zierenberg et al. 2013) respectively, so could conceivably have hit the same magma body. The IDDP-1 magma has been thoroughly studied because it was one of the first occasions that magma had been directly encountered and provided unprecedented opportunities to study the magma without the effects of degassing, cooling or eruption (Zierenberg et al. 2013).

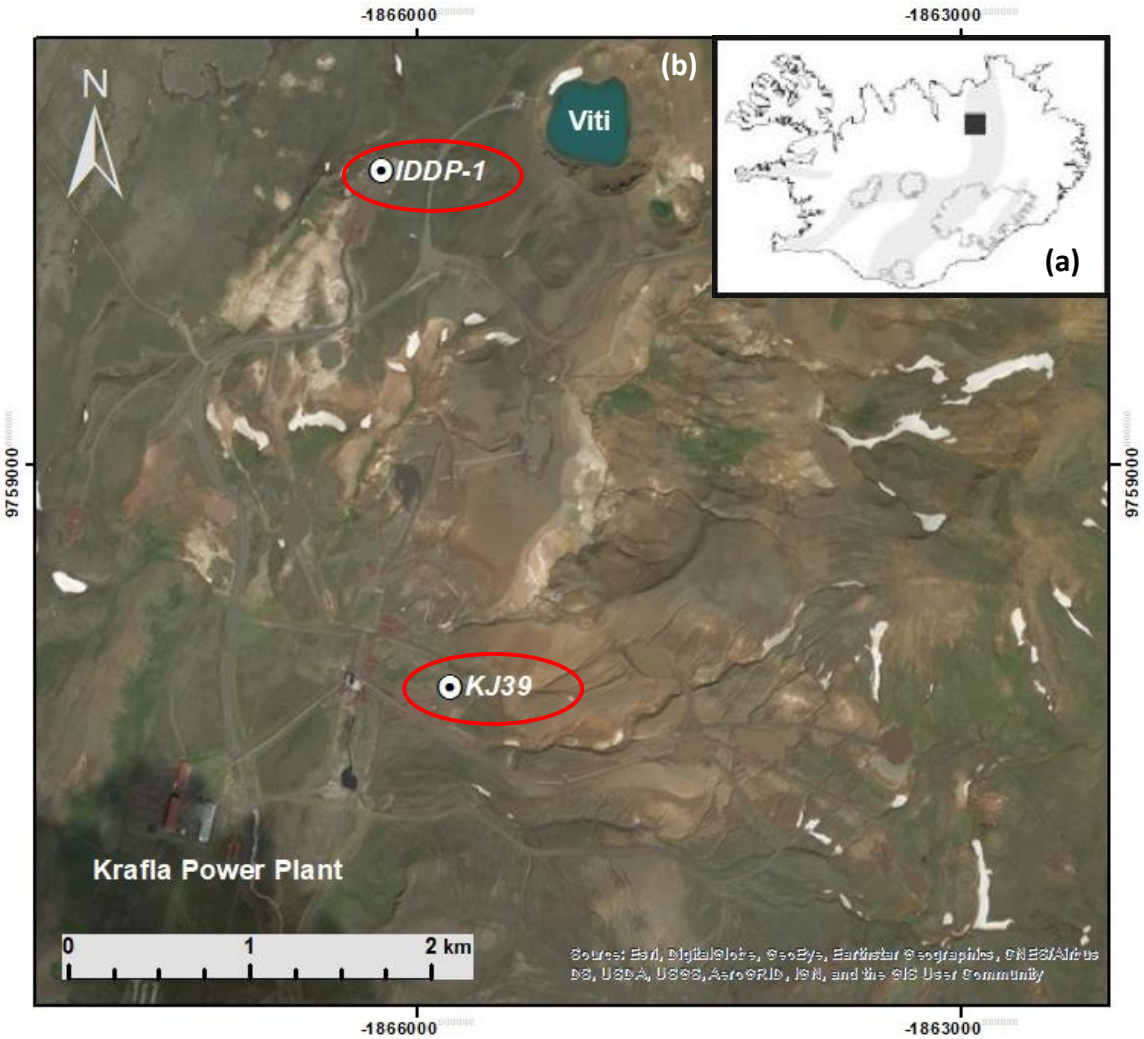

Fig 6.14: *(a) Location of Krafla in Iceland. (b) Location of well holes KJ-39 and IDDP-1 (circled) in relation to the Krafla Power Plant and Viti Crater (labelled). Basemap imagery is from ESRI through ArcMap.*

6.6.1 Origin of IDDP-1 magma

The origin of the IDDP-1 melt is considered to be the result of partial melting of hydrothermally altered basalt at depth (e.g. Zierenberg et al. 2013, Masotta et al. 2018). The multiple batches of melt that were identified by Zierenberg et al. (2013) and Watson (2018) represent the host felsite (Melt-1), the evolved partially melted basalt (Melt-2) and the result of mixing between the two melts (Melt-3).

6.6.2 Major element data

When plotted on the TAS diagram along with the KJ-39 data obtained from this study, it is clear to see that the IDDP-1 glass chips have a much narrower range of SiO_2 (75.9-77.9 wt%) and higher total alkali contents (6.7-8.9 wt%) than the KJ-39 glass chips (58.2-74.5 wt% and 3.5-6.1 wt%, respectively) (*Fig 6.15*).

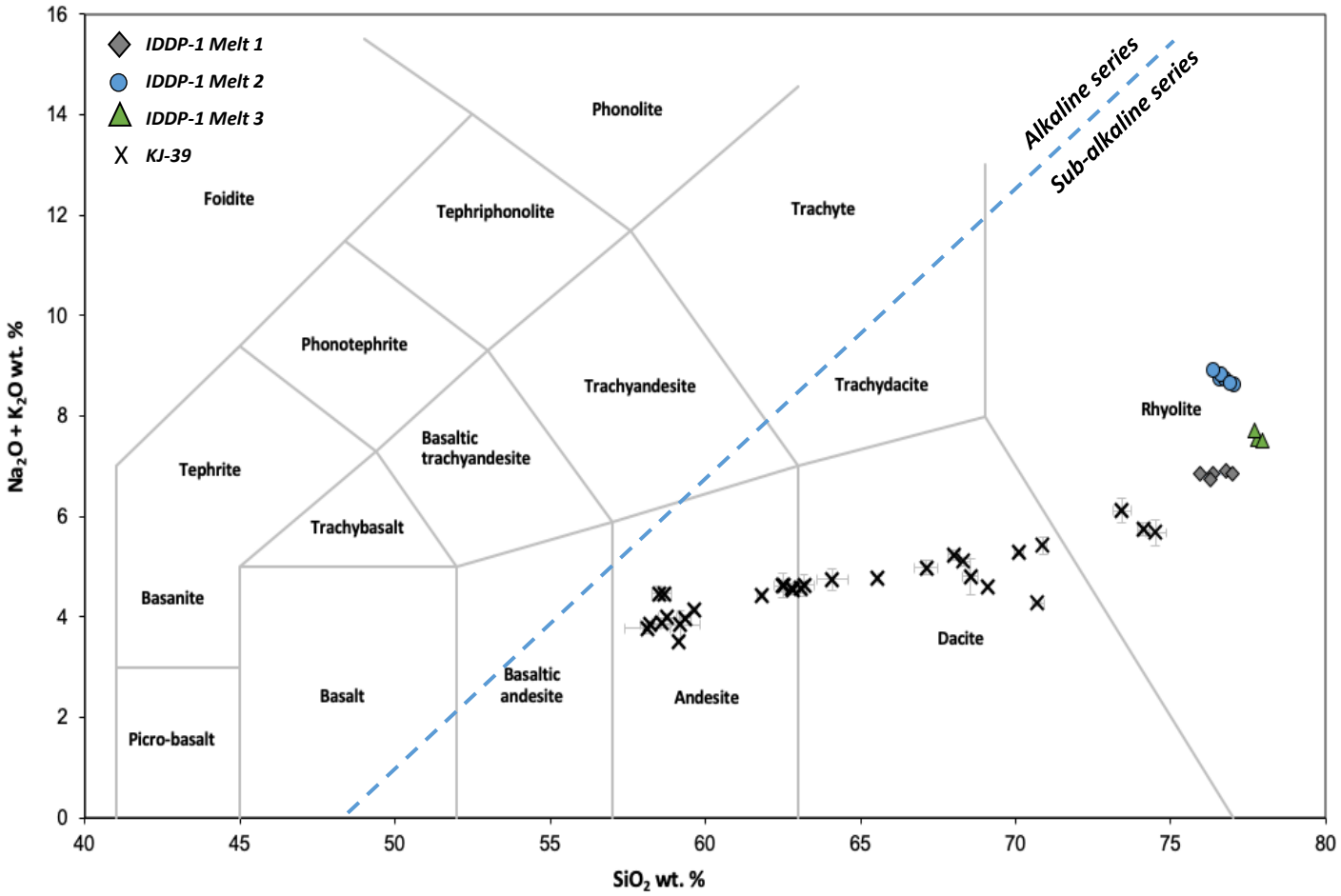

Fig 6.15: *Total-Alkali-Silica (TAS) diagram from Le Bas & Streckeisen (1986) showing the KJ-39 glass chips (black crosses) compared to the IDDP-1 glass, divided into the melt batches from Zierenberg et al. (2013): grey diamonds show Melt-1, blue circles show Melt-2, green triangles show Melt-3. Concentrations normalised to 100% on an anhydrous basis. Error bars show standard deviation.*

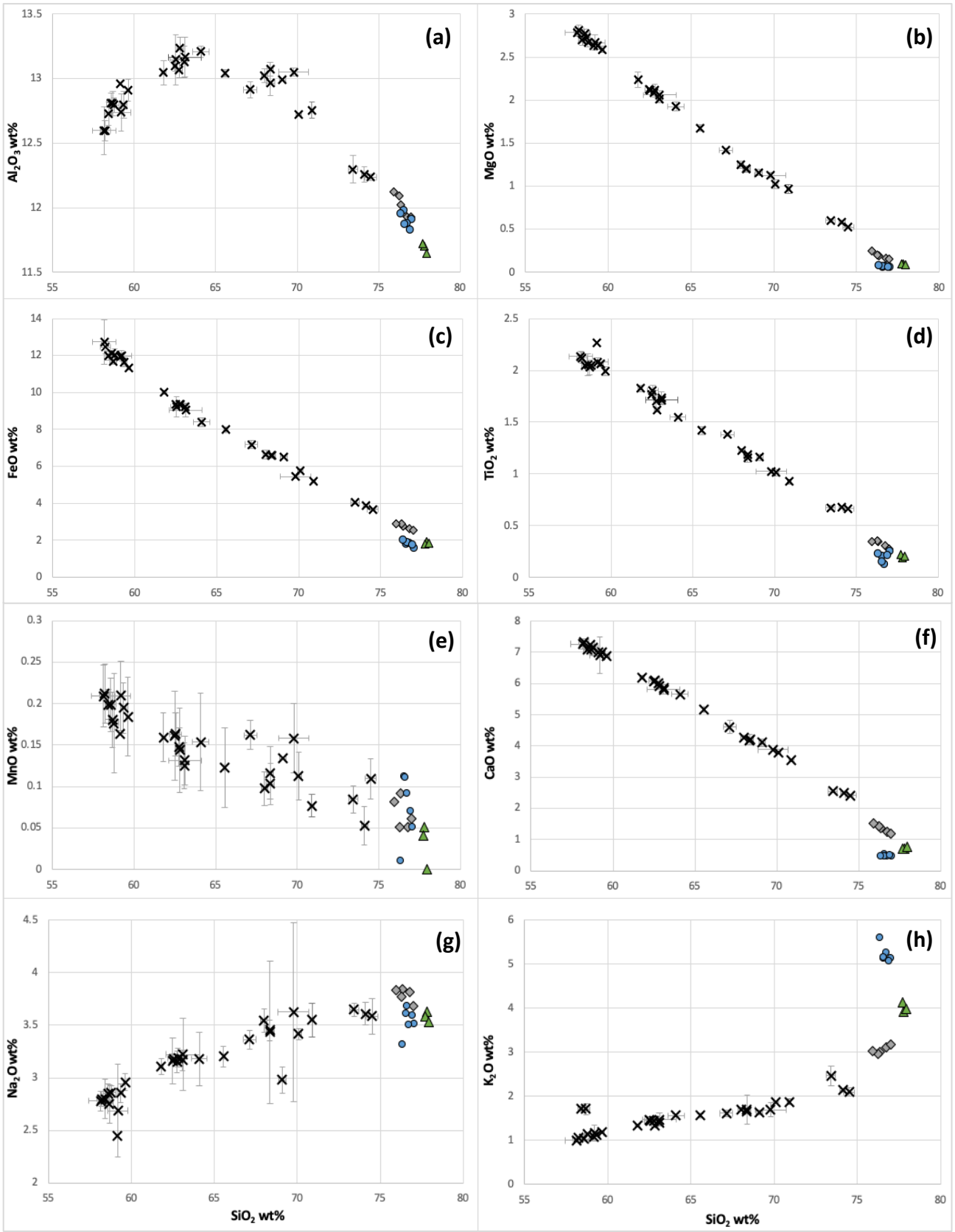

Fig 6.16: *SiO_2 variation diagrams comparing KJ-39 and IDDP-1 (from Zierenberg et al., 2013) glass data. Concentrations normalised to 100% on an anhydrous basis. Error bars show standard deviation. Symbols as in Fig 6.15.*

SiO_2 variation diagrams (Harker diagrams) show that the IDDP-1 data fall on the trends defined by the KJ-39 data, particularly for Al_2O_3, MgO, TiO_2, CaO, MnO and FeO data (*Fig. 6.16a-f*). Na_2O contents of the IDDP-1 glass chips are similar to the highest values measured in the KJ-39 glass chips (*Fig 6.16g*). When the K_2O data are plotted against SiO_2 it is clear that the K_2O contents of the IDDP-1 Melt-2 and Melt-3 glass chips are significantly higher than those of the KJ-39 chips, and are the cause of the higher total alkali content (*Fig 6.16h*). This suggests that there was a more potassic source for the IDDP-1 melt. Melt-1 are the most similar IDDP-1 compositions to the KJ-39 glass based on the major element chemistry.

CIPW norms were calculated for the KJ-39 glass in order to compare with those calculated by Zierenberg et al. (2013) for the IDDP-1 glass. The results are plotted on the quartz-plagioclase-orthoclase ternary diagram (*Fig 6.17*). This shows that the KJ-39 glass have predominantely plagioclase dominated CIPW norms with quartz <40% and orthoclase <30%, and all of the IDDP-1 melts plot separately. Melt-1 and Melt-2 from IDDP-1 have higher K_2O, as shown in *Fig 6.16h*, thus would crystallise more orthoclase from the melt. Melt-1 is the most similar to the KJ-39 glass chips, suggesting that these two melts would crystallise a similar mineral assemblage.

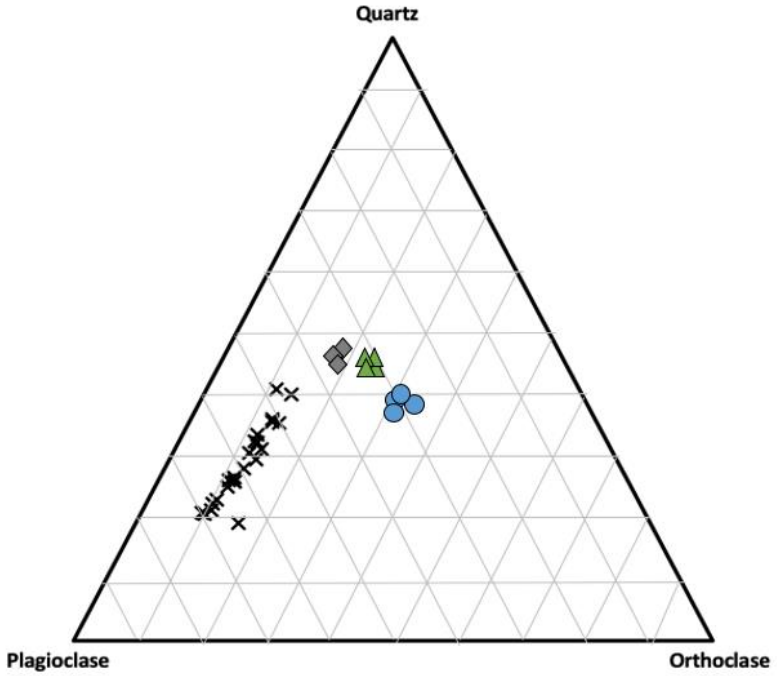

Fig 6.17: *CIPW normative compositions of KJ-39 glass compared to the IDDP-1 glass (from Zierenberg et al., 2013), calculated using the worksheet by Hollacher (2004). Ternary plot plotted using the TernPlot Excel package (Marshall 1996). Symbols as in Fig. 6.15.*

6.6.3 Volatile contents

Average H_2O_t contents of the IDDP-1 and KJ-39 glass are 1.75 and 1.16 wt% respectively, and the ranges are 1.40-2.15 wt% for IDDP-1 (Zierenberg et al. 2013, Watson 2018) and 0.63-3.02 wt% for KJ-39. The majority of of IDDP-1 samples and all KJ-39 glasses have higher OH than mH_2O, with a few chips from IDDP-1 set showing the inverse, suggesting that this water is primarily magmatic. The ratio of OH/mH_2O ranges from 0.97-2.63 for the IDDP-1 samples, with the lowest ratio representing that of the samples with higher mH_2O. For the KJ-39 data set the ratio ranges from 1.24-4.65. *Fig 6.18* presents both IDDP-1 and KJ-39 OH/mH_2O ratios plotted against H_2O_t and both samples show a close correlation with the Nowak & Behrens (2001) model at 550 °C. The model at 843 °C was also plotted because this is the upper end of the rhyolite speciation model (Nowak & Behrens 2001). There is one chip in the KJ-39 sample section that plots above both the 550 °C and 843 °C models.

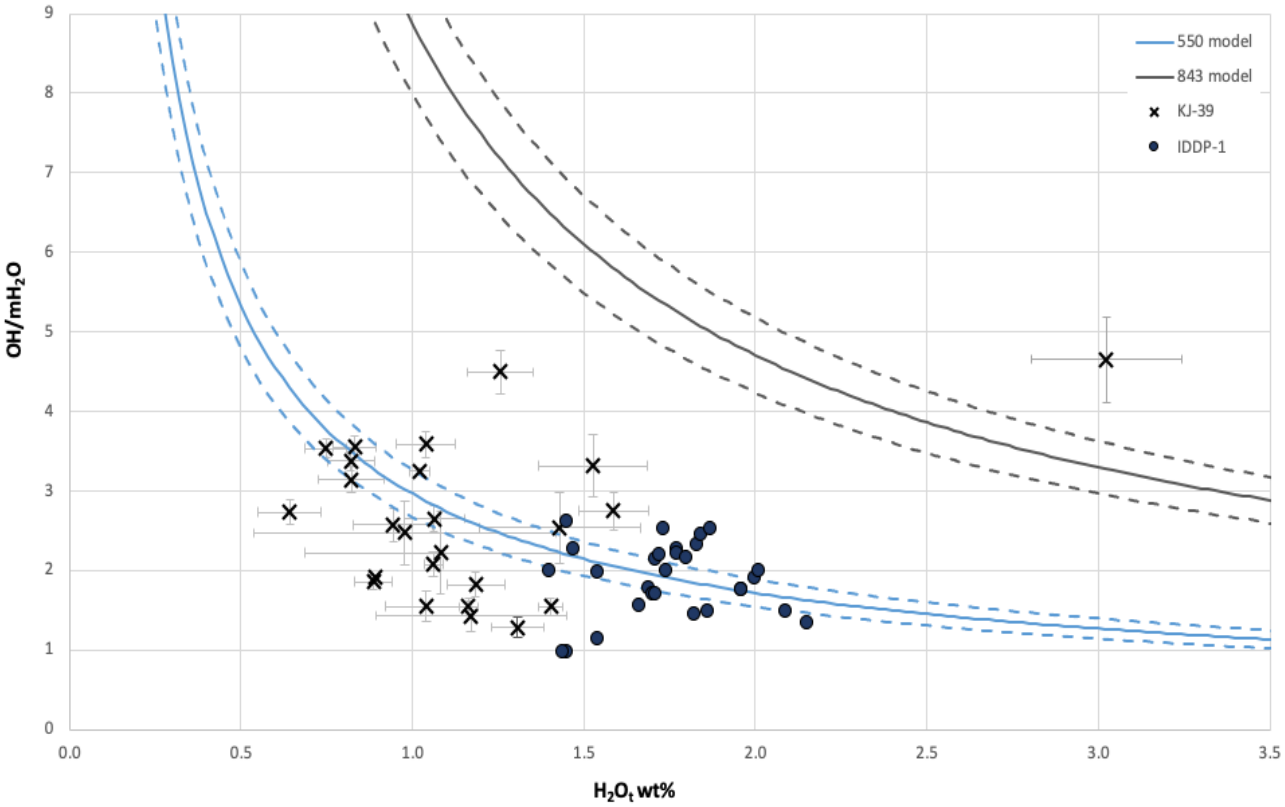

Fig 6.18: *Plot of OH/mH_2O against total H_2O for KJ-39 glass (black crosses) and IDDP-1 glass (blue circles). Error bars show the standard deviation of each individual chip. The blue line represents the modelled speciation at a temperature of 550 °C and the grey line represents the modelled speciation at a temperature of 843 °C from Nowak & Behrens (2001). Dotted lines represent +10% and – 10% of the models.*

CO_2 data was only measureable in seven of the KJ-39 glass chips and ranged from 5 to 40 ppm and the CO_2 contents of the IDDP-1 data range from 58 to 278 ppm (Watson 2018).

6.6.4 Temperature and pressure estimates

6.6.4.1 Temperature comparisons

An average quench temperature of 550 °C was calculated for the KJ-39 magma based on H_2O speciation, and crystallisation temperatures based on the two-pyroxene thermometer (Purtika 2008) were approximately 1000 °C. The quench temperatures for the IDDP-1 sample, when calculated by Watson (2018) ranged from 500 to 625 °C (Nowak & Behrens 2001) and crystallisation temperature estimated by Zierenberg et al. (2013) for the IDDP-1 magma range from 758 to 939 °C based on the pyroxene thermometer QUILF (Anderson et al. 1993). The temperature estimations for the two magma bodies, KJ-39 and IDDP-1, are therefore quite similar. As the IDDP-1 samples were collected over a 9-hour time interval (Saubin et al. 2017), changes in quench temperatures could be calculated based on the time of recovery (Watson 2018), but such data do not exist for the KJ-39 well.

6.6.4.2 Pressure comparisons

Saturation pressures calculated for the KJ-39 samples using VolatileCalc (Newman & Lowenstern 2002) at 600 °C range from 3 to 41 MPa (*Fig 6.5*). The saturation pressures for the IDDP-1 samples, also calculated using VolatileCalc (Newman & Lowenstern 2002) but at 900 °C (based on crystallisation temperature), range from 30 to 50 MPa (Watson 2018).

Hydrostatic pressures for each sample set differ because the two wells intersected the magma bodies at different depths, IDDP-1 was shallower, at a depth of 2101 m. The lithostatic pressure for the KJ-39 sample set was calculated using the maximum density value of 2737 g/L, while the IDDP-1 density value used that of rhyolite 2350 g/L (Stevenson et al. 1994). Almost all of the KJ-39 glass chips appear under-saturated for the depth of collection, with one sample falling above this threshold (*Fig 6.5*). The IDDP-1 samples all fall above hydrostatic pressure (16 MPa) (Watson 2018) (*Fig 6.19*). The differences in the saturation pressures for the two sample sets are because the KJ-39 glass chips contain less volatiles, predominantly CO_2, than the IDDP-1 samples. This suggests that when the magma bodies were intersected by the drilling, the melt in KJ-39 was under less pressure than that in IDDP-1. This is supported by the fact that the magma intercepted by IDDP-1 rose up the well somewhat, likely driven by the overpressure in the magma body (Watson 2018). It is not known, however, whether the magma encountered by KJ-39 also rose up the well after interception.

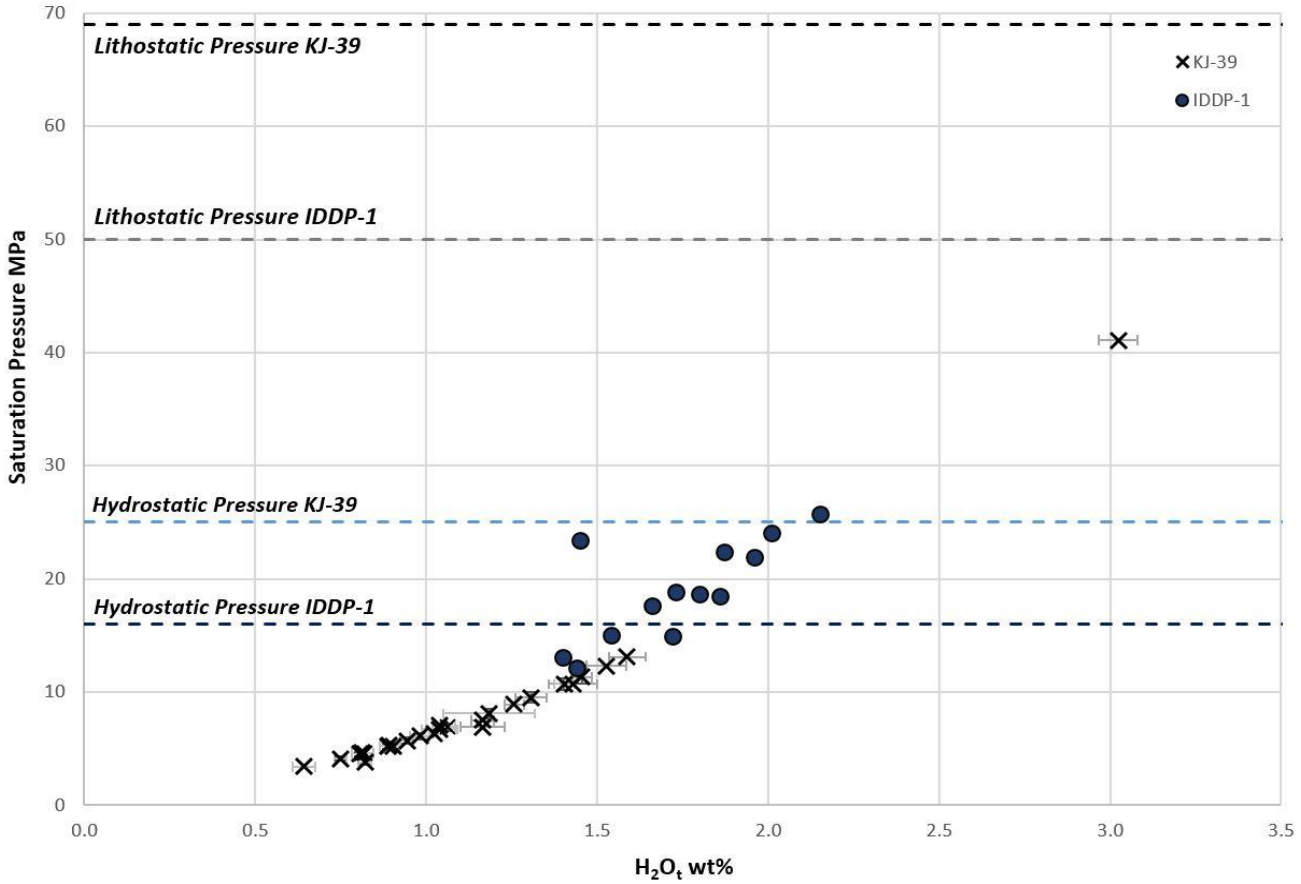

Fig 6.19: *H_2O_t content plotted against saturation pressure calculated using VolatileCalc (Newman & Lowenstern 2002) for KJ-39 (black crosses) and IDDP-1 (blue circles) samples. Blue dotted line represents the hydrostatic pressure and grey dotted lines represent lithostatic pressures. Error bars show standard deviation.*

6.7 Relationship of the KJ-39 and IDDP-1 magma sources

Using the results obtained as part of this study and the data from the literature, a comparison was made to determine the relationship between the two magma sources. The proximity of the two wells and their location in relation to the Krafla magma chamber (*Fig 2.2*) means that the magma intercepted by both the IDDP-1 and KJ-39 wells could be derived from the same heat source. However, the KJ-39 well was drilled directionally to the east, away from the IDDP-1 well and also hit the magma 500 m deeper than IDDP-1.

As shown by in *Fig 6.16,* the IDDP-1 data sits at the high-SiO_2 end of the major element data of KJ-39, with Melt-1, which represents the host felsite, being the most similar. The two magma bodies, KJ-39 and IDDP-1 were both, in part, formed by partial melting of a hydrated basalt to form high-SiO_2 rhyolites (Mortensen et al. 2010, Zierenberg et al. 2013). The model for the genesis of KJ-39 indicates that the heat source that caused this melting, a basaltic intrusion,

also caused the melting of a more mafic rock, such as an andesite. When the well intersected the peripheries of the basaltic intrusion the rhyolite melt and andesitic melt, along with a zone where the two are mixed, were drawn up the well and quenched.

The model for the IDDP-1 melt is quite similar; it is also considered to be formed by partial melting of hydrothermally altered basalt. The heat from this intrusion partially melted the surrounding crust and the two melts mixed (Zierenberg et al. 2013). Silicic rocks formed by this mechanism are also found elsewhere in the Krafla region, including xenoliths from the 1875 Askja eruption (Sigurdsson & Sparks 1981, MacDonald et al. 1987).

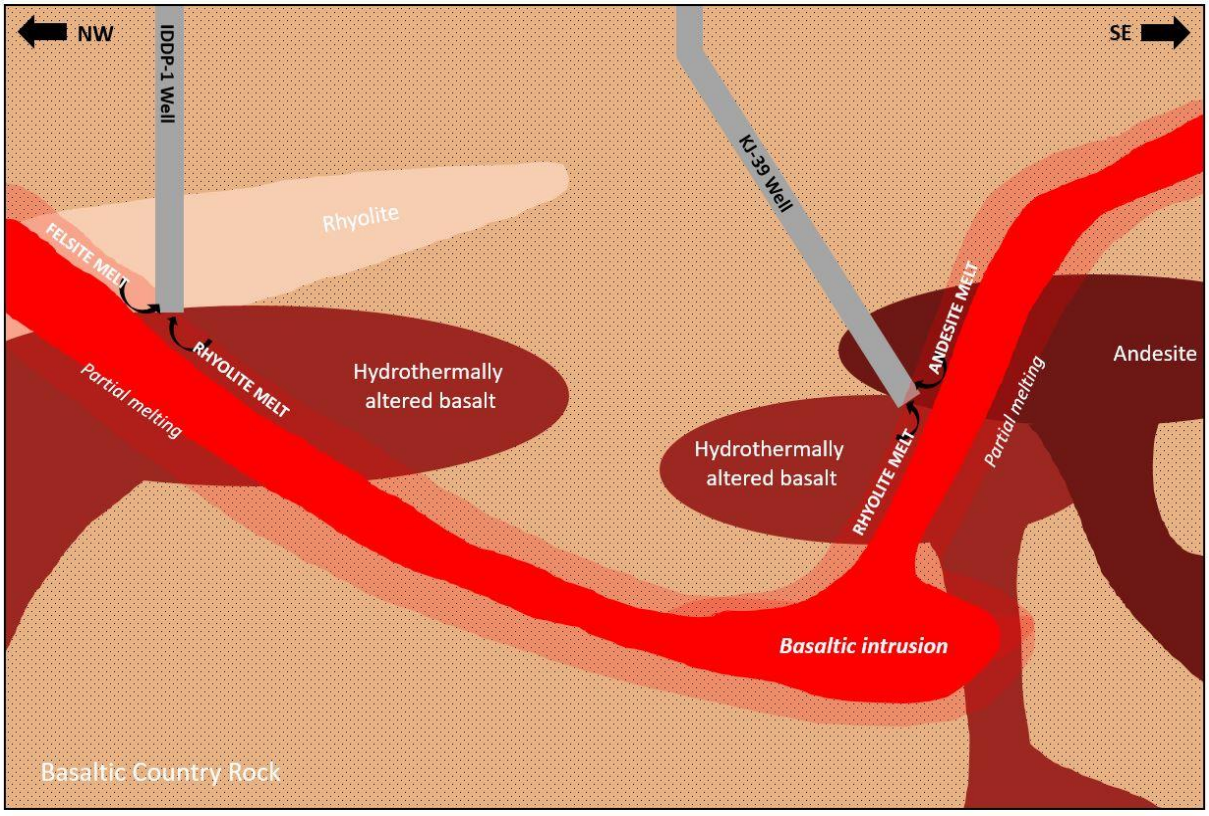

Fig 6.20: *Schematic model for the formation of the KJ-39 and IDDP-1 melts. Heating of surrounding hydrothermally altered basalt to form rhyolitic melt and andesite to form andesitic melt. Source of heat for both melts could be the same basaltic intrusion. Not to scale. Size and shape of intrusions and rock masses not constrained.*

Because of the close proximity of the two wells it is possible that the heat source that caused the melting of the surrounding crust could be the same basaltic intrusion (*Fig 6.20*). Therefore, although the two melts intersected during drilling are not from the same exact magma source, the mechanisms that formed the high-SiO_2 components are probably the same as well as the heat source.

7 Conclusions

This study presents the results of the geochemical and textural analysis of the KJ-39 sample of glass chips that was retrieved when the geothermal well intersected magma at a depth of 2865 m (2571 m below surface) and examines the relationship between the KJ-39 and IDDP-1 melts. Both of these wells intersected magma during geothermal drilling, with KJ-39 intersecting it at a depth of 2571 m and IDDP-1 a depth of 2105 m. The two wells are 2.5 km apart, with KJ-39 drilled directionally to the east away from the IDDP-1 well, and both are located close to the Krafla magma chamber.

The geochemistry and petrology of the KJ-39 glass chips indicate that the melt that was intersected by the KJ-39 well was formed by partial melting of a hydrated basalt to produce a high-SiO_2 melt (Mortensen et al. 2010) and partial melting of a more mafic rock, andesitic in composition. This method of melt formation is similar to that invoked for the melt that was intersected by IDDP-1. The IDDP-1 melt is also thought to have formed by partial melting of a hydrated basalt to produce a rhyolite, which has mixed with the partially melted surrounding felsite country rock (Zierenberg et al. 2013). The much wider range of compositions among the KJ-39 chips is likely due to the melted andesite occurring proximal to the rhyolite and the well intersecting both of these compositions. In order to produce the span of compositions displayed in this study, it is likely that there is a zone of overlap where the two melts are mixed. Because of the differences in the major element chemistry of KJ-39 and IDDP-1, the two melts are not from the same magma body, however, the mechanisms that formed the high-SiO_2 components are probably similar. The proximity of the two wells also suggests that the heat source that caused the melting of the two magma bodies could be the same (*Fig 6.20*).

These findings indicate that this mechanism of producing high-SiO_2 melts, via partially melting hydrated basalt, in basaltic environments like Iceland is much more common than initially considered. The geothermal industry at Krafla targets the peripheries of melt bodies for hydrothermal fluids, so the information from this study will help to improve the knowledge of the sub-surface at Krafla and better inform the most efficient drilling targets and locations. If the intrusion that is causing melting of KJ-39 and IDDP-1 is the same, this could provide more target areas for geothermal drilling in Krafla.

Because of time constraints associated with the project, there were aspects of the samples that were unable to be measured. Further, more in depth analysis of the KJ-39 samples should focus on isotope analysis of the glass chips in order to better constrain the origin of the more mafic melt, as well as trace element analysis. Melt inclusions were also observed in some pyroxene crystals in the KJ-39 sample, which would be interesting to study.

Table 7.1: *Table outlining the main aims of the project along with the conclusions associated with each aim.*

Objective	**Conclusion**
Objective 1: Review the literature on the magmatic context of the Krafla geothermal region and processes that effect melt composition.	Previous studies on KJ-39 and IDDP-1 are presented in ***Chapter 2*** along with the magmatic history of the Krafla region. Magmatic processes are presented in ***Chapter 3***.
Objective 2: Measure major and volatile element variations in the glass chips to examine evidence for magmatic processes such as melt injection, mixing and fractional crystallisation.	Samples were measured for the major and some volatiles (S, Cl and F) using electron probe microanalysis (***Chapter 5***), results suggest evidence of fractional crystallisation or re-melting (***Chapter 6***).
Objective 3: Examine any compositional heterogeneities based on the properties of the glass chips i.e. texture, colour.	No correlation was found between glass chemistry and percentage of vesicles or colour (***Chapter 5***). No correlation between H_2O content and percentage of vesicles found either (***Chapter 6***).
Objective 4: Use FTIR measurements to identify the H_2O and CO_2 concentrations and H_2O speciation in the glass chips.	FTIR measurements were carried out on a total of 44 glass chips to measure H_2O and CO_2. CO_2 contents were often masked by atmospheric contamination but where they could be measured ranged from 5 to 40 ppm and H_2O contents ranged from 0.64 to 3.02 wt% (***Chapter 5***).
Objective 5: Compare glass major and volatile element data as well as mineral assemblages with those from the IDDP-1 magma chips that exist in the literature.	Analysis of data obtained from this study for the KJ-39 samples and IDDP-1 data from the literature identified that the two magma sources are different, with KJ-39 samples showing a wider range of SiO_2 contents and lower alkali contents ($Na_2O + K_2O$) (***Chapter 6***).

Objective 6: Use the comparison to determine the relationship between the two magma bodies that have been intersected and whether they could be from the same or a similar source.	The KJ-39 and IDDP-1 magma bodies, were in part formed by the same mechanism; partial melting of hydrated basalt. The KJ-39 magma shows evidence of melting of an andesite as well, which explains the range of compositions. The IDDP-1 magma is composed of three high SiO_2 rhyolites formed by mixing of the partially melted basalt with the surrounding felsite. The heat source that caused the melting of the two melt bodies is probably the same (***Chapter 6***).

References

Aiuppa A, Baker DR & Webster JD (2009) Halogens in volcanic systems. *Chemical Geology 263*: 1-18

Anderson DL, Lindsley DH & Davidson PM (1993) QUILF: a Pascal program to assess the equilibria among Fe-Mg-Mn-Ti oxides, pyroxenes, olivine and quartz. *Computers and Geosciences 19*: 1333-1350

Ármannsson H & Benjaminsson J (1986) Changes of gas concentrations in Krafla geothermal fluids. *Proceedings of the 5th Symposium on Water-Rock Interaction.* Reykjavik. 13-16

Árnason K (2020) New conceptual model for the Magma-Hydrothermal-Tectonic system of Krafla, NE Iceland. *Geosciences 10* (34)

Baker DR & Balcone-Boissard H (2009) Halogen diffusion in magmatic systems: Our current state of knowledge. *Chemical Geology 263 (1-4)*: 82-88

Baker DR & Moretti R (2011) Modelling the solubility of sulphur in magma: a 50 year old geochemical challenge. *Reviews in Mineralogy & Geochemistry 73 (1)*: 167-213

Ballentyne DW (1970) *A dictionary of named effects and laws in chemistry, physics and mathematics.* Springer Science & Business Media. Dordrecht.

Bartholemew RF, Butler BL, Hoover HL & Wu CK (1980) Infrared spectra of a water containing glass. *Journal of the American Ceramic Society 63* (9-10): 481-485

Balcone-Boissard H, Villemant B & Boudon G (2010) Behaviour of halogens during the degassing of felsic magmas. *Geochemistry Geophysics Geosystems 11* (9): 1525-2027

Björnsson A, Sæmundsson K, Einarsson P, Tryggvason E & Grönvold K (1977) Current Rifting Episode in North Iceland. *Nature 266* (5600): 318-323. https://doi.org/10.1038/266318a0

Björnsson A, Johnsen G, Sigurdsson S, Thorbergsson G & Tryggvason E (1979) Rifting of the Plate Boundary in North Iceland 1975-1978. *Journal of Geophysical Research 84* (NB6): 3029-3038. https://doi.org/10.1029/JB084iB06p03029

Bodvarsson GS, Benson SM, Sigurdsson O, Stefansson V & Eliasson ET (1984) The Krafla Geothermal Field, Iceland 1. Analysis of Well Test Data. *Water Resources Research 20* (10): 1515-1530

Boichu M, Villemant B & Boudon G (2008) A model for episodic degassing of an andesitic magma intrusion. *Journal of Geophysical Research 113*: doi: 10.1029/2007JB005130

Bouguer P (1729) Essai d'optique sur la gradation de la Lumiere. Gauthier-Villars et Cie, Paris (reprinted in 1929 with a Biographic note and a Preface).

Bowen NL (1956) *The evolution of the igneous rocks*. Dover publications, Canada. 60-62

Burnham CW (1975) Water and magmas: a mixing model. *Geochimica et Cosmica Acta 39*: 1077-1084

Calderone GM, Grönvold K & Oskarsson N (1990) The Welded Air-Fall Tuff Layer at Krafla, Northern Iceland - A Composite Eruption Triggered Eruption by Injection of Basaltic Magma. *Journal of Volcanology and Geothermal Research 44* (3-4): 303-314. https://doi.org/10.1016/0377-0273 (90)90024-a

Carroll MR (1994) Solubilities of sulphur, noble gases, nitrogen, chlorine and fluorine in magmas. *Reviews in Mineralogy and Geochemistry 30*: 87-101

Davis BTC & Boyd FR (1966) The join Mg2S2O6-CaMgSi2O6 at 30 kilo bars pressure and its application to pyroxenes from kimberlites. *Journal of Geophysical Research 71 (14)*: 3567-3576

De Campos CP, Perugini D, Ertel-Ingrisch W, Dingwell DB & Poli G (2011) Enhancement of magma mixing efficiency by chaotic dynamics: an experimental study. *Contributions to Mineralogy and Petrology 161*: 863-881

Deer WA, Howie RA & Zussman J (1998) *An introduction to the rock-forming minerals*. 3rd Issue. Mineralogical Society of Great Britain and Ireland. London.

DeGroat-Nelson PJ, Cameron BI, Fink JH & Holloway JR (2001) Hydrogen isotope analysis of rehydrated silicic lavas: implications for eruption mechanisms. *Earth and Planetary Science Letters 185*: 331-341

Della Ventura G, Bellatreccia F, Marcelli A, Guidi MC, Piccinini M, Cavallo A & Piochi M (2010) Application of micro-FTIR imaging in the Earth sciences. *Analytical and Bioanalytical Chemistry 397* (6): 2039-2049. https://doi.org/10.1007/s00216-010-3811-8

Droop GTR, Clemens JD & Dalrymple DJ (2003) Processes and conditions during contact anatexis, melt escape and restite formation: the Huntly Gabbro Complex, NE Scotland. *Journal of Petrology 44 (6)*: 995-1029

Eggler DH (1973) Role of CO2 on the melting processes in the mantle. *Carnegie Institute, Washington. 72*: 457-467

Eichelberger JC (2019) Planning an international magma observatory. *Eos 100*: https://doi.org/10.1029/2019EO125255

Einarsson P (1978) S-wave shadows in the Krafla caldera in NE Iceland, evidence for a magma chamber in the crust. *Bulletin of Volcanology* 41: 1-9

Einarrson P (1991) The Krafla rifting episode 1975-1989. In: Gardarrson A & Einarsson A (eds) Nattura Myvatns (Nature of Lake Myvatn): Reykjavik. *Iceland Nature Science Society*: 97-139

Elders WA, Friðleifsson GO & Saito S (2003) The Iceland Deep Drilling Project: Its global significance. *International Geothermal Conference.* Reykjavik. September 2003.

Elders WA, Friðleifsson GO, Zierenberg RA, Pope EC, Mortensen AK, Guðmundsson A. et al. (2011) Origin of a rhyolite that intruded a geothermal well while drilling at the Krafla volcano, Iceland. *Geology 39* (3): 231-234. https://doi.org/10.1130/g31393.1

Fram MS & Longhi J (1992) Phase equilibria of dikes associated with Proterozoic anorthite complexes. *American Mineralogy 77*: 117-136

Friðleifsson GO & Elders WA (2005) The Iceland Deep Drilling Project: a search for deep unconventional geothermal resources. *Geothermics 34* (3): 269-285. https://doi.org/ 10.1016/j.geothermics.2004.11.004

Friðleifsson GO, Albertsson A & Elders WA (2010) The Iceland Deep Drilling Project (IDDP) 10 years later – Still and opportunity for an international collaboration. *Proceedings World Geothermal Congress*. Bali, Indonesia. April 2010

Friðleifsson GO, Elders WA, Zierenberg RA, Stefansson A, Fowler APG, Weisenberger TB, et al. (2017) The Iceland Deep Drilling Project 4.5km deep well, IDDP-2, in the seawater-recharged Reykjanes geothermal field in SW Iceland has successfully reached its supercritical target. *Scientific Drilling 23*: 1-12. https://doi.org/10.5194/sd-23-1-2017

Friedman I & Long W (1976) Hydration rate of obsidian. *Science 4225* (191): 347-352

Giggenbach WF (1987) Redox processes governing the chemistry of fumerolic gas discharges from White Island, New Zealand. *Applied Geochemistry 2*: 143-161

Giggenbach WF & Sheppard D (1989) Variations in the temperature and chemistry of White Island fumarole discharges 1972-85. *New Zealand Geological Survey Bulletin 103*: 119-126

Grönvold K (1984) Myvatn Fires 1724-1729. Chemical composition of the lava, Reykjavik, Iceland. *Nordic Volcanological Institute, Professional Paper 8401:* 24

Gylfadóttir SS, Kristjánsson V, Egilson Þ, Gudfinnsson GH & Mortensen AK (2012) Discharge testing of the IDDP-1 well in 2010 and 2012. Report ÍSOR-2012/035. Iceland Geosurvey. Reykjavik, Iceland.

Hollacher K (2004) CIPW Norm Calculation Program. Geology Department. Union College.

Hólmgeirsson S, Guðmundsson A, Pálsson B, Bóasson HA, Ingason K, Porhallson S (2010) Drilling operations of the first Iceland Deep Drilling well (IDDP). In: *Proceedings of the World Geothermal Congress*. Bali, Indonesia. 25-29 April 2010. 1-10

Höskuldsson A, Sparks RSJ & Carroll MR (2006) Constraints on the dynamics of subglacial basalt eruptions from geological and geochemical observations at Kverkfjöll, NE Iceland. *Bulletin of Volcanology 68* DOI: 10.1007/s00445-005-0043-4

Ihinger PD, Hervig RL, McMillan PF, Zhang Y & Stolper EM (1994) Analytical methods for volatiles in rhyolitic melt. *Reviews in Mineralogy and Geochemistry 30*: 67-121

Ingason K, Kristjánsson V & Einarsson K (2014) Design and development of the discharge system of IDDP-1. *Geothermics 49*: 58-65

ISOR Iceland Geosurvey (2009) Krafla – Leirbotnar Hole KJ-39 (No. 129)

Jarosewich E, Nelen JA & Norberg JA (1980) Reference samples for electron microprobe analysis. *Geostandards Newsletter 4 (1)*: 257-258

Jochum KP, Nohl U, Herwig K, Lammel E, Stoll B & Hoffmann AW (2005) Georem: A new geochemical database for reference materials and isotopic standards. *Geostandards and Geoanalytical Research 29 (3)*: 333-338

Johannes W & Holtz F (1996) In: Wyllie PJ, (Ed.) *Petrogenesis and Experimental Petrology of Granitic Rocks*. Springer-Verlag. Berlin. 335

Jónasson K (1994) Rhyolite volcanism in the Krafla central volcano, north-east Iceland. *Bulletin of Volcanology 56*: 516-528

Júlíusson BM, Pálsson B & Gunnarsson A (2005) Krafla Power Plant in Iceland – 27 Years of Operation. *Proceedings World Geothermal Congress.* Antalya, Turkey. April 2005

Kennedy BM, Holohan EP, Stix J, Gravley DM, Davidson JRJ & Cole JW (2018) Magma plumbing beneath collapse caldera volcanic systems. *Earth Science Reviews 177*: 404-424

Kruszewski M & Wittig V (2018) Review of failure modes in supercritical geothermal drilling projects. *Geothermal Energy 6 (28)*

Lange RA & Carmichael ISE (1990) Thermodynamic properties of silicate liquids with emphasis on density, thermal expansion and compressibility. *Reviews in Mineralogy and Geochemistry 24* (1): 25-64

Lange RA (1997) A revised model for the density and thermal expansivity of K_2O-Na_2O-CaO-MgO-Al_2O_3-SiO_2 liquids from 700 to 1900 K: Extension to crustal magmatic temperatures. *Contributions to Mineralogy and Petrology 130 (1)*: 1-11

Langella G, Paoletti V, DiPippo R, Amoresano A, Steinunnardóttir K & Milano M (2017) Krafla geothermal system, north-eastern Iceland: Performance assessment of alternative plant configurations. *Geothermics 69:* 74-92

Le Bas MJ & Streckeisen AL (1991) The IUGS systematics of igneous rocks. *Journal of the Geological Society 148* (5): 825-833

Lowenstern JB (2001) Carbon dioxide in magmas and implications for hydrothermal systems. *Mineralium Deposita 36* (6): 490-502

MacDonald R, Sparks RSJ, Sigurdsson H, Mattey DP, McGarvie DW & Smith RL (1987) The 1875 eruption of Askja volcano, Iceland: combined fractional crystallisation and selective contamination in the generation of rhyolitic magma. *Mineralogical magazine 51 (360)*: 183-202

Mandeville CW, Webster JD, Rutherford MJ, Taylor BE, Timbal A & Faure K (2002) Determination of molar absorptivities for infrared absorption bands of H_2O in andesitic glasses. *American Mineralogist 87*: 813-821

Mangan MT & Sisson TW (2000) Delayed, disequilibrium degassing in rhyolite magma: decompression experiments and implications for explosive volcanism. *Earth and Planetary Science Letters 183*: 441-455

Marshall D (1996) Ternplot: An Excel spreadsheet for Ternary diagrams. *Computers and Geosciences 22* (6): 697-699

Masotta M, Mollo S, Nazzari M, Tecchiato V, Scarlato P, Papale P & Bachmann O (2018) Crystallisation and partial melting of rhyolite and felsite rocks at Krafla volcano: A comparative approach based on mineral and glass chemistry of natural and experimental products. *Chemical Geology 483*: 603-618. https://doi.org/10.1016/j.chemgeo.2018.03.031

Mbia P, Mortensen A, Okarsson N & Hardarson B (2015) Sub-surface geology, petrology and hydrothermal alteration of the Menengai geothermal field, Kenya: a case study of wells MW-02, MW-04, MW-06 and MW-07. In: *Proceedings World Geothermal Congress*. 2015. Melbourne, Australia. 20

McIntosh IM, Llewellin EW, Humphreys MCS, Nichols ARL, Burgisser A, Schipper CI & Larsen JH (2014) Distribution of dissolved water in magmatic glass records growth and resorption of bubbles. *Earth and Planetary Science Letters 401*: 1-11

McIntosh IM, Nichols ARL, Tani T & Llewellin EW (2017) Accounting for the species-dependence of the 3500 cm^{-1} H_2O_t infrared molar absorptivity coefficient: Implications for hydrated volcanic glasses. *American Mineralogist 102 (8)*: 1677-1689

Metrich N & Rutherford MJ (1992) Experimental study of chlorine behaviour in hydrous silicic melts. *Geochimica Cosmichica Acta 56*: 607-616

Morimoto N (1988) The nomenclature of pyroxenes. *Mineralogical Magazine 52*: 425-433

Mortensen AK, Grönvold K, Guðmundsson A, Steingrímsson B & Egilson Þ (2010) Quenched Silicic Glass from Well KJ-39 in Krafla, North-Eastern Iceland. *Proceedings World Geothermal Congress*. Bali, Indonesia. April 2010

Mortensen AK, Egilson Þ, Gautason B, Árnadóttir S & Guðmundsson Á (2014) Stratigraphy, alteration mineralogy, permeability and temperature conditions of well IDDP-1, Krafla, NE-Iceland. *Geothermics 49*: 31-41

Mortensen AK, Guðmundsson A, Steingrimsson B, Sigmundsson F, Axelsson G, Ármannsson H, Bjórnsson H, Agustsson K, Sæmundsson K, Olafsson M, Karlsdottir R, Halldorsdottir S & Hauksson T (2015) The Krafla conceptual model revision – Translation of report. In: Landsvirkjun report no. LV-2-15-098

Newbury DE & Ritchie NWM (2013) Elemental mapping of microstructures by scanning electron microscopy-energy dispersive x-ray spectrometry (SEM-EDS): extraordinary advances with the silicon drift detector (SDD). *Journal of Analytical Atomic Spectrometry 28*: 973-988

Newman S, Stolper EM & Epstein S (1986) Measurement of Water in Rhyolitic Glasses – Calibration of an Infrared Spectroscopic Technique. *American Mineralogist 71* (11-12): 1527-1541

Newman S & Lowenstern JB (2002) VolatileCalc: a silicate melt H_2O-CO_2 solution model written for Visual Basic for excel. *Computers & Geosciences 28*: 597-604

Nielsen G, Maack R, Guðmundsson A & Gunnarsson GI (2000) Completion of Krafla geothermal power plant. *Proceeding World Geothermal Congress.* Kyushu-Tohuku, Japan. May 2000

Nishikida K, Nishio E & Hannah RW (1996) *Selected applications of modern FTIR techniques*. CRC Press. Taylor & Francis Group. Florida. 200

Nowak M & Behrens H (2001) Water in rhyolitic magmas: getting a grip on a slippery problem. *Earth and Planetary Science Letters 184* (2): 515-522

Nuccio P & Paonita A (2001) Magmatic degassing of multicomponent vapours and assessment of magma depth: Application to Vulcano Island (Italy). *Earth Science Letters 193*: 467-481

Opheim JA & Guðmundsson A (1989) Formation and geometry of fractures, and related volcanism, of the Krafla fissure swarm, northeast Iceland. *Geological Society of America Bulletin 101*: 1608-1622

Panjasawatwong Y, Danyushevsky LV, Crawford AJ & Harris KL (1995) An experimental study of the effects of melt composition on plagioclase – melt equilibria at 5 and 10 kbar: implications for the origin of magmatic high-An plagioclase. *Contributions to Mineralogy & Petrology 118*: 420-432

Papale P, Moretti R & Barbato D (2006) The compositional dependence of the saturation surface of $H_2O + CO_2$ fluids in silicate melts. *Chemical Geology 229*: 78-95

Pearce TH & Kolisnik AM (1990) Observations of plagioclase zoning using interference imaging. *Earth Science Reviews 29*: 9-26

Perugini D and Poli G (2012) The mixing of magmas in plutonic and volcanic environments: Analogies and differences. *Lithos 153*: 261-277

Purtika K (2008) Thermometers and Barometers for Volcanic Systems. *Reviews in Mineralogy & Geochemistry 69*: 61-120

Reed SJB (1995) *Electron Probe Microanalysis*. In: Potts PJ, Bowles JFW, Reed SJB & Cave MR (eds) Microprobe Techniques in the Earth Sciences. The Mineralogical Society Series, 6. Springer, Boston

Reed SJB (2005) *Electron microprobe analysis and scanning electron microscopy in geology*. 2nd Ed. Cambridge, Cambridge University Press

Reinsch T, Dobson P, Asanuma H, Huenges E, Poletto F & Sanjuan B (2017) Utilising supercritical geothermal systems: a review of past ventures and ongoing research activities. *Geothermal Energy 5* (16)

Ripley EM, Li C, Moore CH, Elswick ER, Maynard JB, Paul RL, Sylvester P, Seo JH & Shimizu N (2011) Analytical methods for sulphur determination in glasses, rocks, minerals and fluid inclusions. *Reviews in Mineralogy & Geochemistry 73*: 9-39

Rollinson HH (1993) *Using geochemical data: evaluation, presentation, interpretation*. Longman Group Limited. Harlow, Essex

Ross CS (1962) Microlites in glassy volcanic rocks. *American Mineralogist 47 (5-6)*: 723-740

Sæmundsson K (1991) *Geology of the Krafla system*. In: Gardarsson, A., Einarsson, A. Nattura Myvatns. Reykjavik: 25-95

Saubin E, Kennedy BM, Tuffen H, Villenueve M, Watson T, Nichols ARL, Schipper I, Cole JW, Mortensen A & Zierenberg RA (2017) Reaction of rhyolitic magma to its

interception by the IDDP-1 well, Krafla, 2009. *American Geophysical Union conference, abstract.*

Saubin E (2020) Insights into the shallow intrusion of rhyolite from field, textures, and drilling of the IDDP-1 magma well, Krafla, Iceland (PhD Thesis). University of Canterbury. Christchurch.

Schipper IC, Castro JM, Kennedy BM, Christenson BW, Aiuppa A, Alloway B, Forte P, Seropian G & Tuffen H (2019) Halogen (Cl, F) and sulphur release during explosive, effusive and intrusive phases of the 2011 rhyolitic eruption at Cordón Caulle volcano (Chile). *Volcanica 2 (1)*: 73-90

Scholze H (1960) On the Question of Distinction between H_2O Molecules and OH Groups in Glasses and Minerals. *Naturwissenschaften 47* (10): 226-227 https://doi.org/10.1007/bf00602759

Seligman AN, Bindeman IN, Watkins JM & Ross AM (2016) Water in volcanic glass: From volcanic degassing to secondary hydration. *Geochimica et Cosmochimica Acta 191*: 216-238

Shea T (2017) Bubble nucleation in magmas: A dominantly heterogeneous process? *Journal of Volcanology and Geothermal Research 343*: 155-170

Sigurdsson H & Sparks RSJ (1981) Petrology of rhyolitic and mixed magma ejecta from the 1875 eruption of Askja, Iceland. *Journal of Petrology 22 (1)*: 41-84

Silver L & Stolper E (1989) Water in albitic glasses. *Journal of Petrology 30 (3)*: 667-709

Silver L (1990) The influence of bulk composition on the speciation of water in silicate glasses. *Contributions of Mineralogy and Petrology 104*: 142-162

Simon JI, Weis D, DePaolo DJ, Renne PR, Mundil R & Schmitt AK (2014) Assimilation of pre-existing Pleistocene intrusions at Long Valley by periodic magma recharge accelerates rhyolitic generation: rethinking the remelting model. *Contributions to Mineralogy and Petrology 167*

Sisson TW & Grove TL (1993) Experimental investigations of the role of H2O in calc-alkaline differentiation and subduction zone magmatism. *Contributions to Mineralogy & Petrology 113*: 143-166

Sparks RSJ (1978) The dynamics of bubble formation and growth in magmas: A review and analysis. *Journal of Volcanology and Geothermal Research 3* (1): 1-37

Stevenson RJ, Briggs RM & Hodder APW (1994) Physical Volcanology and Emplacement History of the Ben-Lomond Rhyolite Lava, Taupo Volcanic Centre, New Zealand. *New*

Zealand Journal of Geology and Geophysics 37 (3): 345-358. https://doi.org/10.1080/00288306.1994.9514625

Stewart C, Craig HM, Gaw S, Wilson T, Villarosa G, Outes V, Cronin S & Oze C (2016) Fate and agricultural consequences of leachable elements added to the environment from the 2011 Cordón Caulle tephra fall. *Journal of Volcanology and Geothermal Research 327*: 554-570

Stolper E (1982a) The speciation of water in silicate melts. *Geochimica et Cosmochimica Acta 46*: 2609-2620

Stolper E (1982b) Water in Silicate Glasses – An Infrared Spectroscopic Study. *Contributions to Mineralogy and Petrology, 81* (1): 1-17. https://doi.org/10.1007/bf00371154

Stolper E & Ahrens TJ (1987) On the nature of pressure-induces coordination changes in silicate melts and glasses. *Geophysical Research Letters 14* (12)

Stolper E (1989) Temperature-Dependence of the Speciation of Water in Rhyolitic Melts and Glasses. *American Mineralogist 74* (11-12): 1247-1257

Sturkell E, Einarsson P, Sigmundsson F, Hooper A, Ófeigsson BG, Geirsson H & Ólafsson H (2010) Katla and Eyjafjallajökull Volcanoes. *Developments in Quaternary Sciences 13*

Teplow W, Marsh B, Hulen J, Spielman P, Kaleeikinin M, Fitch D & Rickard W (2009) Dacite melt at the Puna geothermal venture well field, Big Island of Hawaii. *Geothermal Resource Council Transactions 33*: 989-994

Thorbjornsson I (2016) Deliverable D4.3 candidate materials for couplings and casings. *GeoWell*. Grant agreement no. 654497

Tindle AG & Pearce JA (1983) Assimilation and partial melting of continental crust: evidence from the mineralogy and geochemistry of autoliths and xenoliths. *Lithos 16*: 185-202

Tuffen H & Castro JM (2009) The emplacement of an obsidian dyke through thin ice: Hrafntinnuhryggur, Krafla Iceland. *Journal of Volcanology and Geothermal Research 185* (4): 352-366. https://doi.org/10.1016/j.jvolgeores.2008.10.021

Vogel A, Diplas S, Durant AJ, Azar AS, Sunding MF, Rose WI, Sytchkova A, Bonadonna C, Krüger K & Stohl A (2017) Reference data set of volcanic ash physiochemical and optical properties. *Journal of Geophysical Research: Atmospheres:* 10.1002/2016JD026328

von Aulock FW, Kennedy BM, Schipper CI, Castro JM, Martin DE et al. (2014) Advances in Fourier transform infrared spectroscopy of natural glasses: From sample preparation to data analysis. *Lithos 206*: 52-64. https://doi.org/10.1016/j.lithos.2014.07.017

von Aulock FW, Kennedy BM, Maksimenko A, Wadsworth FB & Lavallee Y. (2017) Outgassing from open and closed magma foams. *Frontiers in Earth Science 5.* doi.org/10.3389/feart.2017.00046

Walker D, Shibata T & DeLong SE (1979) Abyssal tholeiites from the Oceanographer Fracture Zone: 2 phase equilibria and mixing. *Contributions to Mineralogy and Petrology 70*: 111-125

Wallace PJ & Edmonds M (2011) The sulphur budget in magmas: Evidence from melt inclusions, submarine glasses and volcanic gas emissions. *Reviews in Mineralogy and Geochemistry 73*: 215-246

Wardell LI, Kyle PR & Counce D (2008) Volcanic emissions of metals and halogens from White Island (New Zealand) and Erebus volcano (Antarctica) determined with chemical traps. *Journal of Volcanology and Geothermal Research 177*: 734-742

Watson T (2018) Evolution of magmatic volatiles during drilling into a magma body, Krafla, Iceland (Masters' Thesis). Canterbury University. Christchurch.

Webster JD (1990) Partitioning of F between H2O and CO2 fluids and topaz rhyolite melt. *Contributions to Mineralogy and Petrology 104 (4)*: 424-438

Weisenberger TB, Axelsson G, Arnaldsson A, Blischke A, Óskarsson F, Ármannsson H, Blanck H, Helgadóttir HM, Berthet J-CC, Árnason K, Ágústsson K, Gylfadóttir SS, GuÐmundsdóttir V (2015) Revision of the Conceptual Model of the Krafla Geothermal System. Report No. LV-2015-040, íSOR-2015/012, Vatnaskil 15.03, Project No. 14-0200. Landsvirkjun 114 pages

Westrich HR, Stockman HW & Eichelberger JC (1988) Degassing of rhyolitic magma during ascent and emplacement. *Journal of Geophysical Research – Solid Earth 93* (B6): 6503-6511

Zajacz Z, Candela PA, Piccoli PM & Sanchez-Valle C (2012) The partitioning of sulphur and chlorine between andesite melts and magmatic volatiles and the exchange coefficients of major cations. *Geochimica et Cosmochimica Acta 89*: 81-101

Zhang Y, Jenkins J & Xu Z (1997) Kinetics of the reaction $H_2O + OH = 2OH$ in rhyolitic glasses upon cooling: Geospeedometry and comparison with glass transition. *Geochimica et Cosmochimica Acta 61 (11)*: 2167-2177

Zhang Y & Ni H (2010) Diffusion of H, C and O components in silicate melts. *Reviews in Mineralogy & Geochemistry 72*: 171-225

Zhang Y, Xu Z, Zhu M & Wang H (2007) Silicate melt properties and volcanic eruptions. *Reviews of Geophysics 45* (4): 1-27

Zierenberg RA, Schiffman P, Barfod GH, Lesher CE, Marks NE, Lowenstern JB et al. (2013) Composition and origin of rhyolite melt intersected by drilling in the Krafla geothermal field, Iceland. *Contributions to Mineralogy and Petrology 165* (2): 327-347. https://doi.org/10.1007/s00410-012-0811-z

Appendix A: Standards used for calibration of the microprobe results for the minerals and sulphides

***Table A.1**: Plagioclase standard measured values and standard deviations.*

Plag	Measured Value	STDEV	n
SiO_2	51.19	0.35	20
TiO_2	0.02	0.05	20
Al_2O_3	30.89	0.18	20
FeO	0.44	0.23	20
MnO	0.01	0.03	20
MgO	0.14	0.28	20
CaO	13.63	0.23	20
Na_2O	3.46	0.11	20
K_2O	0.16	0.01	20
Cr_2O_3	0.01	0.04	20

***Table A.2**: Pyroxene standards measured values and standard deviations.*

Pyx	Measured Value	STDEV	n
SiO_2	51.19	0.17	20
TiO_2	0.02	0.01	20
Al_2O_3	30.89	0.13	20
FeO	0.44	0.03	20
MnO	0.01	0.01	20
MgO	0.14	0.01	20
CaO	13.63	0.07	20
Na_2O	3.46	0.05	20
K_2O	0.16	0.03	20
Cr_2O_3	0.01	0.02	20

***Table A.3**: Pyrite standards measured values and standard deviations.*

Pyrite	Measured Value	STDEV	n
S	53.43	0.14	4
Mo	0.98	0.03	4
Bi	0.00	0.00	4
Zn	0.01	0.01	4
As	0.11	0.02	4
Si	0.00	0.00	4
Ni	0.00	0.00	4
Co	1.35	0.05	4
Ag	0.01	0.02	4
Pb	0.00	0.00	4
Cl	0.00	0.00	4
Fe	46.51	0.14	4
Cu	0.04	0.02	4
Au	0.00	0.00	4

Appendix B: Raw geochemical data obtained from the electron microprobe

Table B.1: *Measured geochemical values from EPMA measurements.*

Sample	SiO_2	TiO_2	Al_2O_3	Feo	MnO	MgO	CaO	Na_2O	K_2O	Cr_2O_3	S	F	Cl	Total
M1-B1	71.22	0.42	10.53	1.83	0.02	0.24	1.28	2.67	2.05	0.00	61.92	749.07	791.80	90.40
M1-B2	61.95	0.95	11.63	5.48	0.10	1.04	3.66	2.17	1.60	0.00	255.94	851.81	644.75	88.76
M2-B1	64.18	0.93	11.88	5.06	0.11	1.00	3.55	2.47	1.43	0.01	235.30	914.15	686.22	90.80
M2-B2	68.50	0.90	12.33	5.03	0.07	0.94	3.41	3.43	1.81	0.00	235.30	1019.66	820.07	96.62
M3-B1	60.84	1.65	12.67	9.09	0.14	2.03	5.81	3.05	1.39	0.01	734.78	1251.64	633.44	96.94
M3-B2	71.00	0.44	10.53	1.87	0.05	0.27	1.26	2.49	1.85	0.01	61.92	760.20	757.86	89.94
M4-B1	63.31	0.94	11.67	4.90	0.09	0.96	3.45	2.14	1.38	0.00	235.30	889.63	667.37	89.02
M4-B2	65.40	1.35	12.58	7.00	0.16	1.38	4.48	3.28	1.57	0.01	411.77	1196.11	670.20	97.44
M5-B1	72.18	0.40	10.90	1.69	0.01	0.23	1.11	2.74	2.65	0.00	20.64	917.85	825.73	92.10
M5-B2	60.41	1.71	12.66	9.04	0.16	2.06	5.86	3.06	1.41	0.04	749.23	1341.01	616.47	96.65
M5-B3	61.86	1.49	12.75	8.11	0.15	1.86	5.45	3.07	1.51	0.02	588.24	1252.52	644.75	96.53
M5-B4	60.69	1.75	12.76	8.95	0.16	2.05	5.91	3.09	1.40	0.00	796.70	1269.90	644.75	97.03
M5-B5	67.76	0.64	11.26	3.39	0.08	0.53	2.37	2.46	1.66	0.00	111.46	723.70	663.60	90.30
M5-B6	67.91	0.59	11.25	3.35	0.03	0.49	2.34	2.39	1.67	0,00	111.46	721.03	633.44	90.18
M5-B7	56.23	1.60	11.84	8.65	0.15	2.00	5.58	1.81	1.06	0.01	755.42	1252.58	607.04	89.20
M5-B8	66.57	0.61	10.99	3.50	0.08	0.51	2.30	2.00	1.45	0.01	117.65	751.45	706.96	88.18
M5-B9	63.15	1.37	12.56	7.69	0.12	1.62	4.98	3.08	1.50	0.03	520.13	1129.94	684.34	96.32
M6-B1	74.18	0.42	10.99	1.94	0.03	0.25	1.21	3.09	2.78	0.01	24.77	1021.33	776.71	95.07
M6-B2	67.83	0.98	12.31	5.59	0.11	0.99	3.66	3.31	1.80	0.00	253.87	1008.32	723.93	96.78
M6-B3	54.91	1.67	11.65	9.15	0.14	2.06	5.76	1.66	1.29	0.01	866.88	1138.29	599.50	88.56
M6-B4	56.70	1.97	12.34	11.63	0.17	2.58	6.90	2.76	1.10	0.01	1085.66	1485.01	584.42	96.47
M6-B5	71.22	0.39	10.62	1.82	0.04	0.25	1.18	2.49	1.81	0.00	37.15	852.80	803.11	90.00
M6-B6	72.01	0.64	11.83	3.55	0.11	0.51	2.33	3.47	2.02	0.00	86.69	1001.58	706.96	96.64
M6-B7	70.95	0.44	10.51	1.85	0.06	0.27	1.50	2.20	1.81	0.01	37.15	646.64	774.83	89.75
M6-B8	71.49	0.40	10.70	1.76	0.04	0.26	1.27	26.1	1.90	0.00	43.34	659.45	808.76	90.58
1	67.29	1.14	12.37	6.49	0.11	1.18	4.12	3.40	1.63	0.02	314.49	1151.60	646.50	98.45
3	61.76	1.59	13.02	9.20	0.14	2.08	5.81	3.14	1.32	0.02	769.05	1322.21	563.32	98.33
4	57.53	2.02	12.58	11.90	0.20	2.72	7.10	2.80	1.01	0.02	1169.12	1564.35	539.88	98.20
5	56.64	2.08	12.27	12.40	0.20	2.71	7.07	2.71	0.97	0.01	1197.55	1725.82	526.60	97.41
8	58.27	2.03	12.56	11.42	0.19	2.59	6.86	2.80	1.10	0.02	1042.97	1606.80	536.32	98.17
9	71.03	0.48	10.66	2.50	0.06	0.33	1.74	2.27	2.50	0.05	55.97	579.48	659.73	91.74
10	68.76	0.60	11.29	3.42	0.07	0.52	2.41	2.18	2.75	0.02	104.47	547.59	685.06	92.17
11	60.63	1.79	12.80	9.81	0.16	2.19	6.08	3.05	1.31	0.01	847.52	1367.45	594.65	98.10
12	72.98	0.67	12.22	4.02	0.08	0.60	2.53	3.63	2.45	0.03	99.50	1049.40	680.52	99.39
13	56.91	1.97	12.42	11.32	0.17	2.64	6.86	2.67	1.66	0.02	1119.37	1718.18	595.97	96.99
14	57.75	2.03	12.43	11.69	0.20	2.60	6.75	2.63	1.13	0.03	1122.13	1630.65	538.12	97.58
15	64.31	1.10	12.22	6.16	0.10	1.15	4.03	2.69	1.84	0.02	364.83	1169.12	724.00	93.83
16	56.94	2.07	12.32	12.18	0.21	2.75	7.17	2.74	1.02	0.03	1343.24	1827.67	526.89	97.82
17	61.54	1.67	12.85	8.81	0.12	2.01	5.61	3.05	1.47	0.01	696.50	1324.76	624.85	97.41
18	72.13	0.43	10.67	1.95	0.03	0.28	1.32	2.54	2.96	0.02	48.62	852.76	754.76	92.51
19	54.36	1.79	11.73	9.90	0.17	2.33	6.21	1.57	1.40	0.01	965.97	1147.23	561.43	89.74
20	67.35	1.22	12.90	6.57	0.10	1.24	4.24	3.51	1.68	0.02	351.37	1195.78	656.42	99.05
21	57.24	2.01	12.48	11.65	0.20	2.65	6.91	2.68	1.69	0.01	1146.32	1559.60	551.98	97.86

Sample	SiO_2	TiO_2	Al_2O_3	FeO	MnO	MgO	CaO	Na_2O	K_2O	Cr_2O_3	S	F	Cl	Total
a	62.13	1.71	12.93	9.07	0.12	1.99	5.77	3.12	1.38	0.02	696.50	1309.52	612.47	98.48
b	73.50	0.67	12.16	3.85	0.05	0.58	2.47	3.58	2.12	0.02	97.72	1002.40	661.08	99.17
c	58.75	1.96	12.72	11.16	0.18	2.55	6.79	2.92	1.16	0.02	1044.74	1516.83	582.23	98.52
d	58.44	1.43	12.14	7.98	0.10	1.76	5.27	1.68	1.51	0.00	601.97	952.10	603.40	90.52
e	67.53	0.63	12.14	3.63	0.09	0.53	2.85	2.35	2.06	0.01	85.29	534.65	612.47	91.94
f	73.84	0.44	11.05	2.05	0.05	0.28	1.48	1.50	1.48	0.02	40.42	666.76	751.41	92.33
g	59.72	1.45	12.14	8.14	0.14	1.65	5.00	1.23	1.09	0.00	579.23	1265.99	605.99	90.79
h	63.59	1.00	11.99	5.98	0.08	1.02	3.74	1.31	1.21	0.01	293.52	940.96	601.12	90.12
i	69.14	0.61	11.42	3.63	0.06	0.46	2.20	1.28	1.38	0.01	87.06	903.97	661.62	90.37
j	62.45	1.25	12.08	6.75	0.14	1.28	4.16	1.13	0.93	0.02	394.89	1067.22	647.92	90.40
k	75.42	0.42	11.27	1.98	0.05	0.25	1.40	1.86	1.73	0.01	43.53	535.53	767.48	94.52
l	62.34	1.42	12.31	7.70	0.14	1.53	4.80	1.55	1.24	0.02	509.93	1141.67	646.50	93.27
m	58.19	2.23	12.75	11.76	0.16	2.59	6.88	2.41	1.05	0.02	1176.58	1702.98	691.87	98.40
n	66.94	0.83	12.00	4.90	0.11	0.86	3.26	1.35	1.14	0.01	195.45	913.95	627.05	91.57
o	69.61	0.61	11.45	3.57	0.06	0.49	2.25	1.27	1.30	0.01	82.09	812.35	651.04	90.77
p	68.22	1.15	12.83	6.43	0.13	1.15	4.05	2.94	1.61	0.02	314.49	1110.58	665.94	98.72

Appendix C: FTIR Images of glass chip showing location of transects

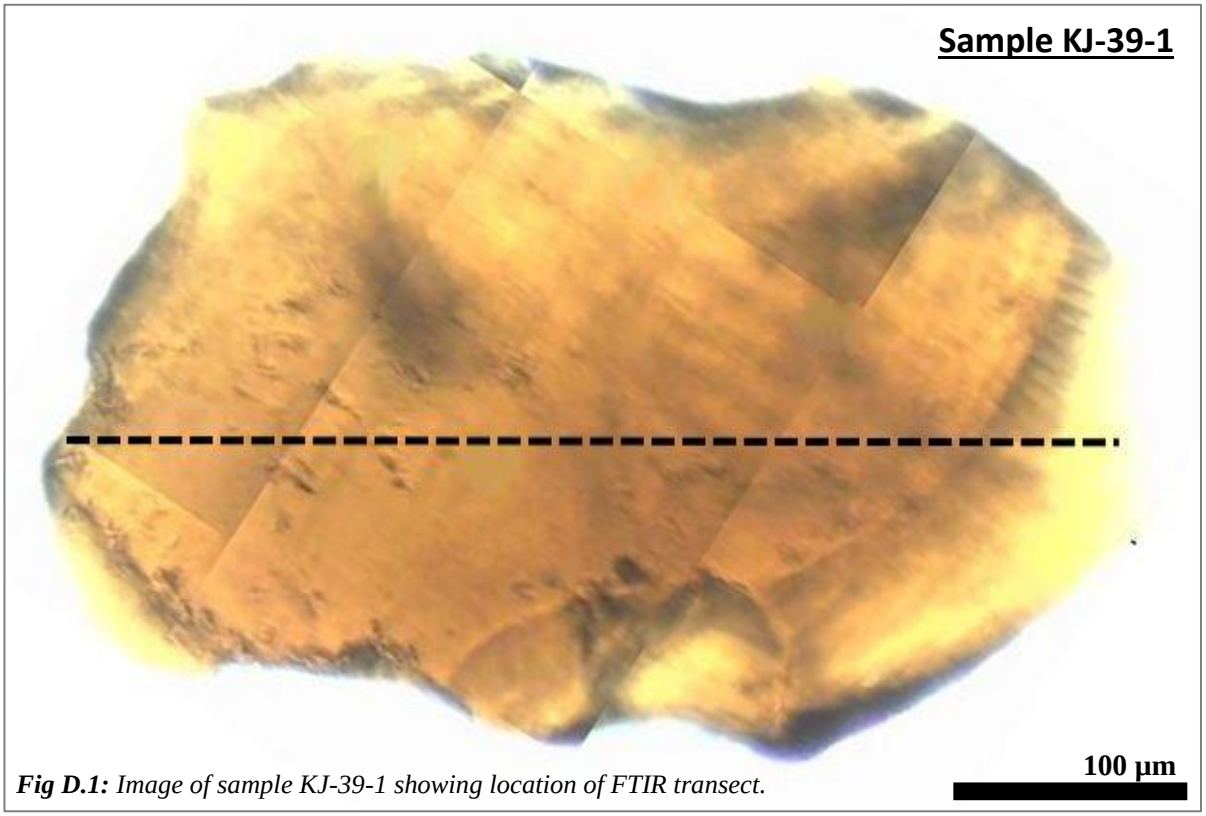

Fig D.1: *Image of sample KJ-39-1 showing location of FTIR transect.*

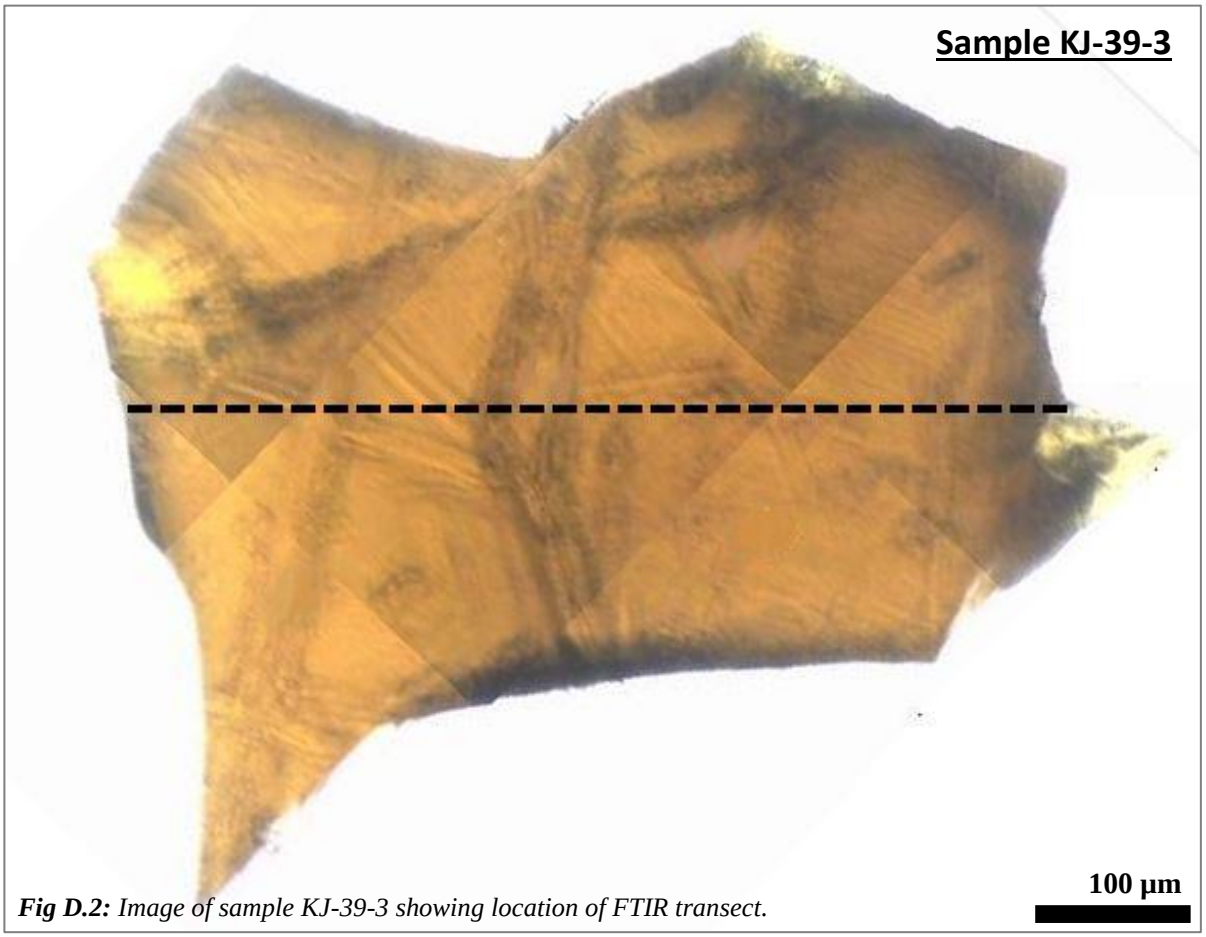

Fig D.2: *Image of sample KJ-39-3 showing location of FTIR transect.*

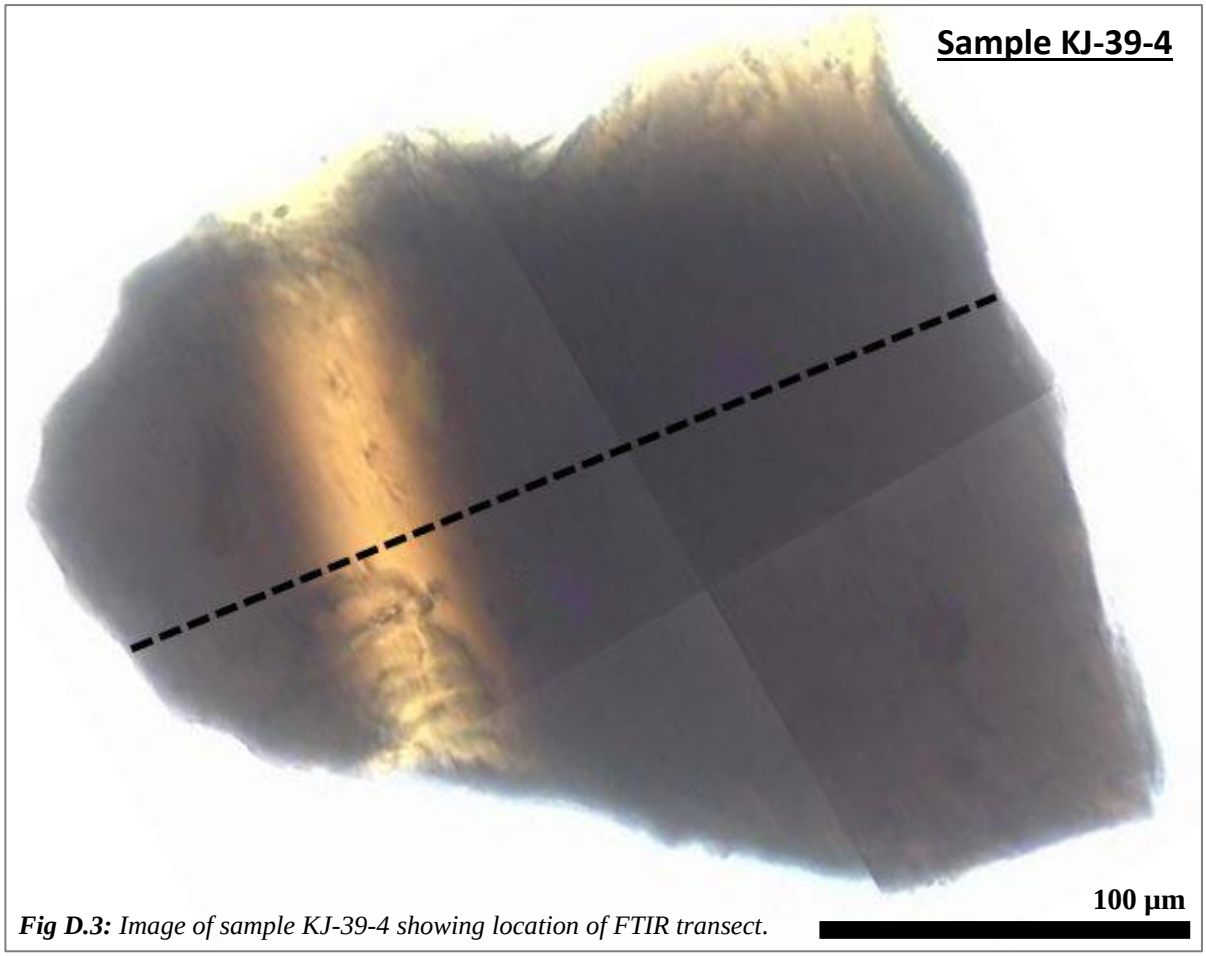

Fig D.3: *Image of sample KJ-39-4 showing location of FTIR transect.*

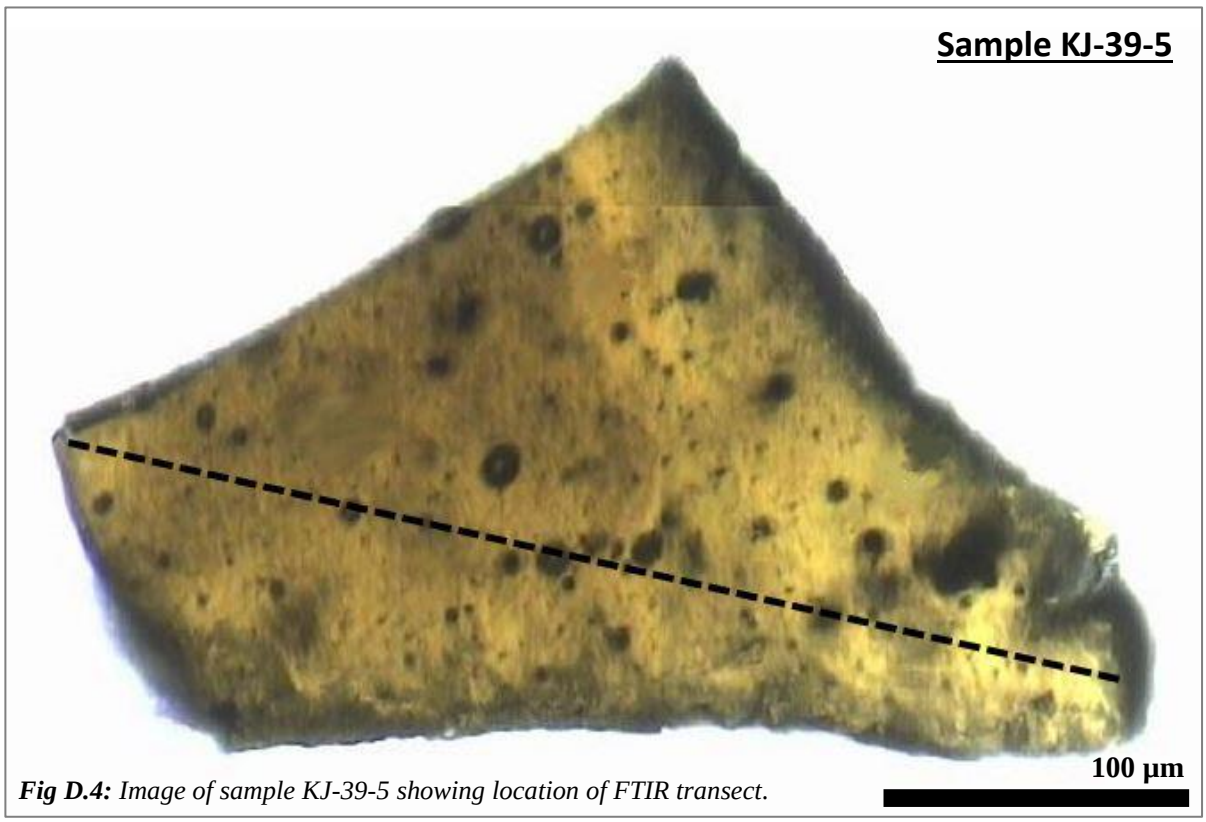

Fig D.4: *Image of sample KJ-39-5 showing location of FTIR transect.*

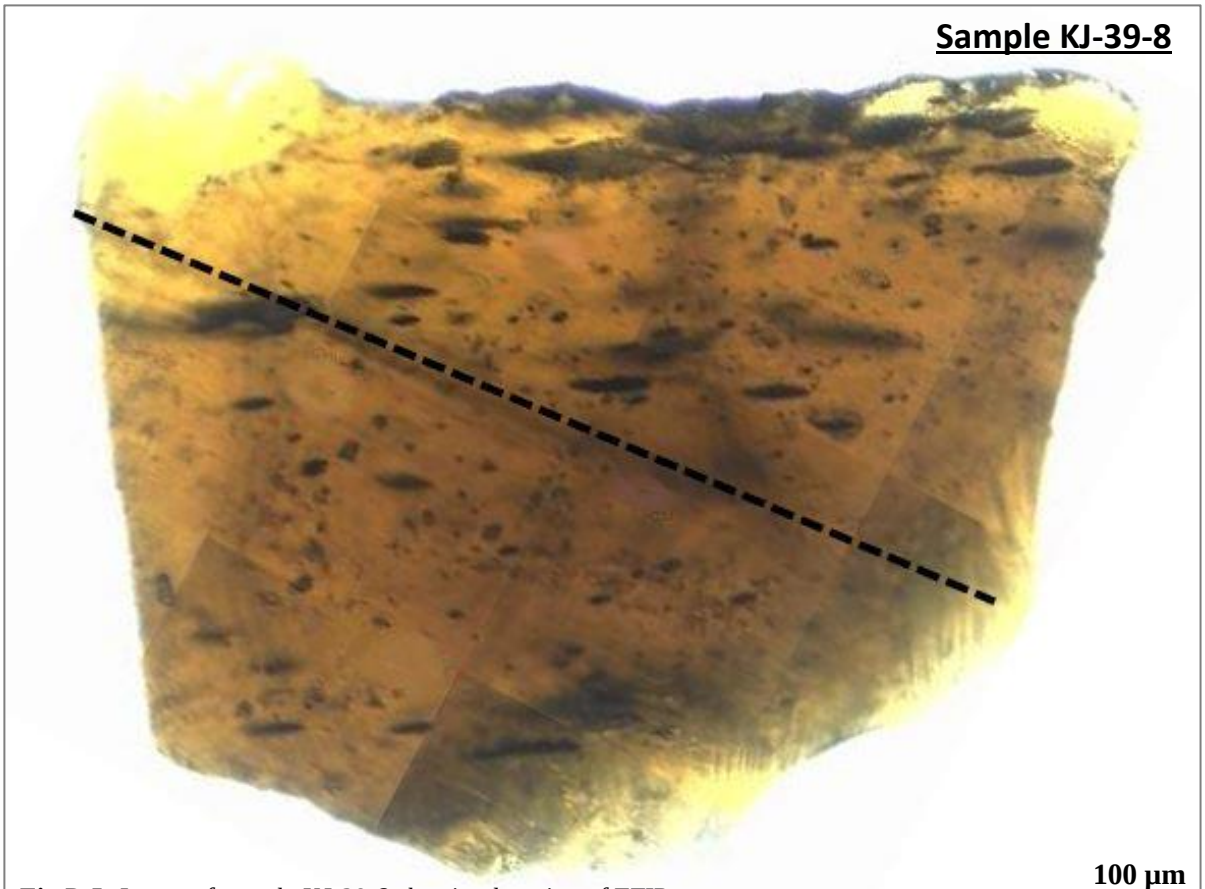

Fig D.5: *Image of sample KJ-39-8 showing location of FTIR transect.*

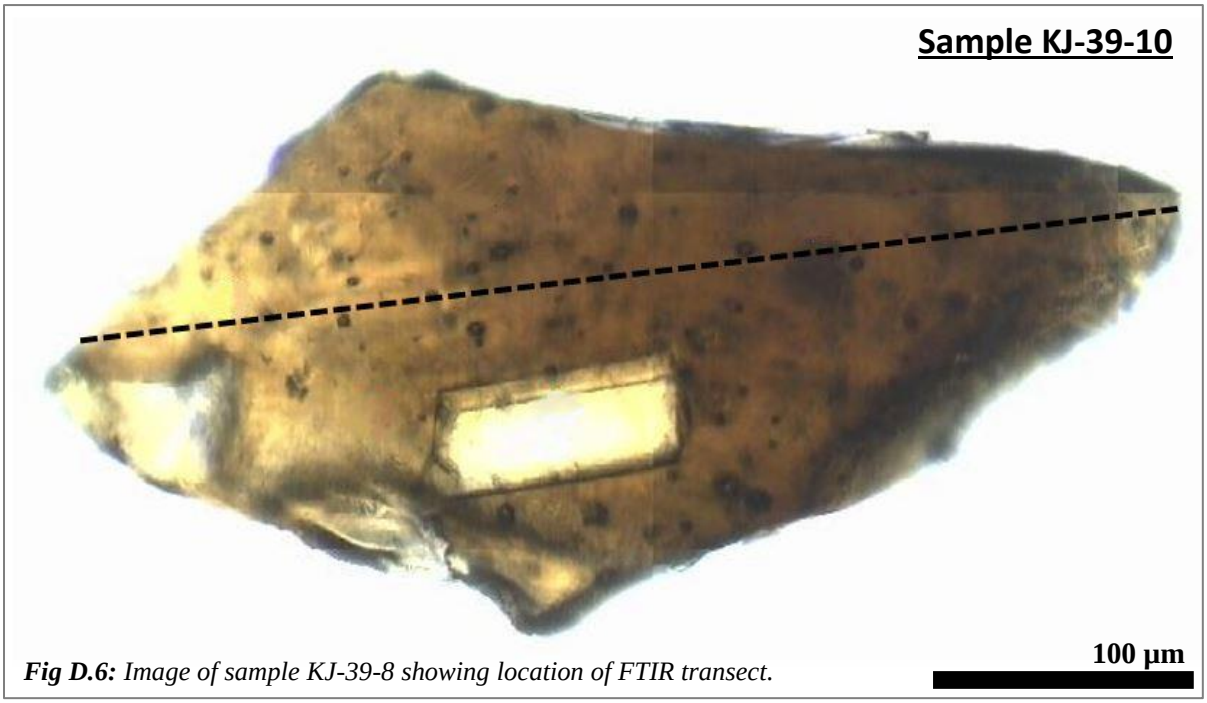

Fig D.6: *Image of sample KJ-39-8 showing location of FTIR transect.*

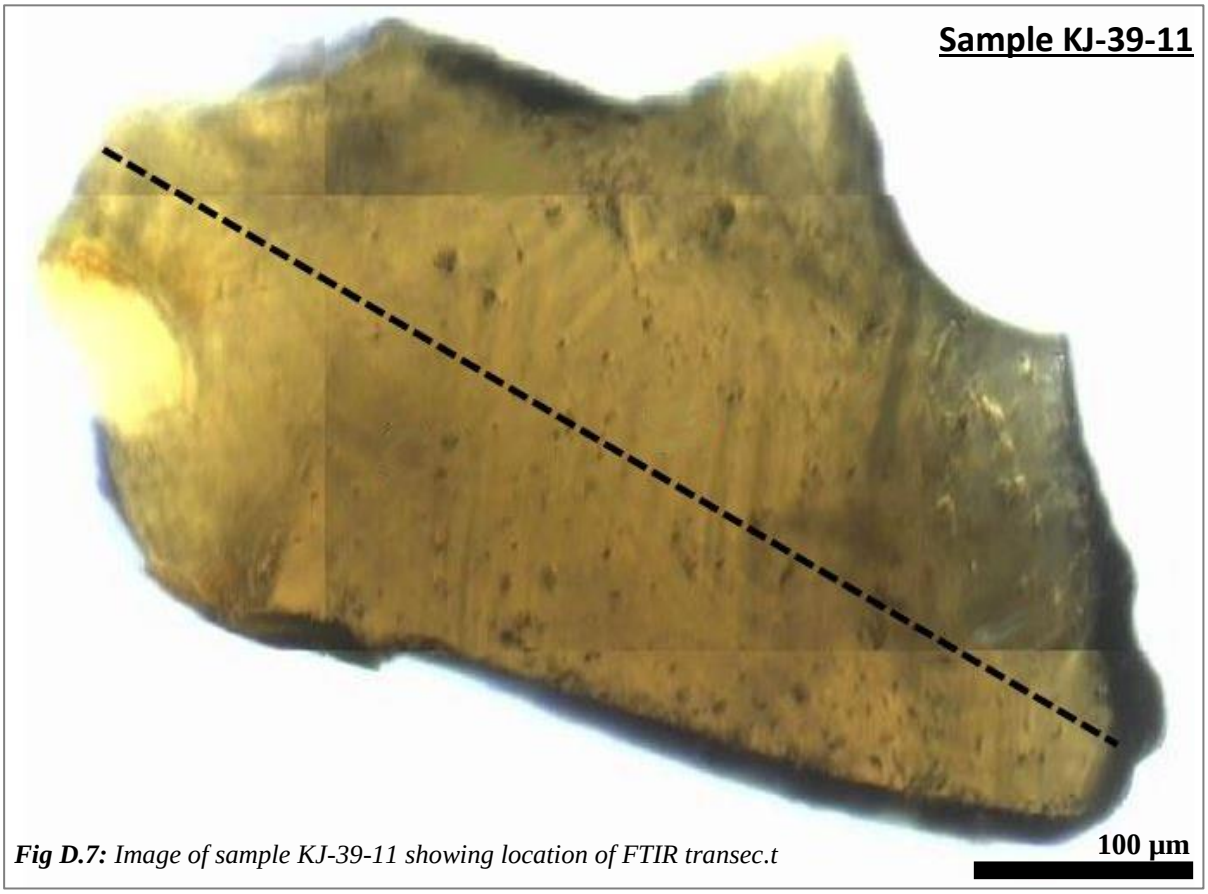

Fig D.7: *Image of sample KJ-39-11 showing location of FTIR transec.t*

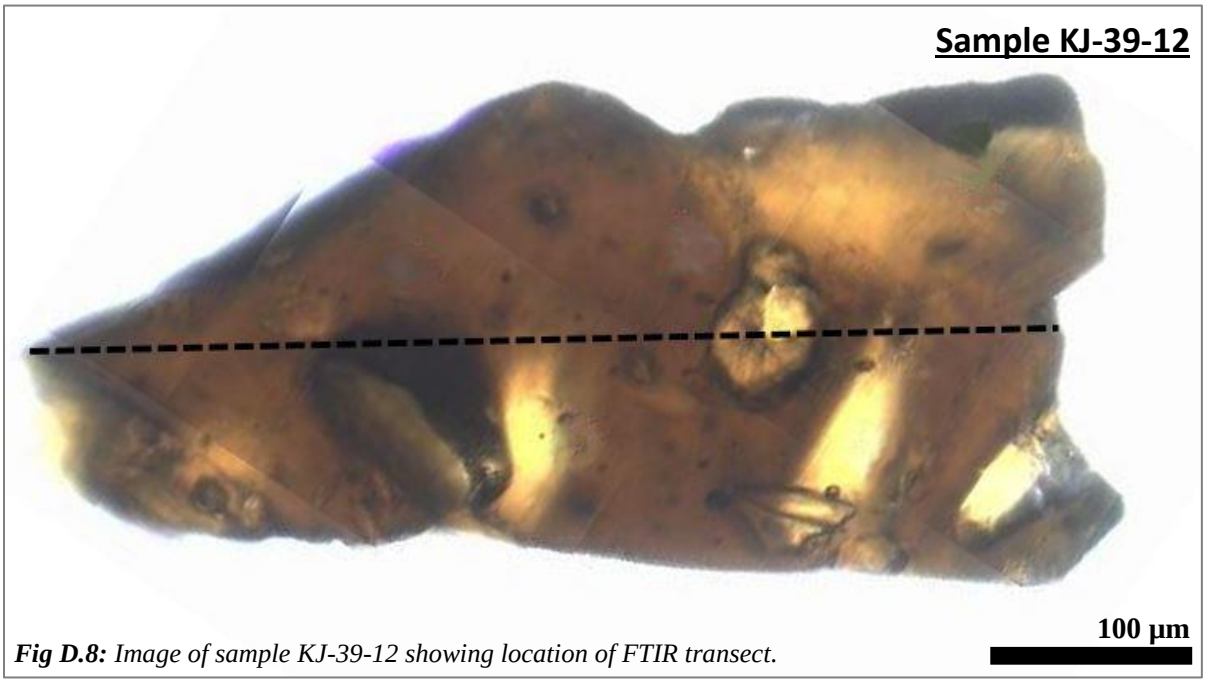

Fig D.8: *Image of sample KJ-39-12 showing location of FTIR transect.*